Design with Constructal Theory: Steam Generators, Turbines and Heat Exchangers

by

Yong Sung Kim

Department of Mechanical Engineering
and Materials Science
Duke University

Date: _____

Approved:

_____

Prof. Adrian Bejan, Co-Supervisor

_____

Prof. Sylvie Lorente, Co-Supervisor

_____

Prof. Josiah Knight

_____

Prof. Edward Shaughnessy

Dissertation submitted in partial fulfillment of
the requirement for the degree of Doctor
of Philosophy in the Department of
Mechanical Engineering and Materials
Science in the Graduate School
of Duke University

2010

Abstract

(Mechanical Engineering)

Design with Constructal Theory: Steam Generators, Turbines and Heat Exchangers

by

Yong Sung Kim

Department of Mechanical Engineering
and Materials Science
Duke University

Date: _____

Approved:

_____

Prof. Adrian Bejan, Co-Supervisor

_____

Prof. Sylvie Lorente, Co-Supervisor

_____

Prof. Josiah Knight

_____

Prof. Edward Shaughnessy

An abstract of a dissertation submitted in partial fulfillment of
the requirement for the degree of Doctor
of Philosophy in the Department of
Mechanical Engineering and Materials
Science in the Graduate School
of Duke University

2010

Abstract

This dissertation shows that the architecture of steam generators, steam turbines and heat exchangers for power plants can be predicted on the basis of the constructal law. According to constructal theory, the flow architecture emerges such that it provides progressively greater access to its currents. Each chapter shows how constructal theory guides the generation of designs in pursuit of higher performance. Chapter two shows the tube diameters, the number of riser tubes, the water circulation rate and the rate of steam production are determined by maximizing the heat transfer rate from hot gases to riser tubes and minimizing the global flow resistance under the fixed volume constraint. Chapter three shows how the optimal spacing between adjacent tubes, the number of tubes for the downcomer and the riser and the location of the flow reversal for the continuous steam generator are determined by the intersection of asymptotes method, and by minimizing the flow resistance under the fixed volume constraints. Chapter four shows that the mass inventory for steam turbines can be distributed between high pressure and low pressure turbines such that the global performance of the power plant is maximal under the total mass constraint. Chapter five presents the more general configuration of a two-stream heat exchanger with forced convection of the hot side and natural circulation on the cold side. Chapter six demonstrates that segmenting a tube with condensation on the outer surface leads to a smaller thermal resistance, and generates design criteria for the performance of multi-tube designs.

To my grandmother, Yang Hae Kim, in heaven

Table of Contents

List of Figures

Nomenclature

$a_{1,2}$	constants
a_a	slope for the acceleration friction factor, Eq. (3.63)
a_f	slope for the acceleration friction factor, Eq. (3.64)
A	area, m^2
b	constant
$b_{1,2}$	constants
B	variable, Eq. (3.18)
$B_{1,2}$	constants
Be	dimensionless pressure difference number, Eq. (3.42)
c	constant
$c_{1,2}$	constants
c_p	specific heat at constant pressure, $J\,kg^{-1}K^{-1}$
C	constant, Eq. (3.15)
C	capacity rate, Eq. (6.26)
C_a	dimensionless factor, Eq. (3.32)
C_D	drag coefficient
C_q	variable
C_1, C_2	diameter ratios, Eq. (5.22)
C^*	ratio of capacity rates, Eq. (6.46)
D	diameter, m
D_h	hydraulic diameter, m

f	friction factor
F	total drag force, N
F	aggregate function, Eq. (4.28)
F_1	drag force on one tube, N
g	gravitational acceleration, $m\ s^{-2}$
Gr	Grashof number, Eq. (5.13)
h	enthalpy, $J\ kg^{-1}$
h	heat transfer coefficient, $W\ m^{-2}K^{-1}$
h	tube length, m
h_f	specific enthalpy of saturated liquid, $J\ kg^{-1}$
h_{fg}	change of specific enthalpy between phases, $J\ kg^{-1}$
H	height, m
HP	high pressure
IP	intermediate pressure
k	thermal conductivity, $W\ m^{-1}K^{-1}$
k_{down}	heat absorption ratio of the downcomer
K	constant
K_1	constant, Eq. (6.38)
L	coordinate from the leading tube to the trailing tube, m, Fig. 5.12
L	length scale, m
LP	low pressure
m	constant

$\dot{m}$	mass flow rate, kg s^{-1}
$\dot{m}_{scale}$	mass flow rate scale, kg s^{-1}
$\dot{m}_{w}$	water mass flow rate, kg s^{-1}
$\dot{m}_{1}$	mass flow rate for a segmented tube, kg s^{-1}
$\dot{m}_{1}$	water flow rate scale in one tube, kg s^{-1}
$\dot{m}_{1,F}$	hot gas flow rate in one channel, kg s^{-1}
$\dot{m}_{3,max}$	maximum mass flow rate for 3-tube model, kg s^{-1}
$\dot{m}_{4,max}$	maximum mass flow rate for 4-tube model, kg s^{-1}
M	mass, kg
n	optimal number of tubes in the assembly, Eq. (3.46)
n_{down}	number of downcomer tubes
n_{up}	number of riser tubes
N	number of tubes
N	number of turbines
N_{tu}	number of heat transfer units, Eq. (3.21)
P	pressure, Pa
Pr	Prandtl number
q	heat transfer rate, W
$q_{3,max}$	maximum heat transfer rate for 3-tube model, W
$q_{4,max}$	maximum heat transfer rate for 4-tube model, W
q'''	volumetric heat transfer rate, W/m^3

Q	heat transfer rate, W
Q_B	heat transfer rate to the boiler, W
Q_R	heat transfer rate to the reheater, W
r_2	acceleration factor
r_3	friction factor
r_4	gravitational factor
R	global water flow resistance
R	ideal gas constant, $\mathrm{J\,kg^{-1}K^{-1}}$
Re	Reynolds number
$Re_{D,h}$	Reynolds number of the hot stream, Eq. (5.17)
$Re_{D_h,c}$	Reynolds number in the upper plenum, Eq. (5.16)
s	entropy, $\mathrm{J\,kg^{-1}K^{-1}}$
S	spacing between adjacent tubes, m, Fig. 3.2
S_{avg}	average spacing between adjacent tubes, m, Fig. 3.2
T	temperature, K
T_B	water boiling temperature, K
T_F	inlet fluid gas temperature, K
T_g	hot gas temperature, K
T_H	highest allowable temperature, K
T_{in}	inlet fluid temperature, K
T_L	outlet temperature of internal fluid, K
T_{out}	outlet hot gas temperature, K

T_0 inlet temperature of internal fluid, K

T_∞ inlet temperature of external fluid, K

u velocity component in the x direction, $m\ s^{-1}$

u dimensionless parameter, Eq. (6.22)

U free stream velocity, $m\ s^{-1}$

U_s velocity scale, $m\ s^{-1}$, Eq. (5.7)

U_1 free stream velocity in one channel, $m\ s^{-1}$

U_∞ external flow velocity, $m\ s^{-1}$

v velocity component in the y direction, $m\ s^{-1}$

v water specific volume, $m^3/\ kg$

v_f specific volume of saturated liquid, $m^3\ kg^{-1}$

v_{fg} change of specific volume between phases, $m^3\ kg^{-1}$

v_g specific volume of saturated vapor, $m^3\ kg^{-1}$

V total volume, m^3

V_t total volume of the cold fluid inside the tubes, m^3

$V_{1,2}$ velocity, $m\ s^{-1}$

w velocity component in the z direction, $m\ s^{-1}$

W width, m

W power, W

x quality of liquid-vapor mixture

x, y, z Cartesian coordinates, m, Fig. 5.1

y variable, Eq. (6.29)

z coordinate along length

z_c location of flow reserval, m

Greek symbols

α thermal diffusivity, $m^2\ s^{-1}$

β coefficient of volumetric thermal expansion, K^{-1}

ΔP pressure drop, Pa

ΔP_1 pressure drop in one tube, Pa

ΔP_a acceleration pressure drop, Pa

ΔP_f friction pressure drop, Pa

ΔP_g hydrostatic pressure difference, Pa

ΔT temperature difference, K

ε effectiveness

η turbine isentropic efficiency

θ variable, Eq. (3.17)

λ Lagrange multiplier

μ dynamic viscosity, $N\ s\ m^{-2}$

μ Lagrange multipliers

ν kinematic viscosity, $m^2\ s^{-1}$

ξ dimensionless group, Eq. (2.20)

ρ density, $kg\ m^{-3}$

ρ_1 water density in the tube, kg m^{-3}

ρ_f density of saturated liquid, kg m^{-3}

σ ratio between spacing and average spacing

ϕ volume fraction occupied by water, Eq. (3.2)

Φ auxiliary function

Ψ auxiliary function

Subscripts

a the large S limit

b the small S limit

c cross-section

c cold

cond conduction

conv convection

down downcomer

D diameter

ext external

F flue gas

g gas

h hot

H high

i i th turbine

i intermediate

in	inlet
int	internal
L	low
max	maximum
min	minimum
opt	optimum
out	outlet
ref	reference
rev	reversible
seg	segment
T	total
up	riser
W	wall
0	reference state
1	single tube
1	downcomer
1	inlet of the first turbine
1,2,3,4	tube number
1′	outlet of the first turbine
2	multiple tubes
2	riser
2	inlet of the second turbine
2′	outlet of the second turbine

∞ external free stream

Superscripts

~ dimensionless

Acknowledgement

As I finish my Ph.D program at Duke University in the United States, it gives me great pleasure to acknowledge and express gratitude to those individuals who have supported me in terms of finances, knowledge and morale:

CEO Gee Won Park, Doosan Heavy Industries, South Korea
Professor Adrian Bejan, Duke University
Professor Sylvie Lorente, University of Toulouse INSA, France
Professor Josiah Knight, Duke University
Professor Edward Shaughnessy, Duke University
CTO Seung Joo Choe, Doosan Heavy Industries, South Korea
Professor Jung Yul Yoo, Seoul National University, South Korea
Former EVP/CTO John Yoon, Doosan Heavy Industries, South Korea

I want to thank my collegues who challenged me with tough but interesting problems and made me realize the chasm between designs on paper, or in the computer, and living engineered products. They opened new worlds that were not reachable to me and, at the same time, applied my work to their engineering activities. At times they frustrated me, but they also inspired me to keep on going.

Finally, I want to thank my family whose support and prayers helped me complete my research and this dissertation.

1. Introduction

In this thesis I use constructal theory in the conceptual design of large scale components for commercial power plants. Power plants represent a major area for engineering development, and a most fertile field for novel methods of design and for new design concepts. Constructal theory is ideally suited for this because it begins the conceptual design with a clean slate, and invites the designer to recognize and consider all the possible and competing configurations. The architecture of the complex flow system is the unknown. There is no bias, no pre-existing rule of thumb.

Constructal theory focuses attention on the generation of flow configurations [1, 2]. Natural and engineered flow systems have configurations. They are not amorphous. “Flow” represents the movement of one entity relative to another (the background). To describe a flow, we speak of what the flow carries (fluid, heat, mass), how much it carries (mass flow rate, heat current, species flow rate), and where the stream is located in the available space. The “where” is the drawing, i.e. the design.

According to constructal theory, the generation of flow configuration can be reasoned based on an *evolutionary* principle of increase of flow access in time (the constructal law): “For a finite-size flow system to persist in time (to live) its configuration must change in time such that it provides greater and greater access to its currents” [3]. The evolution of flow configuration is like an animated movie, which runs in a particular direction in time such that each screen (i.e. each drawing) is replaced by a screen that

flows more easily *as a whole*.

The flow configuration that emerges from this natural tendency is the result of the persistent struggle, contortion and mechanism by which the global flow system achieves global flow performance under global constraints. A growing literature is showing that the constructal law is being used for better engineering and for better organization of the movement and connecting of people, goods and information [1-18]. This direction is recognized as *constructal design*, and with it designers seek not only better configurations but also better (faster, cheaper, more direct, more reliable) strategies for generating the geometry that is missing.

The traditional approaches contrast to constructal design: the configuration is assumed as known and then it has been searched over a long time by trail and error such as “cut and try method” or “design, build and test method” [19, 20]. For example, power plants have been developed over 100 years through these traditional methods. The old approaches have cost tremendous money and time in the development of engineered products. The more critical limitation of this old paradigm is that the optimal configuration can not be found.

In this thesis each chapter shows constructal design, i.e., searching configuration, at several levels of power plant engineering such as steam generator, continuous steam generator, mass distribution of turbines, heat exchangers with natural and forced convection and crossflow heat exchangers. These searches are done by the constructal

law: minimizing global flow resistance under constraints.

Chapter two shows that the architecture of a steam generator can be predicted. The circulation of water for the steam generator is driven by buoyancy in one unheated large tube (the downcomer) and many heated parallel smaller tubes (the riser). The steam generator has the freedom to select the diameter ratio of downcomer and riser tubes in the pursuit of maximizing water circulation rate while the flow volume is fixed. Two flow models are used: single phase liquid in the downcomer and riser, and liquid-vapor mixture in the riser tubes. Features that result from constructal design are: the tube diameters, the number of riser tubes, the water circulation rate, the rate of steam production, and how the flow architecture should change when the operating pressure and the size of the flow system change.

Chapter three presents that the main features of a continuous steam generator can be determined. The steam generator is modeled as continuous when all tubes are heated: a large number of steam tubes in crossflow with a stream of hot gases. The continuous steam generator is designed when the operating pressure is low. The geometry is free to vary in the search for maximum heat transfer density. The total volume of the assembly and the volume of the steam tubes are fixed. The steam flow in the tubes is modeled in two ways: single-phase and two-phase fully developed turbulent flow. The location of the flow reversal (i.e. the demarcation between the tubes of the heated downcomer and those of the riser), the optimal spacing between adjacent tubes, and the number of tubes for the

downcomer and the riser will be searched.

Chapter four demonstrates that the mass distribution for steam turbines of thermal power plants can be found. This is shown for two design classes: a high pressure turbine in series with a low-pressure turbine (two turbines) and a train consisting of many turbines expanding the steam at nearly constant temperature (multiple turbines). The mass inventory of steam turbines is distributed such that the power delivery of power plants is maximized with the fixed total mass. In addition, the optimal intermediate pressures between high pressure and low pressure are searched.

Chapter five details the search for the best flow configuration of a heat exchanger with natural and forced convection in crossflow. The hot side is a single-phase fluid that flows perpendicularly to vertical round tubes, and heats them by forced convection. The cold side is driven by buoyancy (as a thermosyphon) in the vertical tubes. The flow is laminar on both sides. We vary the geometry of a heat exchanger freely, and show how the geometry controls global performance (or heat transfer rate density).

Chapter six concerns the conceptual construction of crossflow heat exchangers that tends to achieve progressively higher heat transfer density. The first step is segmenting s single tube in crossflow with condensation on the outer surface of the tube into equidistant tubes in pursuit of higher heat transfer rate. We expand this segmenting idea to the search of the configuration of crossflow heat exchangers without condensation.

2. Constructal Steam Generator Architecture

The global objective of a steam generator is to heat the stream of water in the most compact manner possible [21, 22]. Compactness translates ultimately into less volume, weight and cost of manufacturing, transportation, assembly and maintenance. It is also related to the improvement of thermodynamic performance subject to finite-size constraints, as we discuss further in Section 2.5. Here we account for this complex design mission by fixing the volume of the flow device, and by using this constraint consistently at every level of construction, i.e., at every length scale.

The water flow through the steam generator is driven by the self-pumping principle illustrated in Fig. 2.1. The vertical tubes shown on the right are heated, bubbles form in them, and the liquid-steam mixture flows upward. Together, they constitute the "riser", which is heated by external combustion gases.

The circulation in the downcomer-riser-downcomer loop is driven by buoyancy effects, as the density of the liquid in the downcomer is greater than the density of the two-phase mixture in the riser. While the circulation continues because of the heating administered to the riser tubes, steam is collected from the upper plenum while make-up liquid is added to the same plenum.

2.1 Tube diameters

We begin with the pure fluid mechanics part of the problem, which is the maximization of steam generation rate per unit of flow volume. When the quality of the

steam (x) produced by the riser is specified, the maximization of steam generation rate is the same as maximizing the circulation rate ($\dot{m}$) through the riser-downcomer loop.

The self-pumping effect [23-26] is due to the difference between the hydrostatic pressure sustained by the downcomer ($\rho_1 gH$) and the hydrostatic pressure sustained by the riser ($\rho_2 gH$), where $\rho_1 > \rho_2$, and H is the height of both columns. The driving pressure difference $(\rho_1 - \rho_2)gH$ is balanced by the pressure losses encountered by the fluid during its circulation,

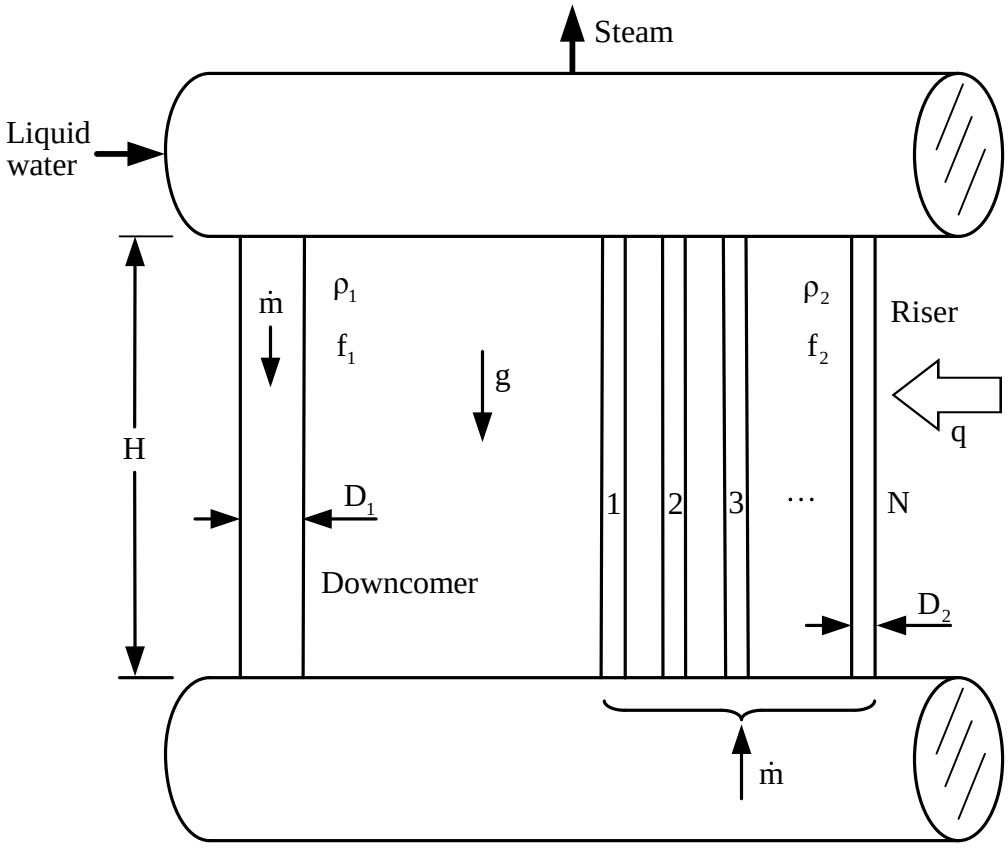

Figure 2.1: Steam generator with self-pumping effect, downcomer and riser tubes.

$$(\rho_1 - \rho_2) g H = \Delta P_1 + \Delta P_2 \tag{2.1}$$

For orientation, we begin with a simple model in which the fluid in both columns is modeled as liquid with constant properties. The pressure drop due to flow friction along each column is

$$\Delta P_{1,2} = 4 f_{1,2} \frac{H}{D_{1,2}} \frac{1}{2} \rho_{1,2} V_{1,2}^2 \tag{2.2}$$

We model the flow as fully turbulent in the fully rough regime, i.e. with constant friction factor f in each column. Mass conservation requires that the mass flow rate $\dot{m}$ is the same in both columns,

$$\dot{m} = \rho_1 \frac{\pi}{4} D_1^2 V_1 = \rho_2 N \frac{\pi}{4} D_2^2 V_2 \tag{2.3}$$

By using Eq. (2.3) to eliminate V_1 and V_2, we rewrite Eq. (2.1) as a global flow resistance that depends on D_1 and D_2:

$$\frac{(\rho_1 - \rho_2) g}{(32/\pi^2) \dot{m}^2} = \frac{f_1/\rho_1}{D_1^5} + \frac{f_2/\rho_2}{N^2 D_2^5} \tag{2.4}$$

The two sizes, D_1 and D_2, vary subject to the total volume constraint

$$\frac{\pi}{4} D_1^2 H + N \frac{\pi}{4} D_2^2 H = V, \text{ constant} \tag{2.5}$$

which means that

$$D_1^2 + ND_2^2 = \text{constant} \qquad (2.5')$$

The method of undetermined coefficients (or Lagrange multipliers) delivers the optimal D_1 and D_2 for which the global flow resistance (2.4) is minimal. The method consists of constructing a linear combination of the right-hand sides of Eqs. (2.4) and (2.5′),

$$\Psi = \frac{f_1/\rho_1}{D_1^5} + \frac{f_2/\rho_2}{N^2 D_2^5} + \lambda\left(D_1^2 + ND_2^2\right) \qquad (2.6)$$

solving the two equations $\partial\Psi/\partial D_1 = 0$ and $\partial\Psi/\partial D_2 = 0$, and eliminating λ by dividing the two equations. The result is

$$\left(\frac{D_1}{D_2}\right)_{\text{opt}} = \left(N^3 \frac{f_1}{f_2}\frac{\rho_2}{\rho_1}\right)^{1/7} \qquad (2.7)$$

The conclusion is that $(D_1/D_2)_{\text{opt}}$ varies as $N^{3/7}$, because f_1/f_2 and ρ_2/ρ_1 are two constants. To obtain the actual values of D_1 and D_2, we combine Eq. (2.7) with the total flow volume constraint (2.5).

The minimized global flow resistance that corresponds to this design is obtained by combining Eqs. (2.4), (2.5) and (2.7):

$$\left[\frac{(\rho_1 - \rho_2)g}{\left(32/\pi^2\right)\dot{m}^2}\right]_{\text{min}} = \left(\frac{\pi H}{4V}\right)^{5/2} \frac{f_1}{\rho_1}\left[1 + \left(\frac{f_2/\rho_2}{f_1/\rho_1}\right)^{2/7} N^{1/7}\right]^{7/2} \qquad (2.8)$$

It is to be expected that f_2/ρ_2 will be greater than f_1/ρ_1, because the ρ_2 liquid is lighter (it has bubbles), and because turbulent two-phase flow is more resistive than single phase, ($f_1 < f_2$). If f_2/ρ_2 is much greater than f_1/ρ_1, then Eq. (2.8) becomes

$$\left[\frac{(\rho_1 - \rho_2)g}{(32/\pi^2)\,\dot{m}^2}\right]_{min} \cong \left(\frac{\pi H}{4V}\right)^{5/2}\left(\frac{f_2}{\rho_2}\right)N^{1/2} \tag{2.9}$$

and, in addition to Eq. (2.7), the following results hold:

$$D_{1,opt} = \left(\frac{4V}{\pi H}\right)^{1/2} b^{-1/7} N^{-1/14} \tag{2.10}$$

$$D_{2,opt} = \left(\frac{4V}{\pi H}\right)^{1/2} N^{-1/2} \tag{2.11}$$

where

$$b = \frac{f_2/\rho_2}{f_1/\rho_1} > 1 \tag{2.12}$$

Note that both tube sizes decrease as N increases, but D_2 decreases much faster than D_1. The minimal flow resistance increases in proportion with the group $(H/V)^{5/2}(f_2/\rho_2)N^{1/2}$ and does not depend on (f_1/ρ_1). If V/H is the effective cross-sectional area (A_c) of all the tubes (downcomer and riser tubes), then the minimal flow resistance varies on $A_c^{-5/2}$. More attractive is to use a larger A_c and a smaller N, but in this limit the contact surface between the riser and the combustion gases that heat the ρ_2 stream is small. There is a tradeoff that leads to the optimal number of riser tubes N, and it comes from maximizing the heat transfer performance of the assembly.

2.2 Number of tubes

Consider next the rate of heat transfer (q) from hot gases to the ρ_2 liquid that flows

through the N riser tubes. In a simple model, the fluid is single phase, the heat transfer conductance is accounted for by the overall heat transfer coefficient h, and the total tube contact surface is

$$A_W = \pi D_2 H N \tag{2.13}$$

The hot gases are considered isothermal at the temperature T_g. The temperature of the ρ_2 fluid at the inlets to the N tubes is T_{in}. The heat transfer rate q from T_g to the $\dot{m}$ stream is (Ref. [27], p. 319),

$$q = \dot{m} c_P \left(T_g - T_{in} \right) \left[1 - \exp\left(-\frac{h A_W}{\dot{m} c_P} \right) \right] \tag{2.14}$$

Here all the parameters are known constants except $\dot{m}$ and A_W, which both depend on N. According to Eq. (2.9), the $\dot{m}(N)$ function is

$$\dot{m} = c_1 N^{-1/4} \tag{2.15}$$

where c_1 is shorthand for the expression

$$c_1 = \pi^{-1/4} \left[g(\rho_1 - \rho_2) \frac{\rho_2}{f_2} \right]^{1/2} \left(\frac{V}{H} \right)^{5/4} \tag{2.16}$$

Equations (2.13) and (2.11) show that

$$A_W = c_2 N^{1/2} \tag{2.17}$$

where

$$c_2 = \left(4\pi VH\right)^{1/2} \tag{2.18}$$

Together, Eqs. (2.14)-(2.18) deliver q as a function of N, which can be summarized as

$$q = c_1 c_P \left(T_g - T_{in}\right)\left(\frac{c_2 h}{c_1 c_P}\right)^{1/3} \xi^{-1/3}\left(1 - e^{-\xi}\right) \tag{2.19}$$

where

$$\xi = \frac{c_2 h}{c_1 c_P} N^{3/4} \tag{2.20}$$

The function $\xi^{-1/3}\left(1 - e^{-\xi}\right)$ reaches its maximum at $\xi_{opt} = 1.904$, which means that the optimal number of riser tubes is

$$N_{opt} = \left(1.904 \frac{c_1}{c_2} \frac{c_P}{h}\right)^{4/3} \tag{2.21}$$

Furthermore, because c_1 is proportional to $(V/H)^{5/4}$ and c_2 is proportional to $(VH)^{1/2}$, we conclude that N_{opt} is proportional to $V/H^{7/3}$, as follows

$$N_{opt} = \left(1.904 \frac{c_P}{2h}\right)^{4/3} \left[g\left(\rho_1 - \rho_2\right)\frac{\rho_2}{f_2}\right]^{2/3} \frac{V}{\pi H^{7/3}} \tag{2.22}$$

Tall steam generators should have fewer riser tubes than short steam generators. The optimal number of riser tubes should be proportional to the total flow volume (downcomer and riser).

As a numerical example, consider a steam generator for a current large-scale power plant. Its global parameters are: V = 47 m^3, H = 36 m, ρ_1 = 624 kg/m^3, ρ_2 = 518

kg/m^3, $f_2 = 0.00475$, $c_P = 7700$ J/kg K, and h ~ 104 W/m^2 K. The fluid is water at P = 13.8 MPa. Substituting these parameters in Eq. (2.22) we obtain $N_{opt} = 541$. In current 100 MW power plant designs the number of the designed riser tubes is approximately 400. The agreement is good in an order of magnitude sense. The discrepancy between 541 and 400 tubes can be attributed to the overall heat transfer coefficient h, the single phase flow assumption in the analysis, or to the fact that in practice N is not optimized. With the exception of h, all the data assumed in Eq. (2.22) are fixed as properties and physical dimensions that are known with certainty. Therefore, to evaluate the validity of the optimal number of the riser tubes Eq. (2.22), the overall heat transfer coefficient must be investigated and this means that a more accurate heat transfer model is required for a definitive constructal design.

2.3 Two-phase flow in the riser tubes

In Sections 2.1 and 2.2 we relied on simple models in order to demonstrate the opportunity for discovering from principle the main features of the flow architecture: the tube diameters and the number of riser tubes. In the second part of two-phase flow we rely on more accurate models of two-phase flow in order to refine the calculation procedure and the features of the constructal architecture.

Consider the more realistic model where the flow in the riser tubes is two-phase. To start with, in Eq. (2.1) the density ρ_2 is replaced with by r_4/ v_f

$$\left(\rho_1 - \frac{r_4}{v_f}\right) gH = \Delta P_1 + \Delta P_2 \tag{2.23}$$

where r_4 is the gravitational factor [28] for the two phase liquid-steam mixture column, and v_f is the specific volume of saturated liquid. The gravitational factor r_4 accounts for the void slip effect on the density of liquid-steam in the vertical column, Fig. 2.2, where x is the quality of the two-phase mixture. The frictional pressure loss along the downcomer is, cf. Eq. (2.2),

$$\Delta P_1 = 4 f_1 \frac{H}{D_1} \frac{1}{2} \rho_1 V_1^2 \tag{2.24}$$

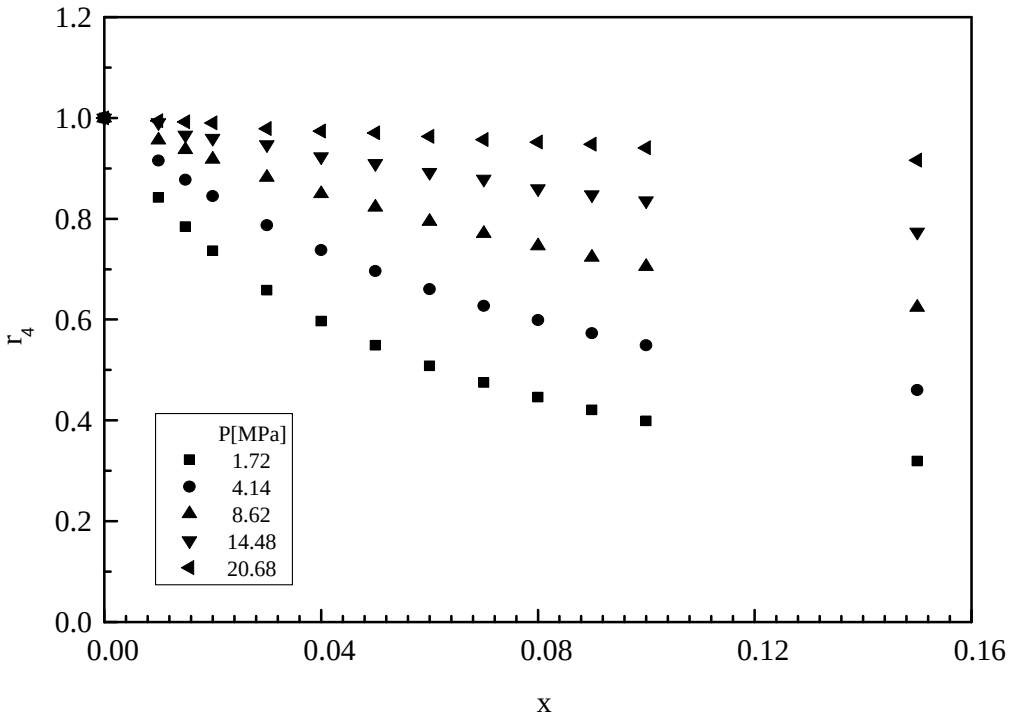

Figure 2.2: The r_4 factor for two-phase mixture gravitational pressure drop.

where V_1 is the mean water velocity in the downcomer,

$$V_1 = \frac{\dot{m}}{\rho_1 (\pi/4) D_1^2} \tag{2.25}$$

and D_1 is the inner diameter of the downcomer column. The friction factor f_1 is a function of the downcomer Reynolds number

$$Re_1 = \frac{V_1 D_1}{\nu_1} = \frac{\dot{m}}{(\pi/4) D_1 \mu_1} \tag{2.26}$$

and the roughness of the downcomer surface. This function is provided by the correlations displayed in the Moody chart [29]. In the present analysis we assume that the surface is smooth, and use a smooth-wall correlation proposed [30] for the range $2 \times 10^3 < Re_1 < 10^7$:

$$f_1(Re_1) = \frac{1}{4(1.82 \log_{10} Re_1 - 1.64)^2} \tag{2.27}$$

The pressure loss along the riser tubes is due to two effects, friction (ΔP_f) and acceleration (ΔP_a) [28]

$$\Delta P_2 = \Delta P_f + \Delta P_a \tag{2.28}$$

The pressure drop due to friction in the two-phase flow is

$$\Delta P_f = 4 f_2 \frac{H}{D_2} \frac{v_f}{2} \left(\frac{\dot{m}}{A_2} \right)^2 r_3 \tag{2.29}$$

where D_2 is the inner diameter of one riser tube, r_3 is the dimensionless friction factor for

two phase flow [28] (see Fig. 2.3), and A_2 is the cross section area of all the riser tubes,

$$A_2 = N\frac{\pi D_2^2}{4} \tag{2.30}$$

In accordance with the model used for the downcomer, we also define the riser flow velocity, friction factor and Reynolds number:

$$V_2 = \frac{\dot{m}/N}{\rho_2(\pi/4)D_2^2} \tag{2.31}$$

$$f_2(Re_2) = \frac{1}{4(1.82\log_{10}Re_2 - 1.64)^2} \tag{2.32}$$

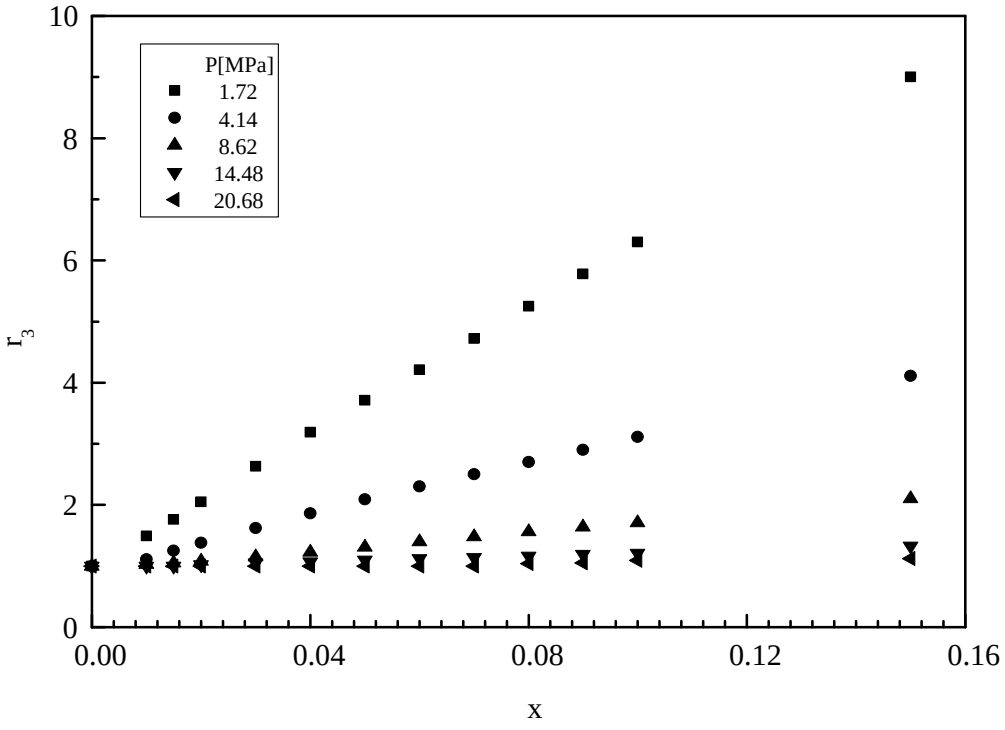

Figure 2.3: The r_3 factor for two-phase mixture frictional pressure drop.

$$Re_2 = \frac{V_2 D_2}{\nu_2} = \frac{\dot{m}/N}{(\pi/4) D_2 \mu_2} \tag{2.33}$$

The pressure drop due to acceleration in two phase flow is

$$\Delta P_a = v_f \left(\frac{\dot{m}}{A_2} \right)^2 r_2 \tag{2.34}$$

where r_2 is the dimensionless acceleration factor [28], shown here in Fig. 2.4. Substituting the pressure drop terms in Eq. (2.23), we obtain the global flow resistance equation for the self-pumping flow system:

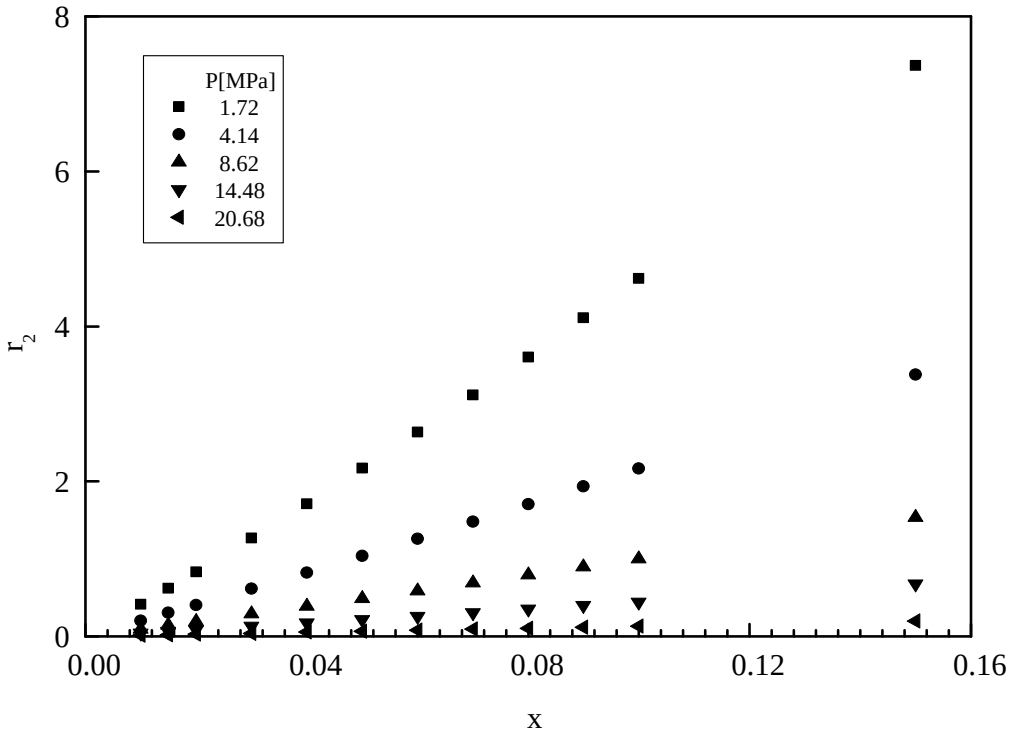

Figure 2.4: The r_2 factor for two-phase mixture acceleration pressure drop.

$$\frac{g\pi^2\rho_1^2 H}{32\dot{m}^2}\left(1 - r_4\right) = \frac{r_2}{2N^2 D_2^4} + \frac{f_1 H}{D_1^5} + \frac{r_3 f_2 H}{N^2 D_2^5} \tag{2.35}$$

The left side is a global flow resistance indicator, which in turbulent flow is essentially the driving pressure difference divided by $\dot{m}^2$. The constant volume constraint is shown in Eq. (2.5). The length scale of the flow structure is indicated by Eq. (2.5), where we set $D_{1,2} \sim L$:

$$L = \left(\frac{4V}{\pi H}\right)^{1/2} \tag{2.36}$$

From this length scale follow the dimensionless tube sizes

$$\tilde{D}_1 = \frac{D_1}{L}, \qquad \tilde{D}_2 = \frac{D_2}{L} \tag{2.37}$$

and the dimensionless flow volume constraint:

$$\tilde{D}_1^2 + N\tilde{D}_2^2 = 1 \tag{2.38}$$

The scale of the mass flow rate ($\dot{m}_{scale}$) follows from Eq. (2.35), where we write $\dot{m} \sim \dot{m}_{scale}$ and $D_{1,2} \sim L$,

$$\frac{g\pi^2\rho_1^2}{32\dot{m}_{scale}^2} = \frac{f}{L^5} \tag{2.39}$$

therefore,

$$\dot{m}_{scale} = \rho_1 g^{1/2}\left(\frac{4V}{\pi H}\right)^{5/4} \tag{2.40}$$

$$\tilde{H} = \frac{H}{L}, \qquad \tilde{m} = \frac{\dot{m}}{\dot{m}_{scale}} \tag{2.41}$$

The dimensionless version of Eq. (2.35) becomes

$$\frac{\pi^2}{32}\frac{\tilde{H}}{\tilde{m}^2}\left(1 - r_4\right) = \frac{r_2}{2N^2\tilde{D}_2^4} + \frac{f_1\tilde{H}}{\tilde{D}_1^5} + \frac{r_3}{N^2}\frac{f_2\tilde{H}}{\tilde{D}_2^5} \tag{2.42}$$

where

$$Re_1 = \frac{B_1\tilde{m}}{\tilde{D}_1}, \qquad Re_2 = \frac{B_2\tilde{m}}{N\tilde{D}_2} \tag{2.43}$$

$$B_1 = \frac{4}{\pi}\frac{g^{1/2}}{\nu_1}L^{3/2}, \qquad B_2 = \frac{4}{\pi}\frac{g^{1/2}}{\nu_2}L^{3/2} \tag{2.44}$$

Two dimensions, $\tilde{D}_1$ and $\tilde{D}_2$, vary but in view of the volume constraint (2.38) only one parameter is free to vary, for example the ratio $\tilde{D}_1/\tilde{D}_2$. According to the method of Lagrange multipliers (Section 2.1), we form the linear combination of the right hand sides of Eqs. (2.38) and (2.42),

$$\Phi = \frac{r_2}{2N^2\tilde{D}_2^4} + \frac{f_1\tilde{H}}{\tilde{D}_1^5} + \frac{r_3}{N^2}\frac{f_2\tilde{H}}{\tilde{D}_2^5} + \lambda\left(\tilde{D}_1^2 + N\tilde{D}_2^2\right) \tag{2.45}$$

and solve the system $\partial\Phi/\partial\tilde{D}_1 = 0$ and $\partial\Phi/\partial\tilde{D}_2 = 0$. After eliminating λ, we obtain

$$N^3\left(\frac{\tilde{D}_2}{\tilde{D}_1}\right)^7 = \frac{2r_2\tilde{D}_2}{5f_1\tilde{H}} + \frac{r_3f_2}{f_1} \tag{2.46}$$

The second term dominates on the right-hand side of Eq. (2.46) when

$$\frac{\tilde{D}_2}{\tilde{H}} << \frac{5r_3}{2r_2} f_2 \tag{2.47}$$

and in this limit Eq. (2.46) delivers the optimal ratio of tube diameters

$$\left(\frac{\tilde{D}_1}{\tilde{D}_2}\right)_{opt} = \left(N^3 \frac{f_1}{f_2 r_3}\right)^{1/7} \tag{2.48}$$

The assumption (2.47) is justified because the height is much greater than the diameter of the riser tubes ($D_2/H \sim 10^{-4}$), the factor r_3 is significantly greater than the acceleration factor r_2, and f_2 is of order 10^{-2} [28]. Even though r_2 approaches r_3 when P < 5 MPa and the liquid-vapor mixture quality (x) is greater than 0.1, the ratio $5r_3f_2/2r_2$ is of order 10^{-2}, i.e. much greater than the ratio D_2/H.

Equation (2.48) resembles Eq. (2.7), which came from a much simpler model. The effect of two phase flow in the riser is conveyed by r_3, which depends on pressure P and quality x [28]. In order to calculate the $\tilde{D}_1/\tilde{D}_2$ of Eq. (2.48) we need to account for the flow regime [Eqs. (2.27) and (2.32)] and the mass flow rate. The latter comes from the minimized flow resistance, which is obtained by combining Eqs. (2.48) and (2.38) with Eq. (2.42),

$$\left[\frac{\pi^2}{32}\frac{\tilde{H}}{\tilde{m}^2}(1-r_4)\right]_{min} = \frac{r_2\left(K^2+N\right)^2}{2N^2} + \frac{f_1\tilde{H}\left(K^2+N\right)^{5/2}}{K^5} + \frac{r_3}{N^2} f_2\tilde{H}\left(K^2+N\right)^{5/2} \tag{2.49}$$

where $K = (N^3 f_1/f_2 r_3)^{1/7}$. The results presented in the next section are based on assuming the same global parameters as in Section 2.2, for example $V = 47\ m^3$ and $H = 36$ m. The

resulting range for the mass flow rate is such that the Reynolds numbers calculated with Eqs. (2.26) and (2.33) vary in the ranges $1.9 \times 10^7 < \mathrm{Re}_1 < 1.4 \times 10^8$ and $3 \times 10^5 < \mathrm{Re}_2 < 1.2 \times 10^8$.

2.4 The effect of operating pressure

The results developed in the preceding sections are sensitive to the pressure in the loop and the quality of the two-phase mixture in the riser tubes. These effects are investigated systematically in Figs. 2.5–2.11, and can be anticipated based on the simple model of Section 2.1.

We begin with Fig. 2.5a, where we set P = 13.8 MPa and recognized [based Eq. (2.48)] that $\left(\tilde{D}_1/\tilde{D}_2\right)_{\mathrm{opt}}$ should be proportional to $N^{3/7}$. Even though we plotted $\left(\tilde{D}_1/\tilde{D}_2\right)_{\mathrm{opt}}/N^{3/7}$ on the ordinate, a weak N effect continues to be present. Stronger is the effect of the quality x, which was given values in the range 0.02 - 0.12. The x effect is captured by the factor $x^{-0.043}$, which appears in the ordinate of Fig. 2.5b. The exponent -0.043 was determined by minimizing the scatter that is still visible in Fig. 2.5b. The conclusion is that for P = 13.8 MPa the optimal allocation of flow volume is represented by

$$\left(\frac{\tilde{D}_1}{\tilde{D}_2}\right)_{\mathrm{opt}} = \left(0.77 \pm 0.02\right) N^{3/7} x^{-0.043} \qquad (2.50)$$

The corresponding maximized mass flow rate $\tilde{m}_{\max}$ is reported in Fig. 2.6a. The

sensitivity of $\tilde{m}_{max}$ to N changes as N increases, namely from $\tilde{m}_{max} \sim N^{-1/8}$ to $\tilde{m}_{max} \sim N^{-1/4}$. Figure 2.6b shows the effect of x, which is a rough proportionality between $\tilde{m}_{max}$ and $x^{0.35}$. Together, these power-law trends lead to the dimensionless correlations reported in Fig. 2.7, namely

$$\begin{aligned} \tilde{m}_{max} &= (2.75 \pm 0.14) N^{-1/8} x^{0.35}, \quad (N \lesssim 50) \\ \tilde{m}_{max} &= (4.28 \pm 0.16) N^{-1/4} x^{0.35}, \quad (N \gtrsim 50) \end{aligned} \tag{2.51}$$

The trends change somewhat when the pressure changes. Fig. 2.8 shows the P = 0.5 MPa equivalent of Fig. 2.5b. This time, instead of Eq. (2.50) the optimal ratio of diameters is correlated by

$$\left(\frac{\tilde{D}_1}{\tilde{D}_2} \right)_{opt} = (0.33 \pm 0.01) N^{0.45} x^{-0.15} \tag{2.52}$$

Here the N exponent 0.45 is consistent with the N exponent in Eq. (2.48), namely 3/7 = 0.43. The maximized mass flow rate at P = 0.5 MPa is correlated in Fig. 2.9, as follows :

$$\begin{aligned} \tilde{m}_{max} &= (0.24 \pm 0.01) N^{-0.075} x^{-0.31}, \quad (N \lesssim 50) \\ \tilde{m}_{max} &= (0.48 \pm 0.01) N^{-0.26} x^{-0.31}, \quad (N \gtrsim 50) \end{aligned} \tag{2.53}$$

The effect of pressure is documented further in Fig. 2.10. As the pressure increases, the optimal diameter ratio $(\tilde{D}_1 / \tilde{D}_2)_{opt}$ increases for every value of x. The maximum mass flow rate exhibits a more complicated behavior. At low pressures, the maximum mass flow rate decreases as the quality increases. At pressures above 2 MPa, the maximum

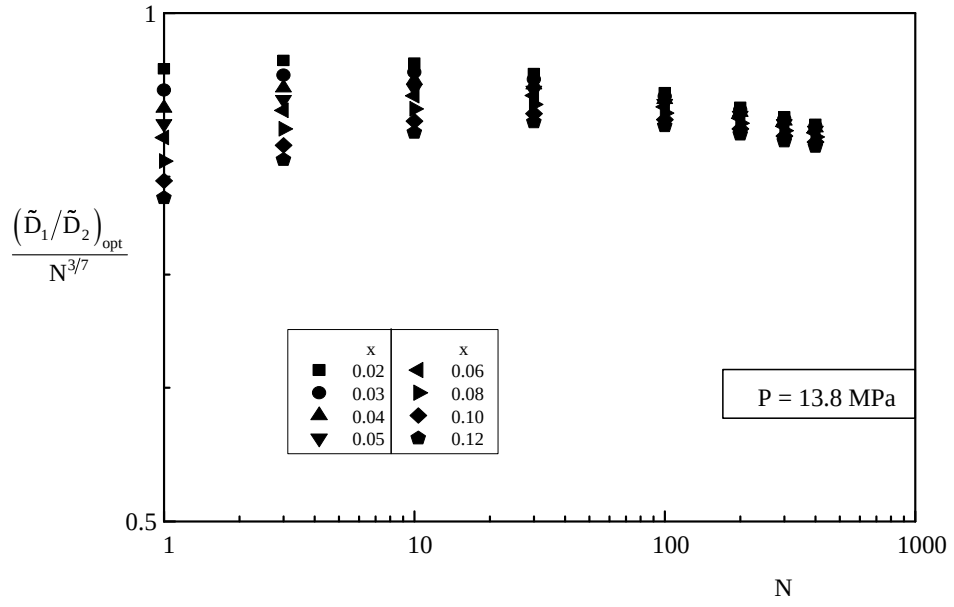

(a)

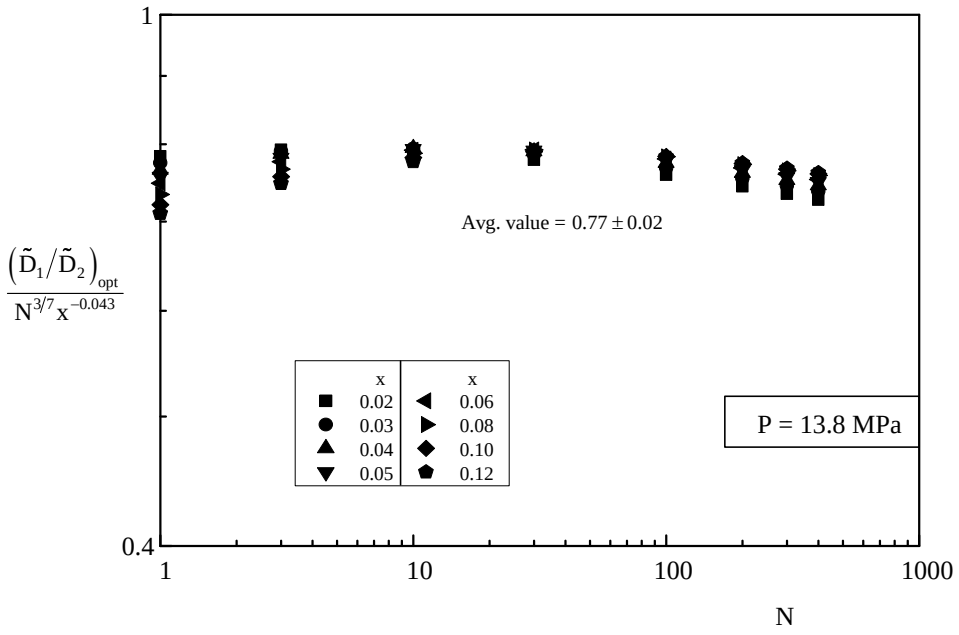

(b)

Figure 2.5: (a) The effect of N and x on the optimal diameter ratio.
(b) Optimal diameter ratio correlation when 13.8 MPa.

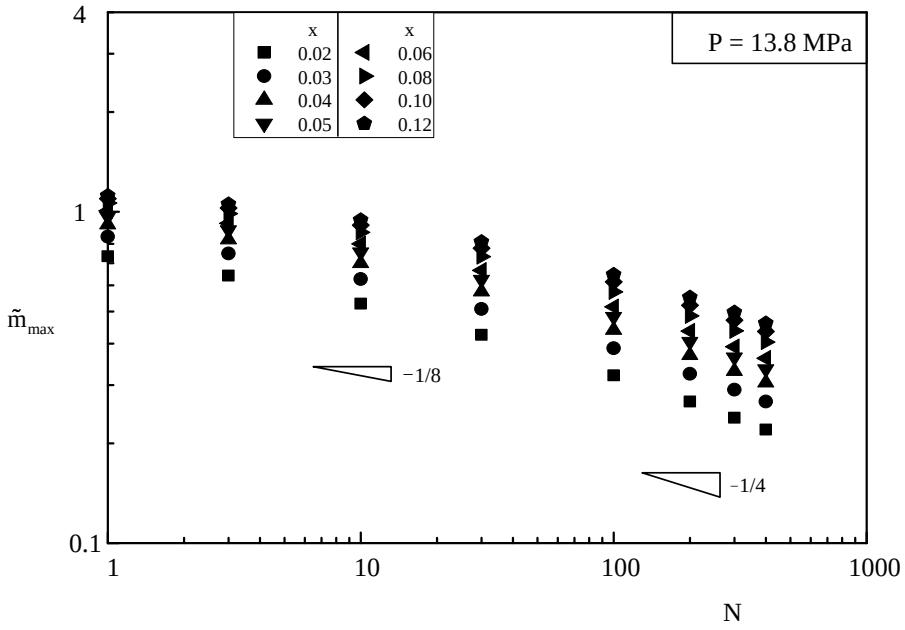

(a)

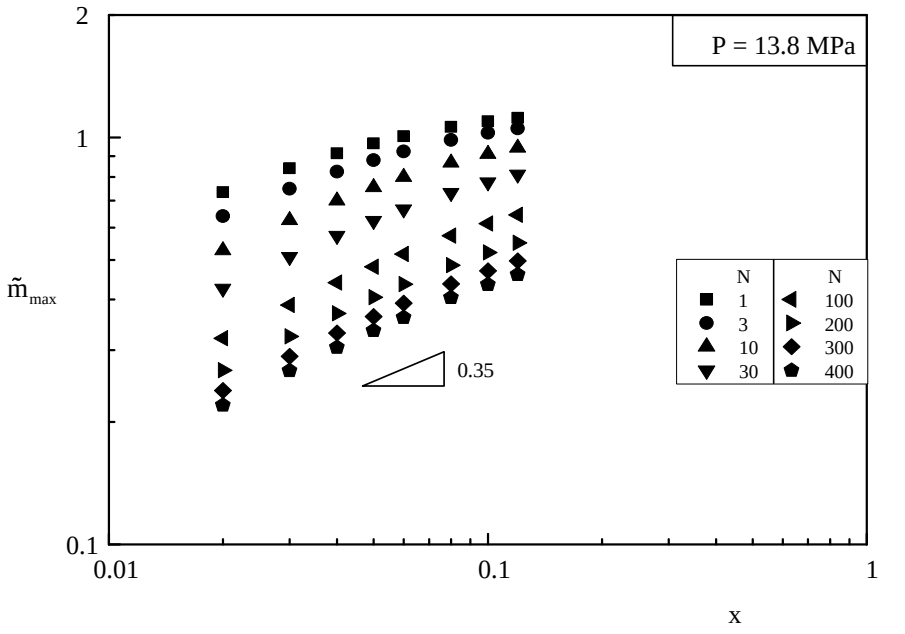

(b)

Figure 2.6: (a) The effect of N on the dimensionless maximum mass flow rate.
(b) The effect of x on the dimensionless maximum mass flow rate when 13.8 MPa..

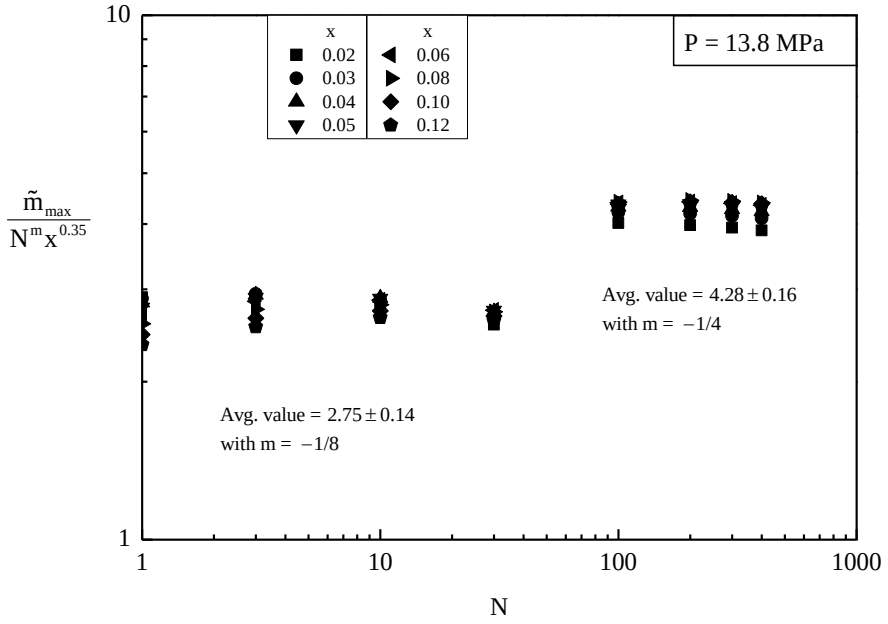

Figure 2.7: Correlation of the dimensionless maximum mass flow rate for 13.8 MPa.

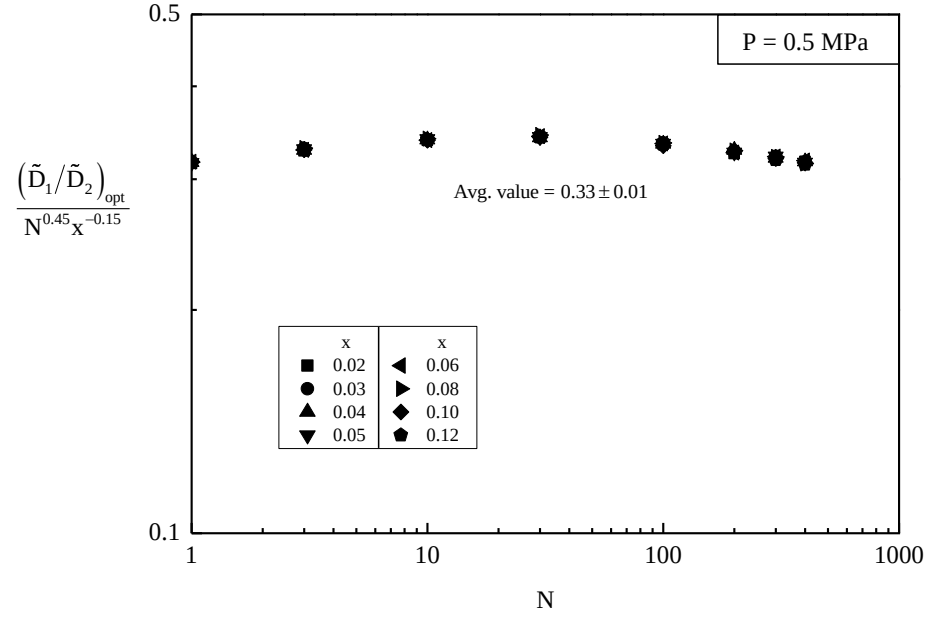

Figure 2.8: Optimal diameter ratio correlation for 0.5 MPa.

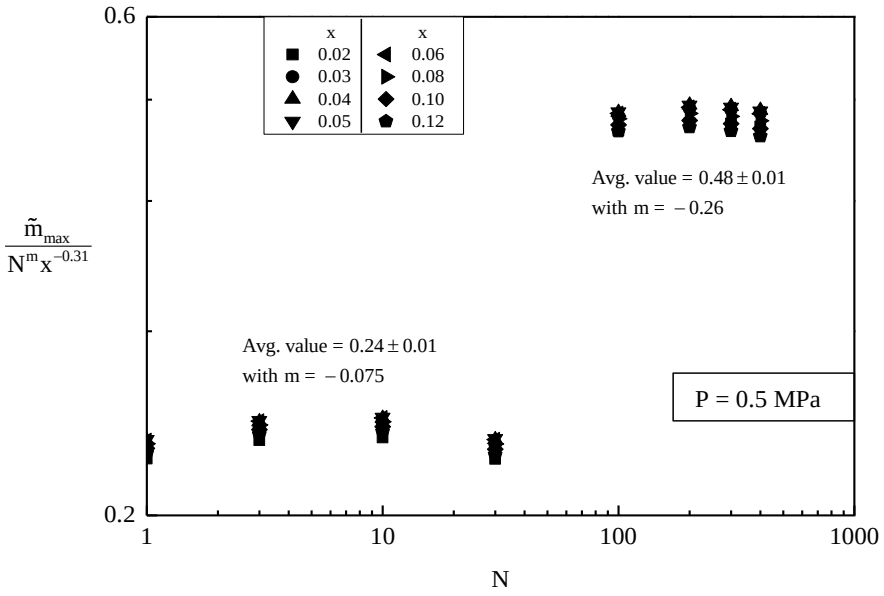

Figure 2.9: Correlation of the dimensionless maximum mass flow rate for 0.5 MPa.

mass flow rate increases with quality.

This reversal in how $\tilde{m}_{max}$ depends on x is explained by the analytical solution developed in Section 2.1. If we take the mass flow rate maximized in Eq. (2.9) and nondimensionalize it in accordance with Eqs. (2.40) and (2.41) we obtain

$$\tilde{m}_{max} = 2^{-5/2}\pi f_2^{-1/2} N^{-1/4} \frac{\left(x v_f v_{fg}\right)^{1/2}}{v_f + x v_{fg}} \tag{2.54}$$

where we replaced ρ_1^{-1} with the specific volume of saturated liquid, $v_f(P)$. We also replaced ρ_2^{-1} with $(v_f + x v_{fg})$, where $v_{fg} = v_g - v_f$ and $v_g(P)$ is the specific volume of saturated vapor. In the limit $x << 1$, the denominator $(v_f + x v_{fg})$ depends on pressure in two ways. When the pressure is sufficiently low, v_f is negligible relative to $x v_{fg}$ and

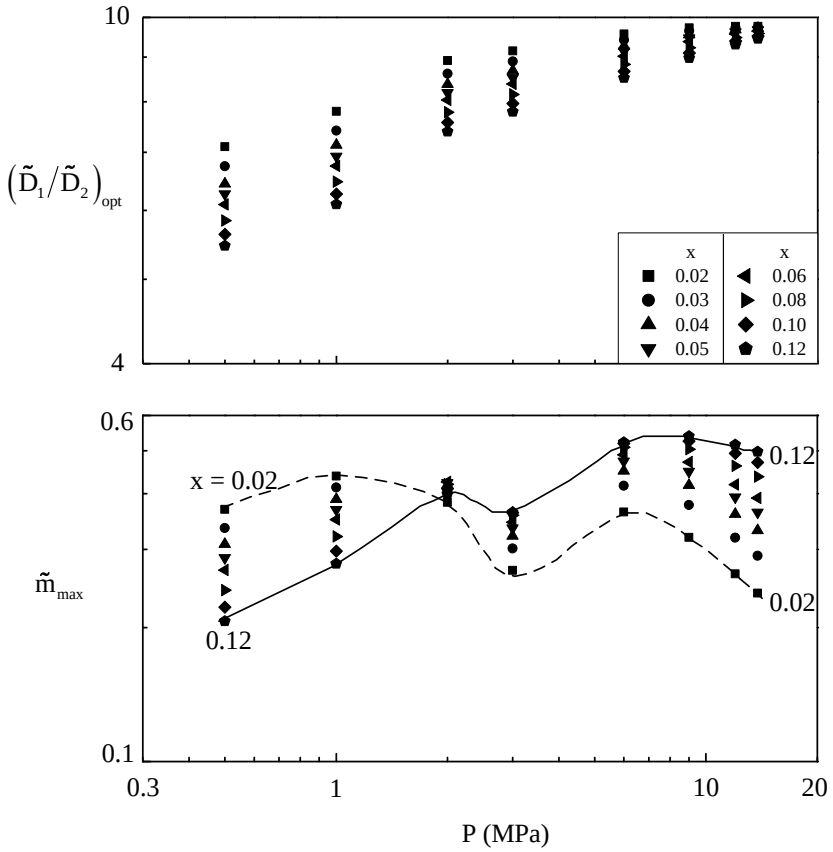

Figure 2.10: The effect of pressure on the optimal diameter ratio and the dimensionless maximum mass flow rate.

Eq. (2.54) approaches

$$\tilde{m}_{max,\,low\,P} \cong \left[2^{-5/2}\pi f_2^{-1/2}\left(\frac{v_f}{v_{fg}}\right)^{1/2}\right] N^{-1/4} x^{-1/2} \tag{2.55}$$

As P approaches the critical pressure, the difference between v_g and v_f disappears and xv_{fg} is negligible relative to v_f. In this limit Eq. (2.54) approaches

$$\tilde{m}_{max,\,high\,P} \cong \left[2^{-5/2}\pi f_2^{-1/2}\left(\frac{v_{fg}}{v_f}\right)^{1/2}\right] N^{-1/4} x^{1/2} \tag{2.56}$$

Equations (2.55) and (2.56) confirm qualitatively the dependence of $\tilde{m}_{max}$ on N and x, which was correlated as Eqs. (2.53) and (2.51), respectively. See the correlations reported for $N \gtrsim 50$. Dividing Eqs. (2.55) and (2.56), we see that the transition from one behavior to the other occurs when the pressure P is such that

$$\frac{v_f(P)}{v_{fg}(P)} \cong x \tag{2.57}$$

This relationship between x and P has been plotted for water in Fig. 2.11, and it divides the x - P domain into the two subdomains in which Eqs. (2.51) and (2.53) apply.

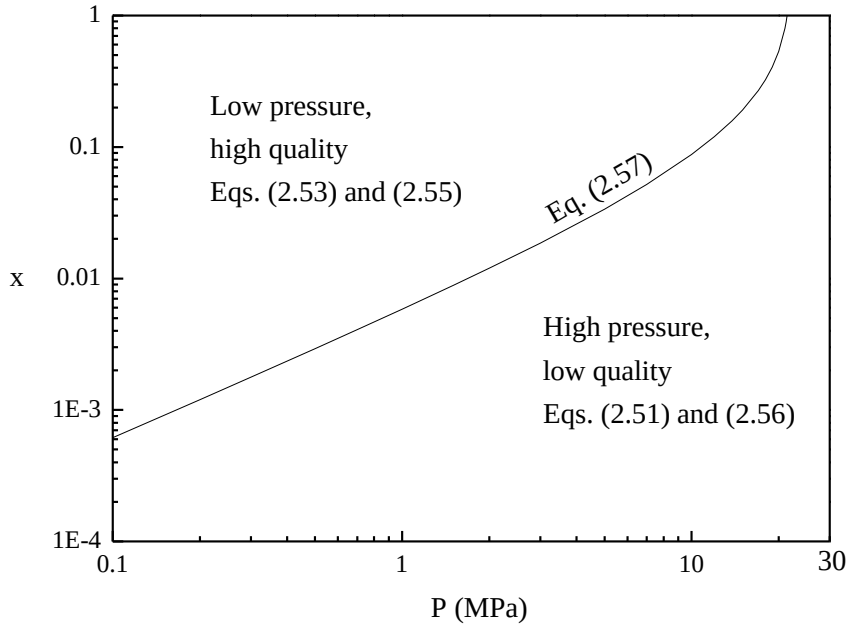

Figure 2.11: The relationship x(P) that serves as boundary between the domain of applicability of Eqs. (2.55) and (2.56).

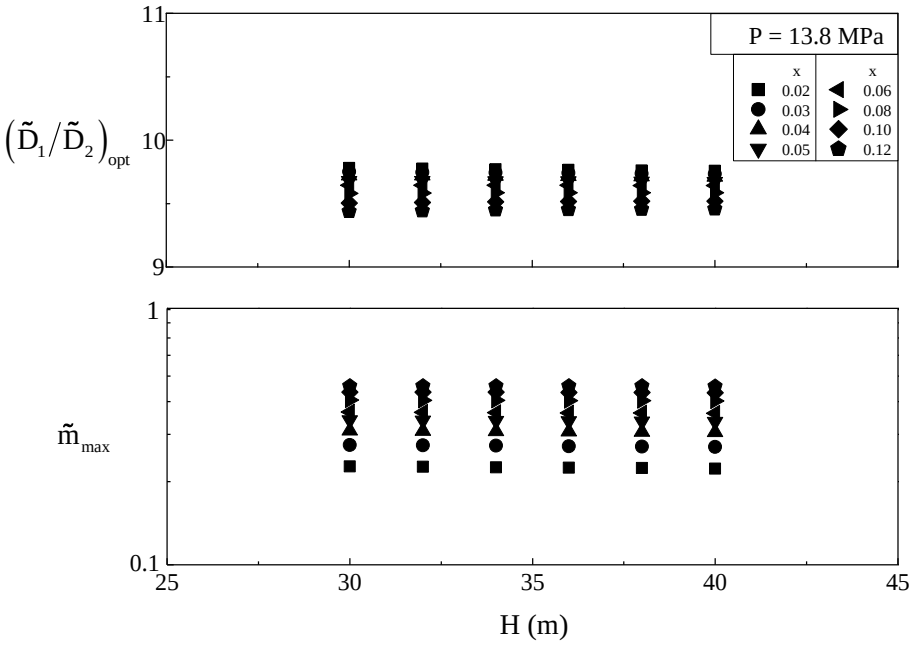

Figure 2.12: The effect of H on the optimal diameter ratio and the dimensionless maximum mass flow rate when 13.8 MPa.

In closing, we relaxed the assumption that the height H is fixed, and investigated the effect of H on the main features of the design, $\left(\tilde{D}_1/\tilde{D}_2\right)_{opt}$ and $\tilde{m}_{max}$. Figure 2.12 shows that these features are insensitive to H. This can be also shown analytically, because, when the assumption (2.47) is valid, $\tilde{H}$ drops out from Eq. (2.42), leaving only

$$\frac{\pi^2}{32\tilde{m}^2}\left(1 - r_4\right) = \frac{f_1}{\tilde{D}_1^5} + \frac{r_3}{N^2}\frac{f_2}{\tilde{D}_2^5} \tag{2.58}$$

2.5 Results and discussion

A practical aspect that is consistent with the present results is that engineers have long classified steam generators according to pressure. In other words, the pressure is an

essential factor in the design of the steam generator. The constructal design developed in this chapter sheds light on the effect of pressures on the main geometric characteristics of steam generator architecture. The results obtained with the two phase flow model show that the optimal configuration of the steam generator is pressure dependent because the quality depends on the pressure and is a crucial factor in minimizing the global flow resistance. This observation is consistent with current designs of steam generators, which have evolved based on the “design, build and test method” over a long time. The designs show different configurations, one for each pressure.

Equations for geometric dimensions can shorten time for the evolution of engineered products. The steam generator has evolved over 100 years based on the old paradigms such as “cut and try” and “design, build and test” methods. These old approaches stand on experience; so, they have a limited capability against the variation of the design and operation conditions. For example, the change of the working fluid from water to mercury might requires a long time to reach the optimal configuration because the geometric dimensions are a function of properties of the working fluid as shown in Eqs. (2.10), (2.11), (2.22), (2.50) and (2.52); so, the configuration of the mercury steam generator should be different from one of the steam generator. Constructal theory enables engineers not to rely on the old approaches in searching the best configuration. Constructal design can guide engineers to find the optimal drawing for the various design and operation conditions.

What we showed here for the design of the steam generator can and should be extended to the other components of the power plant. Each owes its thermodynamic imperfection to its finite size and flow configuration. The finite size can not be changed, at least at the component – concept stage. The flow configuration can be changed, and this is the path to discovering less and less imperfect components for a given size.

3. Continuous Steam Generator Architecture

In the chapter 2, we showed that the configuration of a steam generator can be deduced based on constructal design. This was a simple demonstration of the design method, which was based on the simplifying assumption that the steam generator consists of just two parts, riser and unheated downcomer. Here we consider the more promising design direction where the steam generator is free to have a large number of tubes, so many that its material can be distributed through the available volume. Steam generators with many tubes are the preferred configuration in the power generation industries when the pressure becomes low [21, 22, 31]. In this chapter we consider large numbers of steam tubes, such that the steam generator architecture can be modeled as continuous (Fig. 3.1).

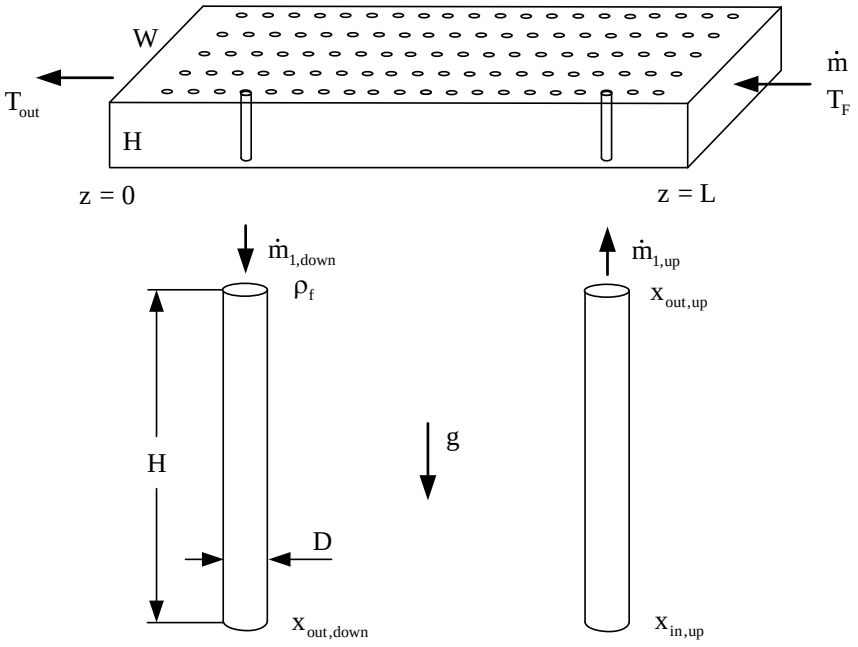

Figure 3.1: Steam generator with a large number of vertical two-phase tubes in crossflow with a horizontal stream of hot gases.

Consider the flow of high-temperature gas across bundle of water tubes shown Fig. 3.1. The steam generator fills a parallelepipedic volume HLW, which is traversed by N equidistant steam tubes of diameter D and height H. Two volume constraints are in place: the total volume occupied by hot gas, and the total volume of water tubes.

Hot combustion gases of capacity rate $\dot{m}c_p$ and inlet temperature T_F flow from right to left. Steam flows in crossflow, inside the tubes, being driven in a vertical loop by the thermosyphon effect due to the fact that the tubes close to z = L are heated more intensely than the tubes close to z = 0. The temperature of hot flue gas is not high enough to transform the water in the tubes into superheated steam at the outlet of each water tube; so, the temperature of water in the tubes remains constant at the boiling temperature T_B corresponding to pressure of the upper and lower plenums, which receive and separate the steam generated in the tubes.

The net mass flow rate of water through a horizontal plane across all the tubes is zero. The flow rate of the circulated water rate and the flow architecture, i.e. the location of the flow reversal, are unknown. In this chapter we seek to configure the continuous steam generating system such that it generates most steam.

3.1 Longitudinal temperature distribution

The geometric constraints of this counterflow heat exchanger are the total volume,

$$V = HLW \tag{3.1}$$

and the volume fraction occupied by water,

$$\phi = \frac{\pi}{4}\frac{D^2 N}{LW} \tag{3.2}$$

The stream of hot gases is modeled as single-phase with constant properties. Assuming that N is sufficiently large so that we may treat the gas temperature T as a continuous function of longitudinal portion z, we write that the hot stream loses enthalpy to match the transfer of heat to the tubular structure T_B,

$$\dot{m}c_p dT = \frac{hA}{L}\left(T - T_B\right)dz \tag{3.3}$$

We assume that the heat transfer coefficient h is a known constant, at best a function of the gas flow rate $\dot{m}$, which is also specified. Integrating Eq. (3.3) from z = 0 where T = T_{out}, to z we obtain

$$T(z) - T_B = \left(T_{out} - T_B\right)\exp\left(\frac{hA}{\dot{m}c_p L}z\right) \tag{3.4}$$

or, because the overall temperature difference $\Delta T = T_F - T_B$ is specified,

$$T(z) - T_B = \Delta T\frac{\exp\left(hAz/\dot{m}c_p L\right)}{\exp\left(hA/\dot{m}c_p\right)} \tag{3.5}$$

In sum, the temperature difference $T - T_B$ varies continuously in the longitudinal direction, and so does the heat transfer rate from the gas to the water in the tubes, regardless of the water direction and flow rate in the tubes. For example, the heat transfer rate into one tube located at position z is

$$h\pi DH\left(T - T_B\right) = \dot{m}_1\left(h_{out} - h_{in}\right) \tag{3.6}$$

where $\dot{m}_1$ is the water mass flow rate through the tube, and

$$h_{in} = h_f \tag{3.7}$$

$$h_{out} = h_f + x_{out}h_{fg} \tag{3.8}$$

In Eq. (3.7) we are assuming that the stream received by every tube from the plenum contains saturated liquid. The steam quality at the tube exit is related to the specific volume of the steam at the exit,

$$v_{out} = v_f + x_{out}v_{fg} \tag{3.9}$$

or, in terms of densities,

$$\frac{\rho_{out}}{\rho_f} = \frac{1}{1 + x_{out}v_{fg}\rho_f} \tag{3.10}$$

Eliminating x_{out} between Eqs. (3.6) -(3.10) we find

$$h\pi DH\left(T - T_B\right) = \frac{\dot{m}_1 h_{fg}}{\rho_f v_{fg}}\left(\frac{\rho_f}{\rho_{out}} - 1\right) \tag{3.11}$$

where $(T - T_B)$ is a known function of longitudinal position, Eq. (3.5).

3.2 Flow reversal

The mass flow rate $\dot{m}_1$ is driven by the weight of its liquid column relative to the weight of the neighboring columns. If the hydrostatic pressure difference between the two

plenums is

$$\Delta P_{ref} = \rho_{ref} gH \tag{3.12}$$

where ρ_{ref} is the reference density in a column of height H, then the net pressure difference that drives $\dot{m}_1$ *upward* through its tube is

$$\Delta P_1 = \left(\rho_{ref} - \rho_1\right) gH \tag{3.13}$$

Here ρ_1 is the average density of the two-phase mixture in the $\dot{m}_1$ tube. Approximating the distribution of density of two-phase water as linear along the tube, we estimate the average density

$$\rho_1 \cong \frac{\rho_f + \rho_{out}}{2} \tag{3.14}$$

The water flow rate $\dot{m}_1$ is driven by ΔP_1. We illustrate this qualitatively with the simplest model of flow fiction in a tube, namely fully developed turbulent (fully rough) and single phase fluid,

$$\frac{\Delta P_1}{H} = C\frac{\dot{m}_1^2}{D^5} \tag{3.15}$$

where the factor is $C = 32fv/\pi^2$, and f is the friction coefficient, which in the fully rough regime is practically constant. A more detailed two-phase flow model is presented in Section 3.5. Eliminating $\dot{m}_1$ and ρ_{out}/ρ_f between Eqs. (3.11) -(3.15) we obtain

$$h\pi DH\Delta T\frac{\theta}{B}\left(\frac{C}{gD^5}\right)^{1/2} = \left(\rho_{ref} - \rho_1\right)^{1/2} \tag{3.16}$$

where $(\rho_{ref} - \rho_1)^{1/2}$ is proportional to $\dot{m}_1$, and

$$\theta = \frac{\exp\left(hAz/\dot{m}c_pL\right)}{\exp\left(hA/\dot{m}c_p\right)} \tag{3.17}$$

$$B = \frac{h_{fg}}{\rho_f v_{fg}}\left(\frac{\rho_f}{\rho_{out}} - 1\right) \tag{3.18}$$

Equations (3.13)-(3.17) show that $\dot{m}_1$ varies longitudinally in proportion with $\exp\left(hAz/\dot{m}c_pL\right)$, regardless of whether the flow is up or down. The change in direction occurs at the longitudinal location (z_c) obtained by requiring

$$\int_0^L \dot{m}_1 dz = 0 \tag{3.19}$$

The result is

$$\frac{z_c}{L} = \frac{1}{N_{tu}}\ln\frac{1+e^{N_{tu}}}{2} \tag{3.20}$$

where

$$N_{tu} = \frac{hA}{\dot{m}c_p} \tag{3.21}$$

3.3 Geometry on the gas side

Consider the hot-gas side of the counterflow heat exchanger, and ask how the geometry affects the global performance. The geometry is represented by the total volume

V = HLW, which is fixed, and by the dimensions H, L, W, D and S, where S is the spacing between adjacent tubes (Fig. 3.2).

If we use $V^{1/3}$ as the fixed length scale of the entire architecture, then there are five dimensionless geometrical features,

$$\left(\tilde{H},\ \tilde{L},\ \tilde{W},\ \tilde{D},\ \tilde{S}\right) = \left(H,\ L,\ W,\ D,\ S\right) / V^{1/3} \tag{3.22}$$

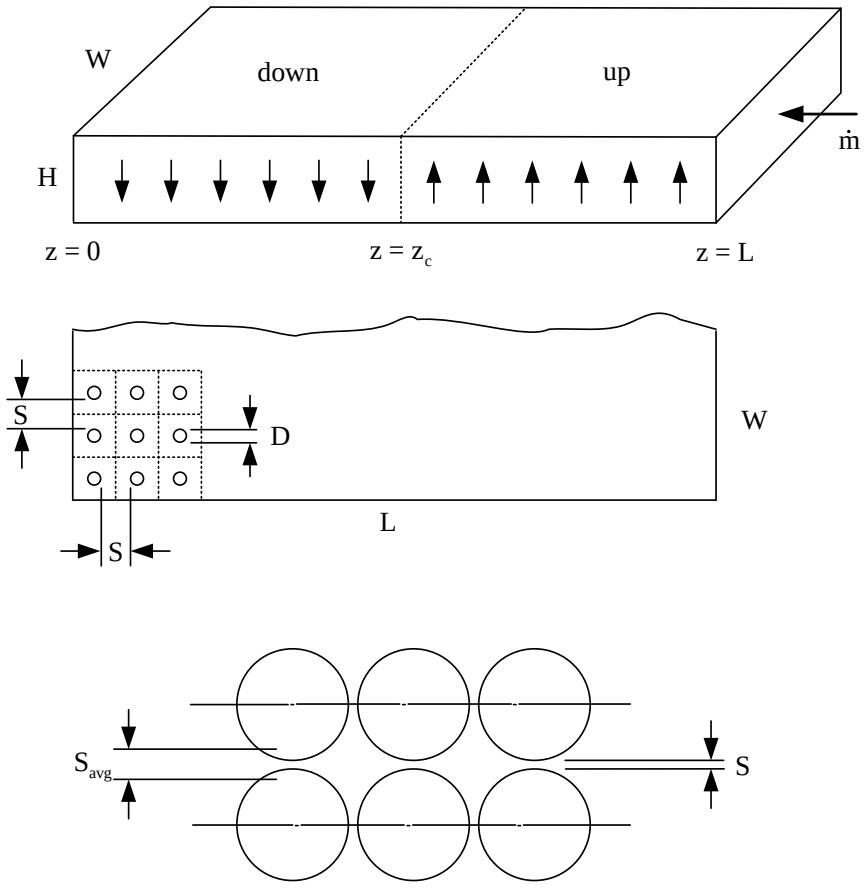

Figure 3.2: Geometric details of the steam generator, viewed from the side and from above.

and one constant

$$\tilde{H}\tilde{L}\tilde{W} = 1 \tag{3.23}$$

In sum, the architecture design has four degrees of freedom. Equation (3.3) shows that the total heat transfer rate from the hot gas to all the tubes is

$$\begin{aligned} q &= \dot{m}c_P\left(T_F - T_{out}\right) \\ &= \dot{m}c_P\Delta T\left(1 - e^{-N_{tu}}\right) \end{aligned} \tag{3.24}$$

where $\Delta T = T_F - T_B$, fixed.

Fixed is also the pressure difference (ΔP_F) that drives the gas stream horizontally through the multi-tube structure. When the spacing between tubes (S) is large, the thermal contact between gas and tubes is poor ($N_{tu} << 1$), and q is small. When the spacing is vanishingly small, the mass flow rate ($\dot{m}$) vanishes and so does q. Between these two S extremes there must be an optimal spacing for which q is maximum when the remaining three geometrical features are fixed (for example, $\tilde{D}$, $\tilde{H}$ and $\tilde{L}$). This expectation is supported by several designs developed in constructal theory [2, 4], where optimal spacings were predicted and validated experimentally [32] for parallel and staggered plates and cylinders in cross-flow. Here we pursue the optimal spacings by focusing on Eq. (3.24) when only S varies. In order to calculate q with Eq. (3.24) we need $\dot{m}$ and N_{tu}. The following analysis is based on the intersection of asymptotes method [2].

(a) The large–S limit. First, we assume that S is sufficiently larger than D so that

the drag force on each tube is independent of the flow around neighboring tubes. The drag force on the tube is

$$F_1 = C_D H D \frac{1}{2} \rho U^2 \tag{3.25}$$

Because of the large spacings, the free stream velocity of the hot gas is

$$U \cong \frac{\dot{m}}{\rho_F H W} \tag{3.26}$$

where the gas density ρ_F is treated as a constant. The total drag force experienced by the assembly is

$$F = F_1 \frac{L}{S} \frac{W}{S} \tag{3.27}$$

This force is balanced by $\Delta P_F HW$, and from this balance we deduce the mass flow rate in the (a) limit,

$$\dot{m}_a = \left(\Delta P_F \rho_F \frac{2}{C_D} \frac{H^2 W^2 S^2}{L D} \right)^{1/2} \tag{3.28}$$

Next, Eq. (3.21) requires estimates for A_a and h_a. The total contact area is

$$A_a = \pi D H \frac{L}{S} \frac{W}{S} = \frac{\pi D V}{S^2} \tag{3.29}$$

The heat transfer coefficient for a long cylinder is (e.g. Ref. [33]):

$$\frac{h_a D}{k_F} = 0.3 + \frac{0.62 Pr_F^{1/3} Re_D^{1/2}}{\left[1 + (0.4/Pr_F)^{2/3}\right]^{1/4}} \left[1 + \left(\frac{Re_D}{282000} \right)^{5/8} \right]^{4/5} \tag{3.30}$$

where k_F and Pr_F are properties of the hot gas. When $10 < Re_D < 10^5$, Eq. (3.30) is

approximated adequately by

$$\frac{h_a D}{k_F} \cong C_a \, Re_D^{1/2} \tag{3.31}$$

where C_a is a dimensionless factor of order 1,

$$C_a = \frac{0.62 Pr_F^{1/3}}{\left[1 + (0.4/Pr_F)^{2/3}\right]^{1/4}} \left[1 + \left(\frac{Re_D}{282000}\right)^{5/8}\right]^{4/5} \tag{3.32}$$

and $Re_D = UD/\nu_F$, with U being provided by Eq. (3.26). In the end, Eq. (3.21) yields

$$N_{tu,a} = \frac{\pi C_a k_F}{c_P \mu_F^{1/2}} \frac{VD^{1/2}}{S^2 H^{1/2} W^{1/2} \dot{m}_a^{1/2}} \tag{3.33}$$

Finally, in the large-S limit the number $N_{tu,a}$ approaches zero, and this means that the group $\left(1 - e^{-N_{tu,a}}\right)$ approaches $N_{tu,a}$, and that Eq. (3.24) approaches the asymptote

$$q_a = \left(\frac{2}{C_D}\right)^{1/4} \pi C_a \frac{k_F \rho_F^{1/4}}{\mu_F^{1/2}} \Delta T \Delta P_F^{1/4} \frac{VD^{1/4}}{S^{3/2} L^{1/4}} \tag{3.34}$$

This shows that the total heat transfer rate decreases monotonically as S increases. For this reason we turn our attention to the opposite limit, in which S decreases.

(b) The small-S limit. When the cylinders barely touch, the flow is slow, the thermal contact between the hot gas and the tubes is excellent, N_{tu} is a large number, and Eq. (3.24) reduces to

$$q_b = \dot{m} c_P \Delta T \tag{3.35}$$

The mass flow rate can be estimated by visualizing the channel of average spacing S_{avg}

inhabited by the stream lines that flow along L, through two adjacent rows of tubes. The smallest spacing (S) occurs where the stream channel is pinched by two tubes that almost touch. Because of the regular arrangement of tubes, we can write

$$S_{avg} = \sigma S \tag{3.36}$$

where σ is a factor of order 1, but greater than 1, for example 2. For the elemental channel represented by the volume $S_{avg} \times L \times H$, the mass flow rate in the Poissuille flow limit is

$$\dot{m}_{1,F} = \rho U_1 S_{avg} H \tag{3.37}$$

in which [33]

$$U_1 = \frac{S_{avg}^2}{12\mu_F}\frac{\Delta P_F}{L} \tag{3.38}$$

The number of such channels is W/D. The total mass flow rate is

$$\dot{m} = \frac{\Delta P_F}{12\nu_F}\frac{S_{avg}^3 V}{DL^2} \tag{3.39}$$

which in combination with Eqs. (3.35) and (3.39) yields

$$q_b = c_P \Delta T \frac{\Delta P_F}{12\nu_F}\frac{\sigma^3 S^3 V}{DL^2} \tag{3.40}$$

This shows that in the small-S limit the total heat transfer rate decreases steeply as S decreases.

(c) The intersection of asymptotes. The maximum of q with respect to S is located sufficiently accurately by intersecting the two asymptotes, Eqs. (3.34) and (3.40).

The result is

$$\tilde{S}_{opt} = \left[\left(\frac{2}{C_D} \right)^{1/4} \frac{12\pi C_a}{Pr_F^{1/4}\,\sigma^3} \right]^{2/9} Be^{-1/6} \tilde{D}^{5/18} \tilde{L}^{7/18} \tag{3.41}$$

$$Be = \frac{\Delta P_F V^{2/3}}{\alpha_F \mu_F} \tag{3.42}$$

where Eq.(3.42) shows the dimensionless pressure difference number introduced by Bhattacharjee and Grosshander [34] (see also Ref. [35]). The factor in square brackets in Eq. (3.41) is approximately 1, and can be replaced by 1. The mass flow rate that corresponds to $\tilde{S}_{opt}$ is

$$\dot{m}_{opt} = \left[\frac{\sigma^3}{12} \right] \frac{k_F}{c_P} V^{1/3} Be \frac{\tilde{S}^3}{\tilde{D}\tilde{L}^2} \tag{3.43}$$

and, if we regard the group $[\sigma^3/12]$ as a number of order 1 and use Eq. (3.41), we obtain

$$\dot{m}_{opt} \sim \frac{k_F}{c_P} V^{1/3} Be^{1/2} \tilde{D}^{-1/6} \tilde{L}^{-5/6} \tag{3.44}$$

$$q_{max} \sim k_F \Delta T V^{1/3} Be^{1/2} \tilde{D}^{-1/6} \tilde{L}^{-5/6} \tag{3.45}$$

The corresponding number of tubes in this optimal assembly is

$$n = \frac{L}{S}\frac{W}{S} = \frac{1}{\tilde{S}^2 \tilde{H}} \cong Be^{1/3} \tilde{D}^{-5/9} \tilde{L}^{-7/9} \tilde{H}^{-1} \tag{3.46}$$

Seen from the gas side, the maximized total heat transfer rate depends on two of the remaining free dimensions of the assembly, $\tilde{D}$ and $\tilde{L}$. The q_{max} value increases as

both $\tilde{D}$ and $\tilde{L}$ decrease: thinner tubes and a shorter gas-flow path are better for increasing the global heat transfer rate.

Another result of this analysis is that the scale of q_{max} is $k_F \Delta T V^{1/3}$, which means that q_{max} increases in proportion with the linear scale of the steam generator, $V^{1/3}$. The volumetric heat transfer density q_{max}/V decreases in proportion with $V^{-2/3}$.

In conclusion, if compactness is the goal, smaller steam generators have greater heat transfer density than larger steam generators. More specifically, if one large steam generator has the total heat transfer rate $q = C_q V^{1/3}$ when Be, $\tilde{D}$ and $\tilde{L}$ are fixed [cf. Eq. (3.45)], then two steam generators (each of half size V/2) will have the total heat transfer rate $2(q/2) = 2C_q(V/2)^{1/3}$, which exceeds by the factor $2^{2/3} = 1.59$ the q value of the single large steam generator. Alternatively, if we fix D and L of the V-size design, and divide V into two V/2 parts in which the tube diameters are D and the length scale of each V/2 part is $(1/2)^{1/3}L$ so that each part has the volume V/2, then the corresponding analysis shows that the combined heat transfer rate of the two parts exceeds by 21 percent the original heat transfer rate, $q = C_q V^{1/3}$.

3.4 Geometry on the steam side

The modeling of the tube surfaces as isothermal allowed us to decouple the search for geometry on the gas side (Section 3.3) from the search for geometry on the steam side. The two sides are not uncoupled. The location of the flow reversal [Eq. (3.20)] depends on the group N_{tu}, Eq. (3.21), which according to the analysis that led to Eq. (3.39) is

$$N_{tu,opt} = \frac{\pi C_a}{Pr_F^{1/2}}\left(\frac{\sigma^3}{12}\right)\left[\left(\frac{2}{C_D}\right)^{1/4}\frac{\pi C_a}{\sigma^3 Pr_F^{1/4}}\right]^{-7/9} Be^{1/12}\tilde{D}^{1/36}\tilde{L}^{5/36} \qquad (3.47)$$

$$\sim Be^{1/12}\tilde{D}^{1/36}\tilde{L}^{5/36}$$

Equation (3.20) is plotted in Fig. 3.3.

The numbers of tubes with downflow and upflow are

$$n_{down} = \frac{z_c}{L} n \qquad (3.48)$$

$$n_{up} = \left(1 - \frac{z_c}{L}\right) n \qquad (3.49)$$

According to Eqs. (3.46) and (3.47), these numbers are functions of $\tilde{D}$, $\tilde{L}$, $\tilde{H}$ and Be, however, the ratio n_{down}/n_{up} is comparable with 1 because z_c/L is order of 0.5, cf. Fig. 3.3.

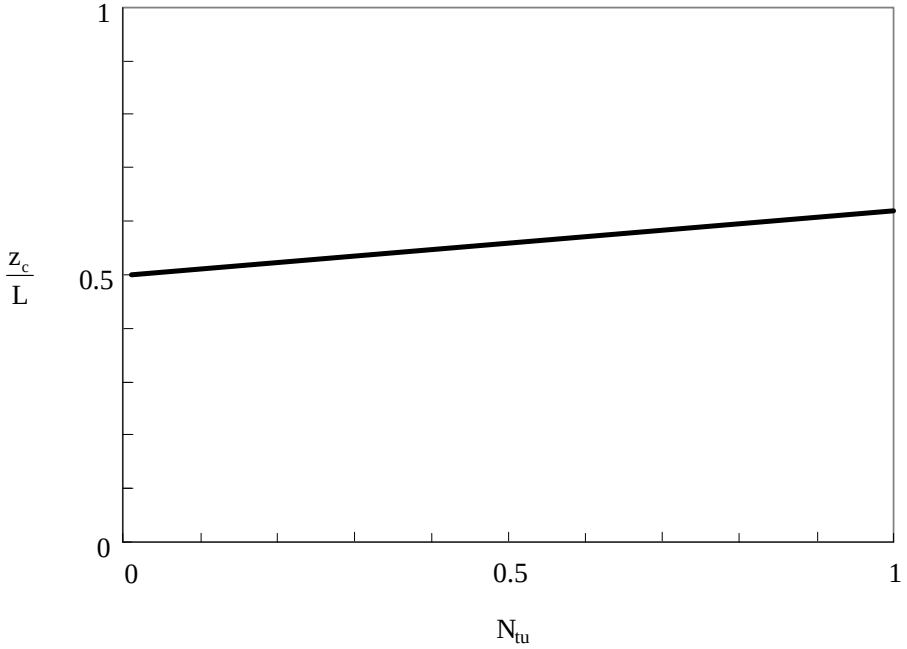

Figure 3.3: The longitudinal location of the flow reversal, for which N_{tu} is given by Eq. (3.47).

Note that because of the small exponents of Be, $\tilde{D}$, and $\tilde{L}$ in Eq. (3.47), the expected order of magnitude of N_{tu} is 1. Furthermore, because the total downward mass flow rate must equal the total upward mass flow rate, the scaling $n_{down} \sim n_{up}$ means that the mass flow rate in one tube ($\dot{m}_1$) has the same scale in both parts, downcomer and riser.

At this stage, we conclude that the constructal design of the gas side (Section 3.3) determines the flow reversal position (Fig. 3.3) and several new relations between the geometric features of the design, namely Eqs. (3.41)-(3.49).

3.5 Two-phase flow model

The scaling relations developed so far are based on two assumptions that greatly simplified the analysis. First, the assumption that all the tube surfaces are isothermal at T_B had the effect of decoupling the heat transfer analysis of the gas side from the analysis of the water side. The second assumption was the single-phase modeling of the friction in one vertical tube [Eq. (3.15)], which allowed us to develop analytically the variation of the one-tube flow rate with the longitudinal position z, cf. Section 3.2. In the following analysis we relax this second assumption and treat the flow as that of a liquid-vapor mixture [28].

Figure 3.4 shows the temperature distribution in the hot gas and the main features of water circulation. The n_{down} tubes represent the downcomer, and the n_{up} tubes represent the riser. The sum of n_{down} and n_{up} is the number of tubes in the assembly, n, cf. Eq. (3.46), which is obtained by constructal design of the continuous steam generator for the gas side.

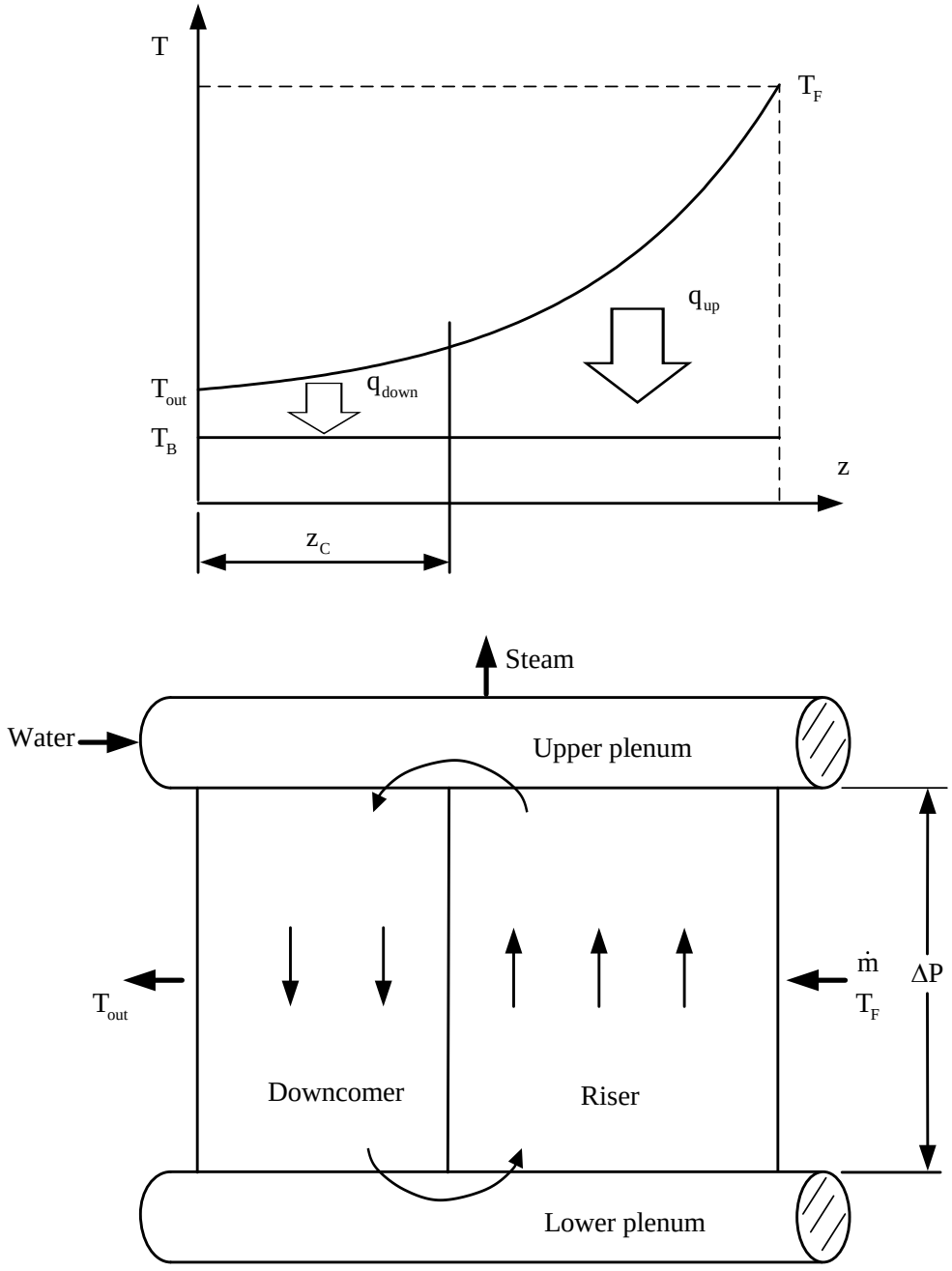

Figure 3.4: The natural circulation (self-pumping effect) in the continuous steam generator model.

The pressure drop in two-phase flow is function of pressure and quality. The pressure difference ΔP between two plenums is (cf. Fig. 3.4)

$$\Delta P = \Delta P_a + \Delta P_f + \Delta P_g \tag{3.50}$$

where ΔP_a and ΔP_f are the acceleration and friction pressure drops, and ΔP_g is the hydrostatic pressure difference for the two-phase flow [28]

$$\Delta P_a = v_f \left(\frac{\dot{m}_w}{A} \right)^2 r_2 \tag{3.51}$$

$$\Delta P_f = 4f \frac{H}{D} \frac{v_f}{2} \left(\frac{\dot{m}_w}{A} \right)^2 r_3 \tag{3.52}$$

$$\Delta P_g = \frac{gH}{v_f} r_4 \tag{3.53}$$

The pressure difference along each tube is the same as ΔP because the pressure in the plenums is uniform, and each tube is installed between the two plenums. For simplicity, we divide the tubes into two groups, downcomer and riser, in order to find the ratio of numbers of downcomer and riser tubes. Considering first the downward flow in the downcomer,

$$\Delta P_{down} = -v_f \left(\frac{\dot{m}_w}{A_1} \right)^2 r_{2,1,out} - 4f_1 \frac{H}{D} \frac{v_f}{2} \left(\frac{\dot{m}_w}{A_1} \right)^2 r_{3,1,out} + gH \frac{1}{v_f} r_{4,1,out} \tag{3.54}$$

where subscript 1 represents the downcomer,

$$A_1 = n_{down} \frac{\pi D^2}{4} \tag{3.55}$$

The quality values at the inlet and outlet of the riser are greater than zero due to the heat

transferred to the downcomer. The two-phase pressure drop is evaluated by subtracting the inlet pressure drop from the outlet pressure drop, which yields the pressure difference equation for the riser,

$$\Delta P_{up} = -v_f\left(\frac{\dot{m}_w}{A_2}\right)^2\left(r_{2,2,out} - r_{2,2,in}\right) - 4f_2\frac{H}{D}\frac{v_f}{2}\left(\frac{\dot{m}_w}{A_2}\right)^2\left(r_{3,2,out} - r_{3,2,in}\right) - gH\frac{1}{v_f}\left(r_{4,2,out} - r_{4,2,in}\right) \tag{3.56}$$

Here the subscript 2 represents the riser,

$$A_2 = n_{up}\frac{\pi D^2}{4} \tag{3.57}$$

Next, for the closed loop formed by the downcomer and the riser we write

$$\Delta P_{down} + \Delta P_{up} = 0 \tag{3.58}$$

Substituting Eqs. (3.54) and (3.57) into Eq. (3.58), and using $n_{down} = n - n_{up}$ and $r_{4,1,out} = r_{4,2,in}$, we obtain the global flow resistance equation for the two-phase flow system:

$$R = \frac{g\pi^2\rho_f^2 HD^4}{16\dot{m}_w^2}\left(2r_{4,1,out} - r_{4,2,out}\right) = \frac{r_{2,1,out}}{\left(n - n_{up}\right)^2} + \frac{2f_1 r_{3,1,out}H}{\left(n - n_{up}\right)^2 D} + \frac{\left(r_{2,2,out} - r_{2,2,in}\right)}{n_{up}^2} + \frac{2f_2\left(r_{3,2,out} - r_{3,2,in}\right)H}{n_{up}^2 D} \tag{3.59}$$

If the friction factors (f_1, f_2) are assumed to be independent of n_{up}, then the global flow resistance can be minimized analytically by solving $\partial R/\partial n_{up} = 0$, which yields

$$\left(\frac{n}{n_{up}}\right)_{opt} = 1 + \left\{\frac{r_{2,1,out} + 2f_1 r_{3,1,out} H/D}{\left[\left(r_{2,2,out} - r_{2,2,in}\right) + 2f_2\left(r_{3,2,out} - r_{3,2,in}\right)H/D\right]}\right\}^{1/3} \tag{3.60}$$

Consider two limiting conditions: $r_2 >> 2f\, r_3 H/D$ and $r_2 << 2f\, r_3 H/D$, which correspond to H ~ D and H >> D, respectively:

$$\left(\frac{n}{n_{up}}\right)_{opt,\, H \sim D} = 1 + \left(\frac{1}{r_{2,2,out}/r_{2,1,out} - 1}\right)^{1/3} \tag{3.61}$$

$$\left(\frac{n}{n_{up}}\right)_{opt,\, H >> D} = 1 + \left(\frac{1}{r_{3,2,out}/r_{3,1,out} - 1}\right)^{1/3} \tag{3.62}$$

In Eqs. (3.61) and (3.62) we used $(f_1/f_2)^{1/3} \sim 1$, $r_{2,2,in} = r_{2,1,out}$ and $r_{3,2,in} = r_{3,1,out}$. Equations (3.61) and (3.62) show that in taller continuous steam generators the number of riser tubes is determined by the friction effect, and in shorter continuous generators the number of riser tubes is determined by the acceleration effect. According to Ref. [28], c.f., Figs. 2.3 and 2.4, r_2 and r_3 are expressed as linear functions,

$$r_2 = a_a x \tag{3.63}$$

$$r_3 = a_f x + 1 \tag{3.64}$$

where slopes, a_a and a_f, depend on pressure and their values become larger when the pressure decreases.

Using Eq. (3.63) we determine $r_{2,2,out}$ and $r_{2,1,out}$, because the quality x is proportional to the rate of heat absorption:

$$r_{2,2,out} = a_a x_{2,out} \tag{3.65}$$

$$r_{2,1,out} = k_{down}\ a_a x_{2,out} \tag{3.66}$$

where k_{down} represents the heat absorption ratio of the downcomer and has the range $0 < k_{down} < 1$:

$$k_{down} = \frac{q_{down}}{q_{max}} = 1 - \frac{q_{up}}{q_{max}} = 1 - \frac{T_F - T(z_c / L)}{T_F - T_{out}} \tag{3.67}$$

Using Eqs. (3.5) we obtain k_{down}:

$$k_{down} = 1 - \frac{1 - e^{-N_{tu}(1 - z_c / L)}}{1 - e^{-N_{tu}}} \tag{3.68}$$

which is shown in Fig. 3.5.

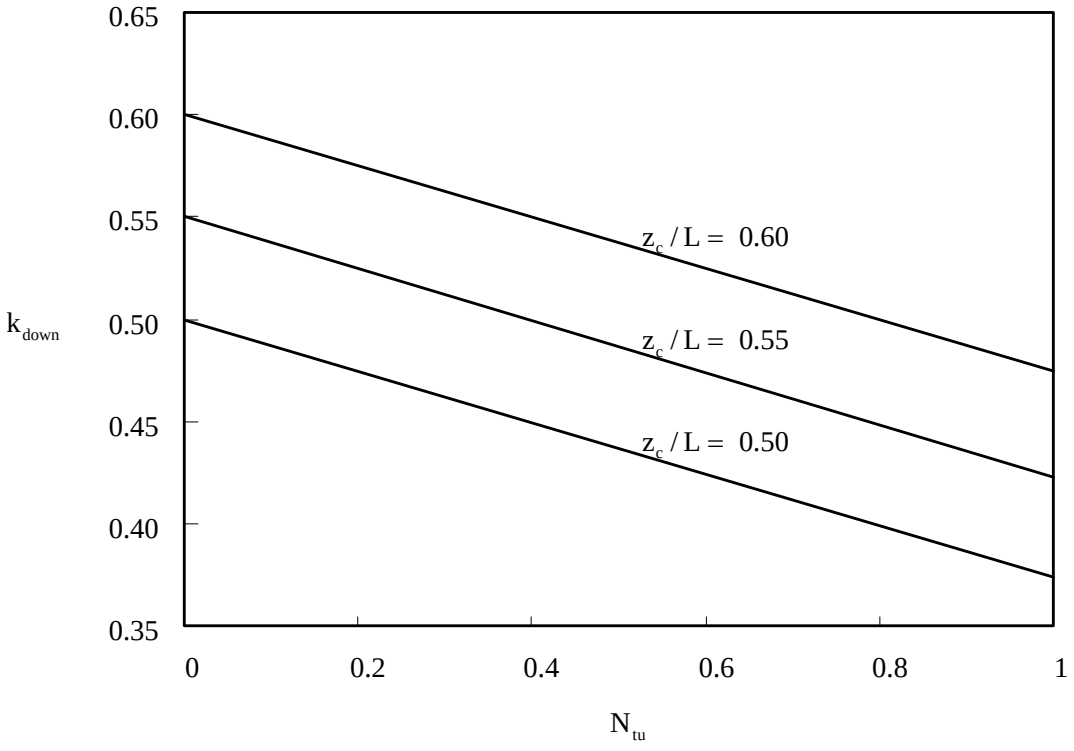

Figure 3.5: Heat absorption ratio of the downcomer.

Substituting Eqs. (3.65) and (3.66) into Eq. (3.61), which is the simpler form for shorter continuous steam generators (H ~ D), we obtain:

$$\left(\frac{n}{n_{up}}\right)_{opt,\ H\sim D} = 1 + \left(\frac{1}{1/k_{down} - 1}\right)^{1/3} \tag{3.69}$$

Equation (3.69) confirms that the location of the flow reversal in tubes depends on the number of heat transfer units N_{tu} (Section 3.2). If $N_{tu} > 1$, k_{down} is less than 0.5 as shown in Fig. 3.5; it leads to $n/n_{up} < 2$ and this means the number of the riser tubes is greater than the number of the downcomer tubes, i.e., $n_{up} > n_{down}$. If $N_{tu} << 1$, k_{down} is greater than 0.5; so, the number of the downcomer tubes is greater than the number of the riser tubes, i.e., $n_{up} < n_{down}$.

Using Eq. (3.64) we obtain $r_{3,2,out}$ and $r_{3,1,out}$

$$r_{3,2,out} = a_f x_{2,out} + 1 \tag{3.70}$$

$$r_{3,1,out} = k_{down}\ a_f x_{2,out} + 1 \tag{3.71}$$

Substituting Eqs. (3.70) and (3.71) into Eq. (3.62) yields the location of the flow reversal for taller continuous steam generators, H >> D case, in the function of a_f and k_{down}:

$$\left(\frac{n}{n_{up}}\right)_{opt,\ H>>D} = 1 + \left[\frac{1}{\left(a_f x_{2,out} + 1\right)/\left(k_{down}\ a_f x_{2,out} + 1\right) - 1}\right]^{1/3} \tag{3.72}$$

Equation (3.72) shows that the location of the flow reversal for tall continuous steam generators depends on pressure as well as the number of heat transfer units, because it is the function of a_f and k_{down} whereas it is only the function of the number of heat transfer

units for shorter continuous steam generators.

We can investigate Eq. (3.72) in three different cases. If $a_f x_{2,out} << 1$, and then $n/n_{up} \rightarrow \infty$. This means that the number of the downcomer tubes is significantly greater than the number of the riser tubes when pressure is high, i.e., a_f is very small. If $a_f x_{2,out} >> 1$, and then Eq. (3.72) becomes Eq. (3.69). This means that when pressure is low the number of the riser tubes can be greater or less than the number of the downcomer tubes, depending on the number of heat transfer units. If $a_f x_{2,out} \sim 1$, and then $2 < n/n_{up} < \infty$, because $1 < (a_f x_{2,out} + 1)/ (k_{down}\ a_f x_{2,out} + 1) < 2$. This implies that the number of the downcomer tubes is greater than the number of the riser tubes when the pressure is moderate. In sum, the location of the flow reversal can occur anywhere, depending on pressure and the number of heat transfer units for taller continuous steam generators.

Using these results, the design data for the location of the flow reversal, $z_c/L = 0.3$, can be reviewed; this value was determined by the measurement in the steam generator in operation and fixed for all design conditions [36]. The design data are: P ~ 3 MPa, H/D ~ 150, h ~ 10 kcal/hr m^2 ℃, A ~ 1000 m^2, $\dot{m}$ ~ 10^5 kg/hr and c_P ~ 0.1 kcal/kg ℃. We assume that the designed steam generator is tall and that the pressure is low. Substituting these data into Eq. (3.21) we obtain $N_{tu} \sim 1$. According to Fig. 3.5, k_{down} is less than 0.5; so, the number of the riser tubes should be greater than the number of the downcomer tubes, i.e., $z_c/L < 0.5$. This confirms that the design practice, $z_c/L = 0.3$, is reasonable. According to constructal theory, however, the fixed value of z_c/L should be avoided

because its value is the variable which can be determined by minimizing the global flow resistance as described in this section.

In conclusion, the minimization of the global flow resistance, cf., Eq. (3.59), yields the location of the flow reversal of continuous steam generators, which depends on pressure and the number of heat transfer units. We can infer that for high pressure the number of the downcomer tubes is greater than the number of the riser tubes, and that for low pressure the number of the riser tubes can be greater than the number of the downcomer tubes, depending on the number of heat transfer units.

3.6 Results and discussion

In this chapter we developed analytically the constructal design of continuous steam generators with large numbers of tubes so many that the temperature distribution in the horizontal direction may be modeled as continuous. This feature of the model and the approximation that the tubes are essentially isothermal at the boiling temperature, led to the analytical derivation of the location of flow reversal, i.e. the intermediate location that separates the down flowing steam tubes (the downcomer) from the upflowing tubes (the riser). The flow reversal location depends on pressure and the number of heat transfer units.

On the gas side of the crossflow heat exchanger, we used the method of intersecting the asymptotes and found that the spacing between tubes can be selected such that the global heat transfer density is maximal. The optimal spacing depends on three

dimensionless groups accounting for the imposed pressure difference, the tube diameter, and the horizontal flow length, Eq. (3.41). Corresponding scaling relations were determined for the total number of steam tubes and the maximal heat transfer density of the heat exchanger.

Constructal theory explains the design practice of continuous steam generator; most of continuous steam generators are designed for the low operation pressure. We see that the global flow resistance, Eq. (3.59), is the function of the gravitational friction factor difference ($2r_{4,1,out} - r_{4,2,out}$). According to Ref. [28], c.f., Fig. 2.2, r_4 decreases linearly at the high pressure; furthermore, the slope of r_4 at the high pressure becomes small. This implies that the global flow resistance becomes smaller at the high pressure. On contrary, at the low pressure ($2r_{4,1,out} - r_{4,2,out}$) has much larger value than the high pressure because r_4 decreases exponentially. Therefore continuous steam generators at the low pressure might operate more stably against various operation conditions such as startups, shutdowns and sudden load changes. This is the reason why *low pressure* continuous steam generators have been preferred over 100 years [21, 22].

This analysis and its results are useful with regard to scaling up and scaling down the designs of continuous steam generators. For example, the analysis showed that the total heat transfer rate increases in proportion with the length scale of the entire heat exchanger, Eq. (3.45). A consequence of this is the fact that the heat transfer density decreases as the length scale increases.

4. Distribution of Size in Steam Turbine Power Plants

Like all technologies, power plants are evolving. They are becoming more efficient and larger (Fig. 4.1). There is very clear relationship between thermodynamic performance and "size", which in Fig. 4.1 is represented by the net output of the plant; larger plants operate closer to the Carnot limit than smaller plants, Fig 4.2. This size effect is present in the performance of other energy conversion systems [37, 38], for example in heat exchanger design [22], automotive design [39], and refrigeration and liquefaction plants [40, 41]. It is explained by the relationship between the resistance encountered by a

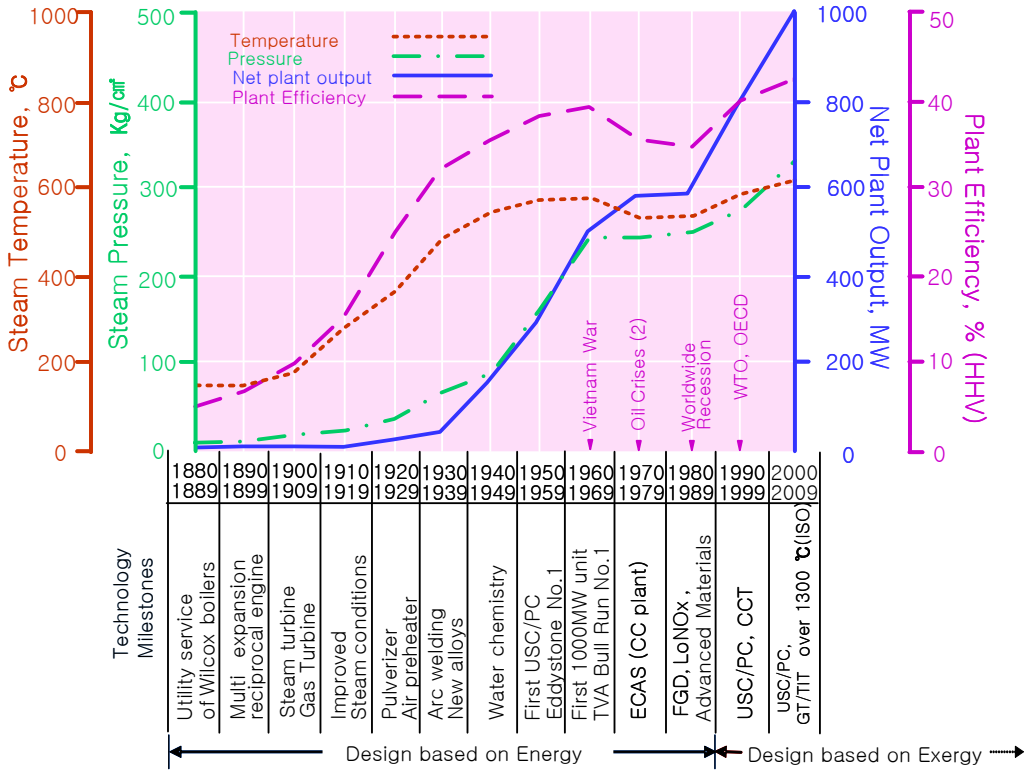

Figure 4.1: The evolution of power plant design in the 20th century.

flow (fluid, heat) and the size of the cross-section (duct, surface) pierced by the flow. Larger cross-sections offer less resistance. This holds for the cross-sections of pipes with fluid flow, and for the heat transfer areas of heat exchangers. The thermodynamic imperfection of a flow system is intimately tied to the size of its hardware [42].

Power plants are also evolving internally. Their structure has been changing in time. The emergence of new organs (superheater, regenerator, feedwater heater) is aligned very clearly with time and the stepwise increase in thermodynamic performance. This aspect of the evolution of power plant technology is one of the examples of how constructal theory unites engineering with the other flow designs of nature [40].

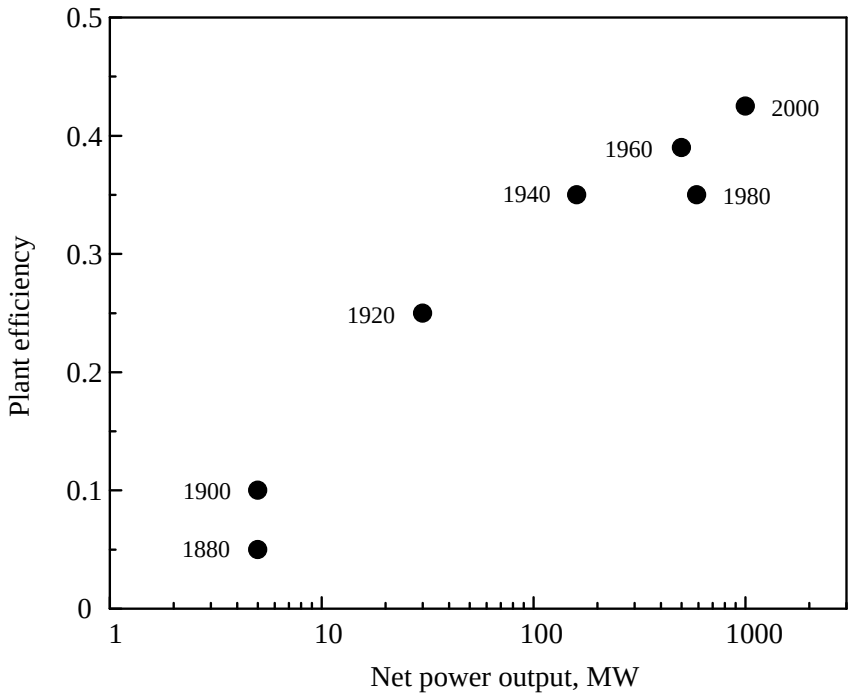

Figure 4.2: The relationship between plant efficiency and power output (from Fig. 4.1).

We focus on another aspect of power plant evolution, which has not been addressed in a predictive sense before. In late 1800s, the design of steam power plants was based on a single turbine. Contemporary power plants have turbine "groups" or "trains", consisting of a high pressure turbine (HP) followed by one or more intermediate pressure (IP) and low pressure (LP) turbines. Why are these changes happening? Why is not the single-turbine design surviving? What is the best way to divide one turbine into a train of smaller turbine?

The answer comes from the relation between the imperfection of an organ and the size of the organ. We see that this holds for the entire power plant (Fig. 4.2) and for a single turbine (Fig. 4.3). But, if larger turbines are more efficient, why not use a single large turbine as opposed to a group of smaller turbines?

In this chapter we answer these questions by adopting the constructal design proposal to view the whole installation is a *distributed energy system* [2]. The installation has a total size (e.g. total mass for all the turbines), and must mesh with the rest of the power plant, between clearly defined pressures (P_H, P_L), and at temperatures no greater than a specified level (T_H), cf. Fig. 4.4. Usually, the inlet steam temperature (T_2) of LP turbine can be higher than the inlet steam temperature (T_H) of HP turbine because the reheater is installed in a lower gas temperature region in the boiler and the allowable temperature of the tube material is fixed. However, we assume that T_2 is equal to T_H to simplify the analysis. What the installation does not have is configuration.

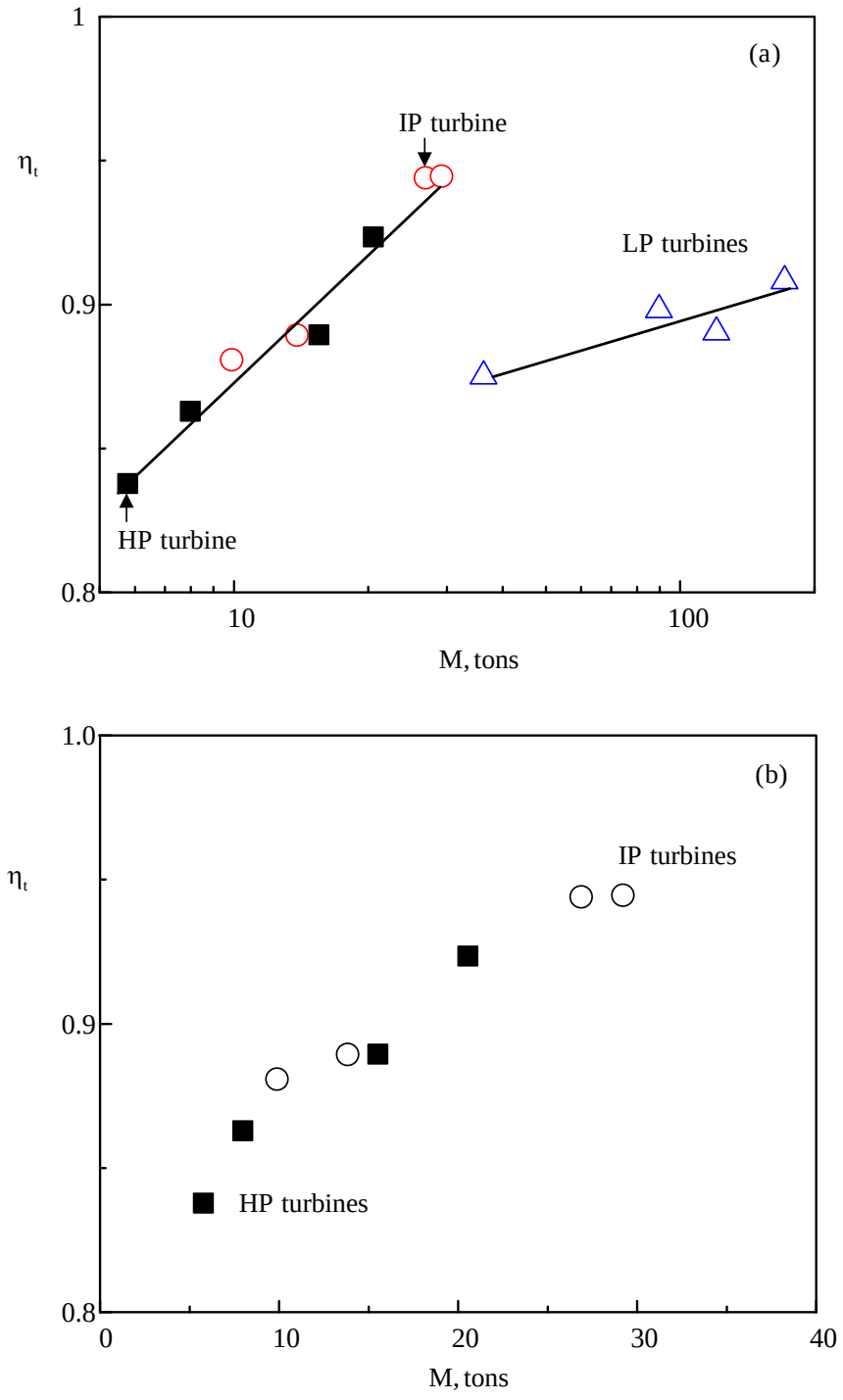

Figure 4.3: The relationship between turbine isentropic efficiency and size.

We give ourselves the freedom to image that we can distribute the available mass over the pressure interval occupied by the installation. Our objective is to distribute the mass inventory in such a manner that the total power produced by the installation is greater and greater. In this direction of design evolution, the installation obtains its configuration – more mass in turbines at some pressures, as opposed to less mass in the remaining turbines.

4.1 Two turbines in series

Consider the train of two turbines shown in Fig. 4.4. The overall pressure ratio is fixed, P_H/P_L. The steam enters the two turbines at the highest allowable temperature level, $T_1 = T_2 = T_H$. The power outputs from the two turbines are (cf. Ref. [40]):

$$W_1 = \dot{m} c_p \left(T_1 - T_{1'} \right) = \dot{m} c_p T_H \eta_1 \left[1 - \left(\frac{P_i}{P_H} \right)^{R/c_p} \right] \tag{4.1}$$

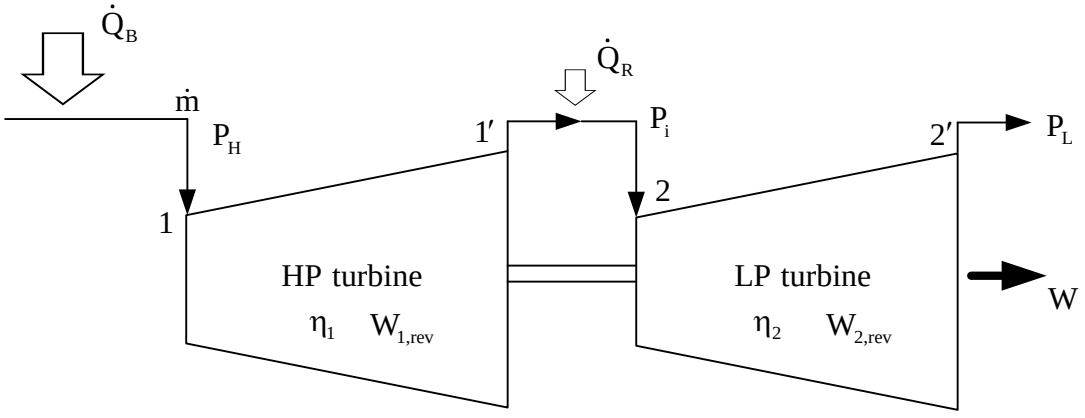

Figure 4.4: Train of two turbines, high pressure and low pressure.

$$W_2 = \dot{m} c_P \left(T_2 - T_{2'} \right) = \dot{m} c_P T_H \eta_2 \left[1 - \left(\frac{P_L}{P_i} \right)^{R/c_P} \right] \tag{4.2}$$

The heat transfer rate to the reheater is

$$Q_R = \dot{m} c_P \left(T_2 - T_{1'} \right) = W_1 \tag{4.3}$$

The overall efficiency of the power plant is

$$\eta = \frac{W_1 + W_2}{Q_B + Q_R} = \frac{1}{Q_B} \frac{W_1 + W_2}{1 + Q_R / Q_B} \tag{4.4}$$

where Q_B is the heat transfer rate administrated to the $\dot{m}$ stream in the boiler, before state 1. For simplicity, we recognize that in modern power plants the ratio Q_R/Q_B is of order 1/10, and this allows us to approximate Eq. (4.4) as

$$\eta Q_B \cong \left(W_1 + W_2 \right) \left(1 - \frac{W_1}{Q_B} \right) \tag{4.5}$$

where Q_B is fixed because state 1 is fixed (P_H, T_H). Equation (4.5) can be written further as

$$\eta \frac{Q_B}{\dot{m} c_P T_H} = \left\{ \eta_1 \left[1 - \left(\frac{P_i}{P_H} \right)^{R/c_P} \right] + \eta_2 \left[1 - \left(\frac{P_L}{P_i} \right)^{R/c_P} \right] \right\} \times \left\{ 1 - \frac{\dot{m} c_P T_H}{Q_B} \eta_1 \left[1 - \left(\frac{P_i}{P_H} \right)^{R/c_P} \right] \right\} \tag{4.6}$$

The expression shown above can be maximized with respect to P_i, by solving $\partial\eta/\partial P_i = 0$,

and in the limit $\dot{m}c_P T_H / Q_B << 1$ (which is consistent with $Q_R << Q_B$) the optimal intermediate pressure is

$$P_i \cong \left(P_H P_L\right)^{1/2} \left(\frac{\eta_2}{\eta_1}\right)^{c_P/2R} \times \left\{1 + \frac{\dot{m}c_P T_H}{Q_B}\left[\frac{1}{2}\left(1 + \frac{\eta_2}{\eta_1}\right) - \left(\frac{\eta_2}{\eta_1}\right)^{1/2}\left(\frac{P_L}{P_H}\right)^{R/2c_P}\right]\right\} \tag{4.7}$$

Simpler forms in the limit represented by Eq. (4.7) are available for $\eta_2 / \eta_1 \cong 1$ (note: $\eta_{1,2} < 1$),

$$P_i \cong \left(P_H P_L\right)^{1/2} \left\{1 + \frac{\dot{m}c_P T_H}{Q_B}\left[1 - \left(\frac{P_L}{P_H}\right)^{R/2c_P}\right]\right\} \tag{4.8}$$

which in the limit $\dot{m}c_P T_H / Q_B = 0$ reduces to

$$P_i = \left(P_H P_L\right)^{1/2} \tag{4.9}$$

The analysis that follows is based on the simpler version, Eq. (4.9), in order to make the demonstration entirely analytically. In reality, the limit $\dot{m}c_P T_H / Q_B = 0$ is not reached. For example, the boiler of a 500 MW power plant receives $\dot{m} = 473$ kg/s and $Q_B = 10^6$ kW, while $T_H = 813$ K [43]. In this case, the dimensionless group $\dot{m}c_P T_H / Q_B$ is equal to 1.26. However, its effect on Eq. (4.8) is weak because the quantity shown between { } is essentially constant and of order 1.

The isentropic efficiencies increase monotonically with the sizes of two turbines

(M_1, M_2), cf. Fig. 4.3. The $\eta(M)$ curves must be concave because they both approach $\eta = 1$ in the limit $M \to \infty$. It is reasonable to assume that near $\eta \leq 1$ the $\eta(M)$ data for turbine designs are curve fitted by

$$\eta_1 = 1 - a_1 e^{-b_1 M_1} \tag{4.10}$$

$$\eta_2 = 1 - a_2 e^{-b_2 M_2} \tag{4.11}$$

where $(a, b)_{1,2}$ are four empirical constants that depend on the pressure level of the turbine. The total power produced by the two turbines is $W = \eta_1 W_{1,rev} + \eta_2 W_{2,rev}$, where the functions $\eta_1(M_1)$ and $\eta_2(M_2)$ are known. The total mass of the ensemble is fixed,

$$M = M_1 + M_2 \tag{4.12}$$

There is one degree of freedom in the making of Fig. 4.4, namely the dividing of M into M_1 and M_2. The optimal way to divide M is determined using the method of Lagrange multipliers. We form the aggregate function

$$\Phi = W + \lambda M \tag{4.13}$$

for which W and M are the expressions (4.1, 4.2) and (4.12). We solve the system $\partial\Phi / \partial M_1 = 0$ and $\partial\Phi / \partial M_2 = 0$, eliminate the multiplier λ, and obtain

$$b_1 M_1 - b_2 M_2 = \ln\left(\frac{a_1 b_1 W_{1,rev}}{a_2 b_2 W_{2,rev}} \right) \tag{4.14}$$

Equations (4.14) and (4.12) pinpoint the mass allocation fractions M_1/M and M_2/M. The first and most important conclusion is that there must be a *balance* between M_1 and M_2.

For example, if we use the HP and IP data of Fig. 4.3 for η_1 of Eq. (4.10), we obtain approximately $a_1 \cong 0.2$ and $b_1 \cong 4.6\times10^{-5}\ \text{kg}^{-1}$. If we use the LP data of Fig. 4.3 in conjunction with Eq. (4.11), we estimate that $a_2 \cong 0.13$ and $b_2 \cong 2.1\times10^{-5}\ \text{kg}^{-1}$. If, in addition, Eq. (4.9) holds, then $W_{1,rev} = W_{2,rev}$ and this means that on the right hand side of Eq. (4.14) we have $a_1b_1W_{1,rev}/(a_2b_2W_{2,rev}) \cong 34$, which considerably greater than 1. In conclusion, Eq. (4.14) states that b_1M_1 is greater than b_2M_2, namely $b_1M_1 \cong b_2M_2 + 3.5$.

Combining Eqs. (4.12) and (4.14) yields the optimal mass distribution equations for high pressure and low pressure turbines

$$M_1 = 0.044\,M + 7.3\times10^4\ \text{kg} \tag{4.15}$$

$$M_2 = 0.956\,M - 7.3\times10^4\ \text{kg} \tag{4.16}$$

M_1 equals M_2 when $M = 1.6\times10^5$ kg. In conclusion, there is an optimal way *to distribute mass* along the train of turbines. According to Eqs. (4.15) and (4.16), the total mass is allocated in a balanced way; with more mass at the high pressure end when total mass M is small, and with more mass at the low pressure end when the total mass is large. What we showed here for a group of two turbines also holds for groups of three or more.

The penalty associated with not using a train of turbines can be calculated with reference to Fig. 4.4. We form the ratio $W(M_2=0)/W_{max}$, where W_{max} is the W maximum that corresponds to the constructal design, Eq. (4.9). The ratio is

$$\frac{W(M_2 = 0)}{W_{max}} = \frac{1}{2}\left[1 + \left(\frac{P_L}{P_H}\right)^{R/2c_p}\right] < 1 \qquad (4.17)$$

This ratio is always smaller than 1. In conclusion, the penalty is more significant when the overall pressure ratio is greater.

4.2 Multiple turbines

Consider the limit where the number of turbines is extremely large (i = 1, 2, …, N) and their individual sizes are small, Fig. 4.5. Each turbine and subsequent reheater can be modeled as an isothermal expander receiving the heat transfer rate Q_i and the steam $\dot{m}(T_H,\ P_i + \Delta P_i)$, and delivering the power W_i and the steam $\dot{m}(T_H,\ P_i)$.

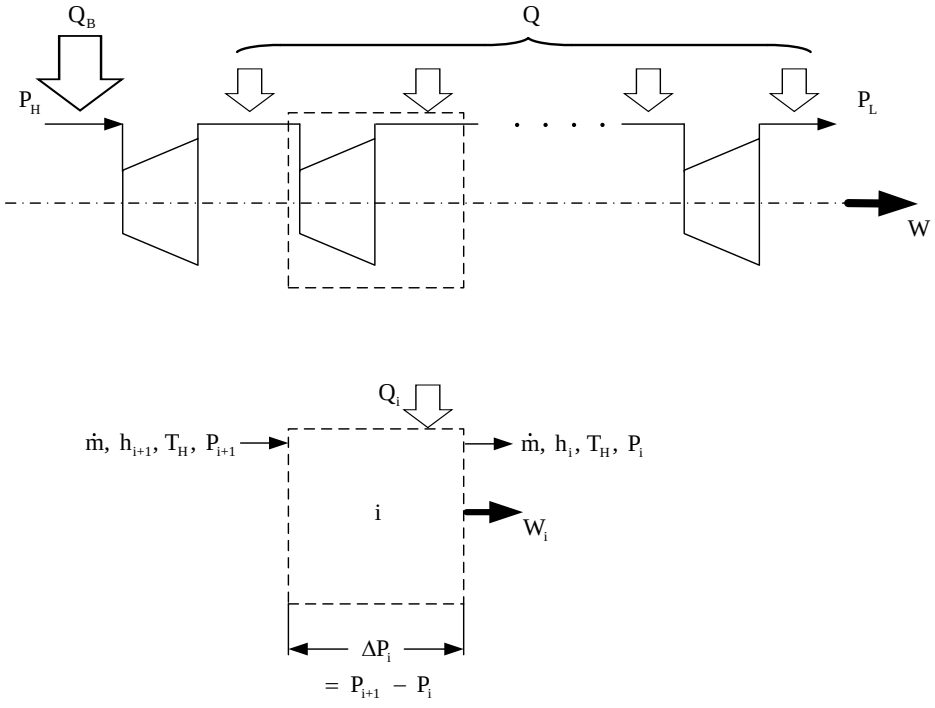

Figure 4.5: Train of N turbines.

With reference to the elemental system (i) shown in Fig. 4.5, the first law requires

$$W_i = Q_i + \dot{m}\left(h_{i+1} - h_i\right) \tag{4.18}$$

Because the steam is modeled as an ideal gas, the enthalpy of the inflow is the same as the enthalpy of the outflow, and the first law reduces to

$$W_i = Q_i \tag{4.19}$$

If the isothermal expander (i) operates reversibly, then

$$Q_{i,rev} = \dot{m}T_H\left(s_{out} - s_{in}\right)_i = \dot{m}T_H R\frac{\Delta P_i}{P_i} \tag{4.20}$$

and $W_{i,rev} = Q_{i,rev}$. The actual system operates irreversibly with the efficiency

$$\eta_i = \frac{W_i}{W_{i,rev}} < 1 \tag{4.21}$$

and its power output is

$$W_i = \dot{m}T_H R\eta_i\frac{\Delta P_i}{P_i} \tag{4.22}$$

where $\Delta P_i = P_{i+1} - P_i$. Of interest is the total power delivery

$$W_T = \dot{m}T_H R\sum_{i=1}^{N}\eta_i\frac{P_{i+1} - P_i}{P_i} \tag{4.23}$$

which in combination with the boiler heat input (Q_B, fixed) and the total heat input to the isothermal train ($Q = W$), yields the efficiency ratio

$$\eta = \frac{W}{Q_B + W} \tag{4.24}$$

In order to maximize η we must maximize total power W_T given by Eq. (4.23). Attractive are larges value of $(\Delta P/P)_i$ and η_i, in each stage of isothermal expansion. The data of Fig. 4.3 suggest that, in general, η_i depends on both M_i and P_i, such that

$$\frac{\partial \eta_i}{\partial M_i} > 0 \quad \text{and} \quad \frac{\partial \eta_i}{\partial P_i} > 0 \tag{4.25}$$

The masses of the N turbines are constrained by the total mass of the turbine train, which is fixed:

$$M_T = \sum_{i=1}^{N} M_i \tag{4.26}$$

Another constraint is the ΔP_i's must all up to the overall pressure difference, $\Delta P_T = P_H - P_L$:

$$\Delta P_T = \sum_{i=1}^{N} \left(P_{i+1} - P_i \right) \tag{4.27}$$

In summary, we must maximize the sum (4.23) subject to the constraints (4.26) and (4.27). According to Lagrange's method of undetermined coefficients, this problem is equivalent to seeking the extremum of the function

$$F = \sum_{i=1}^{N} \left[\eta_i \left(\frac{P_{i+1}}{P_i} - 1 \right) + \lambda M_i + \mu \left(P_{i+1} - P_i \right) \right] \tag{4.28}$$

where $\eta_i = \eta_i(M_i, P_i)$, and λ and μ are two Lagrange multipliers. The function F is a linear combination of the sums (4.23), (4.26) and (4.27). It depends on 2N + 2 variables, namely λ, μ, M_1, …, M_N and P_1, …, P_N. Its extremum is found by solving the system of 2N

equations

$$\frac{\partial F}{\partial M_i} = \frac{\partial \eta_i}{\partial M_i}\left(\frac{P_{i+1}}{P_i} - 1\right) + \lambda = 0, \quad (i = 1, 2, \ldots, N) \tag{4.29}$$

$$\frac{\partial F}{\partial P_i} = \frac{\partial \eta_i}{\partial P_i}\left(\frac{P_{i+1}}{P_i} - 1\right) - \eta_i \frac{P_{i+1}}{P_i^2} + \mu = 0, \quad (i = 1, 2, \ldots, N) \tag{4.30}$$

This system establishes the N masses (M_i) and the N intermediate pressures (P_i) as functions of the undetermined coefficients λ and μ. In principle, these coefficients can be determined by substituting the solutions for $M_i(\lambda, \mu)$ and $P_i(\lambda, \mu)$ into the constraints (4.26) and (4.27).

Here we make analytical progress on a simpler path by linearizing the function $\eta_i(M_i)$ in the vicinity of the design range in which all the turbines are expected to operate (namely, near $\eta_t \sim 1$ in Fig. 4.3). We write that for all N turbines the efficiency-mass relation is unique,

$$\eta_i \cong a + bM_i + cP_i \tag{4.31}$$

where (a, b, c) are constants. The first result of the linearization is that the N equations (4.29) reduce to

$$\frac{P_{i+1}}{P_i} = \text{constant} \tag{4.32}$$

In view of Eq. (4.27), we conclude that the total pressure interval ΔP_T is divided into N pressure intervals such that

$$\frac{P_{i+1}}{P_i} = \left(\frac{P_H}{P_L}\right)^{1/N} \tag{4.33}$$

or

$$\frac{\Delta P_i}{P_i} = \left(\frac{P_H}{P_L}\right)^{1/N} - 1 \tag{4.34}$$

This is in agreement with what we found earlier in Eq. (4.9).

The distribution of M_T among the N turbines follows from Eqs. (4.30), in which we substitute Eqs. (4.31) and (4.32). The result is

$$\frac{\eta_i}{P_i} = \left(\frac{P_L}{P_H}\right)^{1/N} \left\{\mu + c\left[\left(\frac{P_H}{P_L}\right)^{1/N} - 1\right]\right\}, \quad \text{constant} \tag{4.35}$$

This shows that in the (M_i, P_i) range where Eq. (4.31) is valid, Eq. (4.35) becomes

$$a + bM_i + cP_i = P_i \times \text{constant} \tag{4.36}$$

If the effect of P_i on η_i is negligible, as in the case of the HP and IP data of Fig. 4.3, then Eq. (4.36) reduces to

$$a + bM_i \cong P_i \times \text{constant} \tag{4.37}$$

The mass of the individual turbine should increase linearly with the pressure level of that turbine.

In particular, if the linear approximation (4.31) reveals that $a/b << M_i$, as in the calculations shown under Eq. (4.14), then Eq. (4.37) states that the M_i's must be distributed in proportion with the P_i's, and, in view of Eq. (4.34), in proportion with the

ΔP_i's:

$$M_i \sim P_i \sim \Delta P_i \tag{4.38}$$

Equation (4.38) indicates that more mass should be placed in the expanders at higher pressures.

4.3 Results and discussion

These is a considerable volume of work on turbine design, where the size is selected from other considerations such as the distribution of maximal stresses due to centrifugal forces, and the flaring out of the flow passages to accommodate the expansion of the steam along the turbine train [44]. The work reported in the present chapter suggests that the design of future concepts of turbine train configuration must combine the traditional considerations [45, 46] with size allocation principle illustrated in this chapter.

This chapter also highlights the need for more extensive and more exact information on how the size of each turbine affects its thermodynamic performance. The data that we used (Fig. 4.3) are few and provide a narrow view of the size effect that is needed for future design. These data also require an understanding of how the multiple turbines are arranged in the power plant.

As the power generation capacity of the plant increases, the boiler and the turbine also increase in size. It is easer to increase the size of the boiler than the size of the

turbine. Today, in a 1000 MW power plant there is still a single boiler, while the number of turbines is five or six. Each pressure stage employs one or several (two or three) turbines in parallel. For example, in power plants with more than 500 MW capacity, the LP stage consistently employs two or more turbines.

Several physical limitations require the use of multiple turbines in parallel at a single pressure stage. A major limitation posed by centrifugal stresses is the length of the last blade. The current maximum length is approximately 1.3 m. The data of Fig. 4.3 come from a current design for a 1000 MW power plant with a low-pressure stage consisting of four turbines in parallel, each turbine with last blades 1.14 m long. The ordinate of Fig. 4.3 indicates the efficiency of the single LP turbine, while the abscissa represents the total mass employed for each pressure stage. If the mass of the LP turbines is divided by 4, then the LP data of Fig. 4.3 move closer to the HP and IP data.

Note also that the efficiency of one turbine is affected by the operation of the turbine upstream of it. The irreversibility of a turbine is due to six losses: deviation from the ideal velocity ratio, rotational loss, diaphragm-packing leakage loss, nozzle end loss, moisture and supersaturating loss and exhaust loss [44]. The last two losses are present only in the LP turbines, not upstream, therefore the efficiency of the single LP turbine should be lower than the efficiency of HP and IP turbines, cf. Fig. 4.3. Furthermore, because the HP turbine is installed at the head of the train, its efficiency should be lower than the IP turbine efficiency because of entrance losses due to the configuration of the

steam passage. This too is confirmed by the data of Fig. 4.3.

The optimal intermediate pressure Eqs. (4.7)-(4.9) may not be attainable in a design with two turbines model because of the properties of water. For example, the intermediate pressure in a 500 MW power plant is approximately 4 MPa, while the intermediate pressure based on Eq. (4.9) is 0.35 MPa. The discrepancy between the intermediate pressures is due to the ideal gas model used for steam. If we model as isentropic the expansion through the high pressure turbine, because of the saturated steam curve of water the attainable intermediate pressure is 3.15 MPa. The expansion cannot proceed beyond 3.15 MPa because of engineering limitations such as water droplet impingement on the blades. This limitation impacts on the mass distribution of turbines for two turbines model. When the number of pressure stages increase to three or more, the expansion limitation due to steam properties diminishes in importance.

The total turbine mass must be divided in a certain way when two or more turbines are used in series. The allocating of mass is synonymous with the discovery of the configuration of the turbine train. Important is that in this article the distribution of "size" along the turbine train came from the pursuit of global thermodynamic performance. The allocation of mass is driven by the size effect on turbine efficiency: larger turbines operate closer to the reversible limit (e.g. Fig. 4.3).

Future extensions of this work should take into account the physical limitations that make necessary the use of several turbines in parallel at a pressure stage. Such work

could address the distribution of turbine mass per pressure stage, instead of per turbine. This work would be assisted further by the availability of more extensive data of the type sampled in Fig. 4.3. To that end, it would be useful to construct models that account for the trend exhibited by the data. In other words, the analytical form of $\eta(M, P)$, which was approximated here in Eqs. (4.10) and (4.31), should be derived from a model that accounts for irreversibility and finite size.

5. Constructal Configuration for Natural and Forced Convection in Cross-flow

Convection plays a vital role in power and its pieces of equipment. Even though half of total heat transfer in the power plant is done by the convection, most of the heat transfer surface is occupied by the convective heat transfer because the intensity of the heat flux by radiation in the furnace is significantly greater than the convection [21, 22]. Therefore, the optimal sizing and shaping of components for convection is a major requirement in power plant design.

According to traditional practice, most of the data and equations used in the design and engineering of components of the power plant refer to heat transfer configurations that are documented in handbooks and in a very active research literature [21, 22, 47-78]. Even though the objective in engineering design is to create the configuration of the system, the effect of the flow configuration on the performance of the convective heat transfer components is largely overlooked. In this chapter we show how the configuration dictates the global performance of a crossflow heat exchanger with forced convection on the outside and natural convection on the inside. We show that it is possible to “morph” the architecture of the device such that its global heat transfer rate, or volumetric heat transfer density is maximized. In this direction of design evolution, the flow architecture tends to become simpler.

5.1 Numerical model

Figure 5.1 shows a cross-flow configuration with two vertical tubes and two plenums. A cold single-phase fluid fills the tubes and the plenums. A hot stream of the same fluid flows horizontally around and between the tubes. Heat flows from the hot stream to the cold stream inside the tubes. The leading tube is heated more intensively than the trailing tube, and the difference between the two heating rates causes a density difference between the fluid densities in the two tubes. Buoyancy drives a circulation loop,

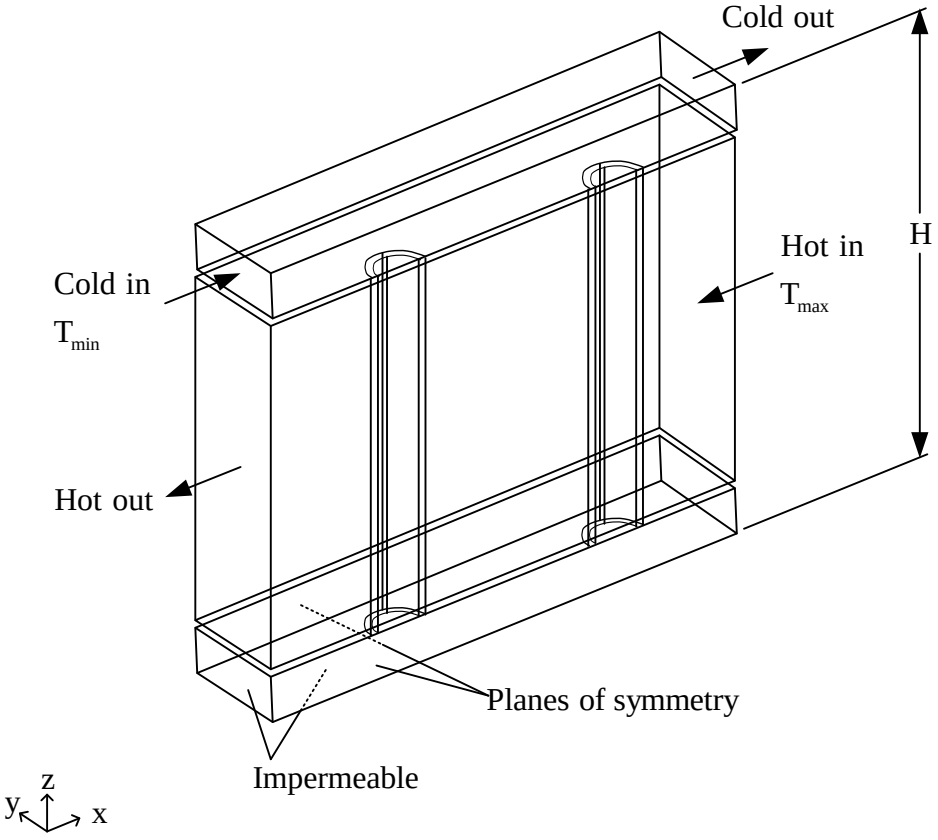

Figure 5.1: Cross-flow configuration.

with the flow upward through the leading tube and downward through the trailing tube. The circulation is completed by horizontal flows in the two plenums. The heat transfer to the two tubes is convected away by a slow stream of cold fluid, which enters the upper plenum from the left (with the average speed uc,in) and exits to the right (Fig. 5.1).

The driving force for the natural circulation is proportional to the temperature difference between the two vertical fluid columns inside the tubes. We adopt the Boussinesq approximation that the fluid density decreases linearly with the temperature,

$$\rho = \rho_0 \left[1 - \beta \left(T - T_0 \right) \right] \tag{5.1}$$

and that $\beta \left(T - T_0 \right) << 1$. The subscript 0 indicates a reference condition. Equation (5.1) is used in the modeling of the flow inside the tubes and the plenums, and it couples the momentum and energy equations in that flow volume. The dimensionless governing equations for steady incompressible flow are written in terms of the dimensionless variables

$$\left(\tilde{x}, \tilde{y}, \tilde{z} \right) = \left(x, y, z \right) / H \tag{5.2}$$

$$\left(\tilde{u}, \tilde{v}, \tilde{w} \right) = \left(u, v, w \right) / U_s \tag{5.3}$$

$$\tilde{P} = P / \rho U_s^2 \tag{5.4}$$

$$\tilde{T} = \left(T - T_{min} \right) / \Delta T \tag{5.5}$$

where

$$\Delta T = T_{max} - T_{min} \tag{5.6}$$

H is the height of the cross-flow configuration, T_{max} and T_{min} are maximum and minimum inlet temperatures, which are fixed, and U_s represents the velocity scale, which is obtained by a scale analysis (e.g. Ref. [33])

$$U_s = \frac{\nu}{H} \tag{5.7}$$

The resulting dimensionless equations for mass, momentum and energy conservation in the internal fluid space with laminar flow are

$$\frac{\partial \tilde{u}}{\partial \tilde{x}} + \frac{\partial \tilde{v}}{\partial \tilde{y}} + \frac{\partial \tilde{w}}{\partial \tilde{z}} = 0 \tag{5.8}$$

$$\tilde{u}\frac{\partial \tilde{u}}{\partial \tilde{x}} + \tilde{v}\frac{\partial \tilde{u}}{\partial \tilde{y}} + \tilde{w}\frac{\partial \tilde{u}}{\partial \tilde{z}} = -\frac{\partial \tilde{P}}{\partial \tilde{x}} + \tilde{\nabla}^2\tilde{u} \tag{5.9}$$

$$\tilde{u}\frac{\partial \tilde{v}}{\partial \tilde{x}} + \tilde{v}\frac{\partial \tilde{v}}{\partial \tilde{y}} + \tilde{w}\frac{\partial \tilde{v}}{\partial \tilde{z}} = -\frac{\partial \tilde{P}}{\partial \tilde{y}} + \tilde{\nabla}^2\tilde{v} \tag{5.10}$$

$$\tilde{u}\frac{\partial \tilde{w}}{\partial \tilde{x}} + \tilde{v}\frac{\partial \tilde{w}}{\partial \tilde{y}} + \tilde{w}\frac{\partial \tilde{w}}{\partial \tilde{z}} = -\frac{\partial \tilde{P}}{\partial \tilde{z}} + \tilde{\nabla}^2\tilde{w} + Gr\,\tilde{T} \tag{5.11}$$

$$Pr\left(\tilde{u}\frac{\partial \tilde{T}}{\partial \tilde{x}} + \tilde{v}\frac{\partial \tilde{T}}{\partial \tilde{y}} + \tilde{w}\frac{\partial \tilde{T}}{\partial \tilde{z}}\right) = \tilde{\nabla}^2\tilde{T} \tag{5.12}$$

where $\tilde{\nabla}^2 = \partial^2/\partial\tilde{x}^2 + \partial^2/\partial\tilde{y}^2 + \partial^2/\partial\tilde{z}^2$ and

$$Gr = \frac{g\beta\Delta T H^3}{\nu^2} \tag{5.13}$$

The corresponding equations for laminar flow in the space outside the tubes, under the assumption that the external fluid is the same as the internal fluid, are the same as the internal fluid space except the w-momentum equation, which is

$$\tilde{u}\frac{\partial \tilde{w}}{\partial \tilde{x}} + \tilde{v}\frac{\partial \tilde{w}}{\partial \tilde{y}} + \tilde{w}\frac{\partial \tilde{w}}{\partial \tilde{z}} = -\frac{\partial \tilde{P}}{\partial \tilde{z}} + \tilde{\nabla}^2\tilde{w} \tag{5.14}$$

The energy equation for the solid tube walls is

$$\tilde{\nabla}^2\tilde{T} = 0 \tag{5.15}$$

The thermal boundary conditions are $\tilde{T} = 0$ at the inlet to the internal flow plenum ($T = T_{min}$, Fig. 5.1), and $\tilde{T} = 1$ at the inlet to the external flow space ($T = T_{max}$, Fig. 5.1). The side walls are thermally and hydrodynamically planes of symmetry. The other walls of the plenums are impermeable and adiabatic. The Reynolds numbers at the inlet of the upper plenum and the external flow space are

$$Re_{D_h,c} = \frac{u_{c,in}D_h}{\nu} = \tilde{u}_{c,in}\tilde{D}_h \tag{5.16}$$

$$Re_{D,h} = \frac{u_{h,in}D}{\nu} = \tilde{u}_{h,in}\tilde{D} \tag{5.17}$$

where D_h represents the hydraulic diameter of the cross section of the upper plenum.

In summary, four dimensionless parameters (Gr, Pr, $Re_{D_h,c}$, $Re_{D,h}$) govern the flows in a heat exchanger with forced convection on the outside and natural convection on the inside. The dimensionless mass flow rate due to circulation by natural convection inside the tubes is

$$\tilde{m} = \sum\left(\frac{\dot{m}_{up}}{\rho H^2 U_s}\right) = \sum\left(\frac{\dot{m}_{down}}{\rho H^2 U_s}\right) \tag{5.18}$$

The subscripts up and down indicate the flow direction inside the tubes. The

dimensionless heat transfer rate from the hot (external) fluid to the cold (internal) fluid is

$$\tilde{q} = \frac{q}{\rho c_p U_s A \Delta T} = \tilde{u}_{h,in}\left(1 - \tilde{T}_{h,out}\right) = \sum\left(\tilde{q}_{conv} + \tilde{q}_{cond}\right)_{\substack{\text{top end} \\ \text{of the tubes}}} \tag{5.19}$$

The conductivity of the tube wall (k_w) is assumed to be much higher than the conductivity of the fluid (k). The ratio $\tilde{k} = k_w/k$ is assumed to have a value sufficiently greater than 1 so that it has a negligible effect on the thermal resistance in the direction perpendicular to the tube. Figure 5.2 shows that the dimensionless thermal conductivity should be larger than 1000, because the heat transfer rate is insensitive to $\tilde{k}$ when $\tilde{k} > 1000$.

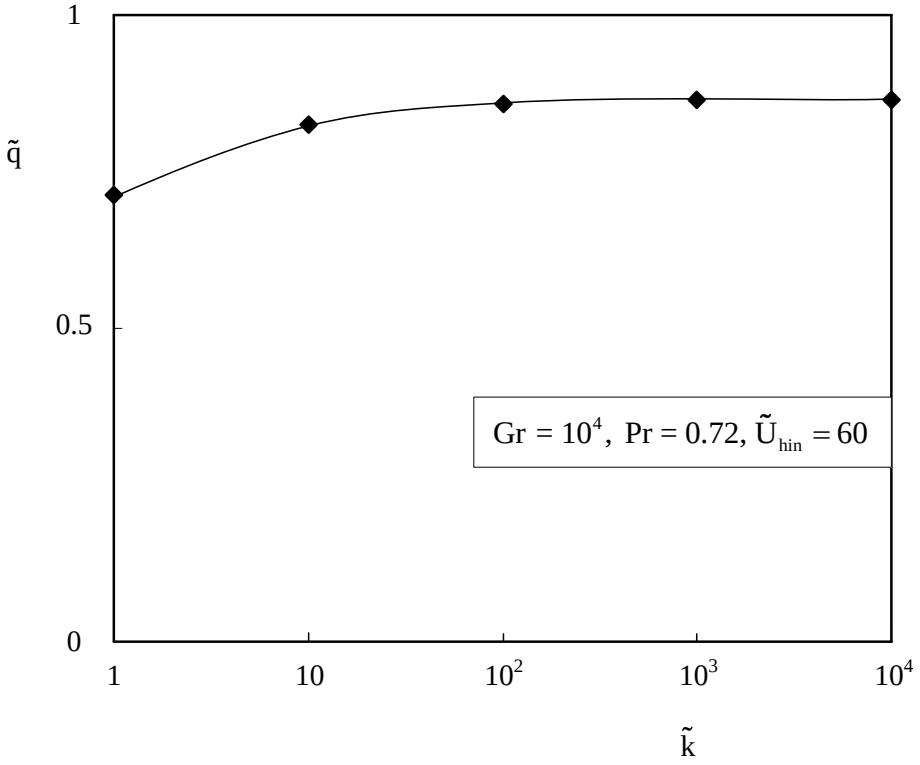

Figure 5.2: The effect of the upper plenum Reynolds number on the contribution made by conduction to the total heat transfer rate.

A finite element package was used for solving the governing equations (5.8)-(5.15) simultaneously [79]. The residuals for mass, momentum and energy equations were assigned values smaller than 10^{-7}, because the change in the dimensionless mass flow rate was less than 10^{-6} when the residuals limit was changed from 10^{-7} to 10^{-8}. Because of numerical limitations, the Gr value for the flow inside of tubes is of order 10^4. The $Re_{D_h,c}$ value for the upper plenum is a degree of freedom, because it depends on the value chosen for the inlet velocity $u_{c,in}$. The $Re_{D_h,c}$ value must be less than 1000, as this is the order of magnitude of the Reynolds number for transition to turbulence in an enclosed space. Figure 5.3 shows that the heat transfer by vertical conduction in the

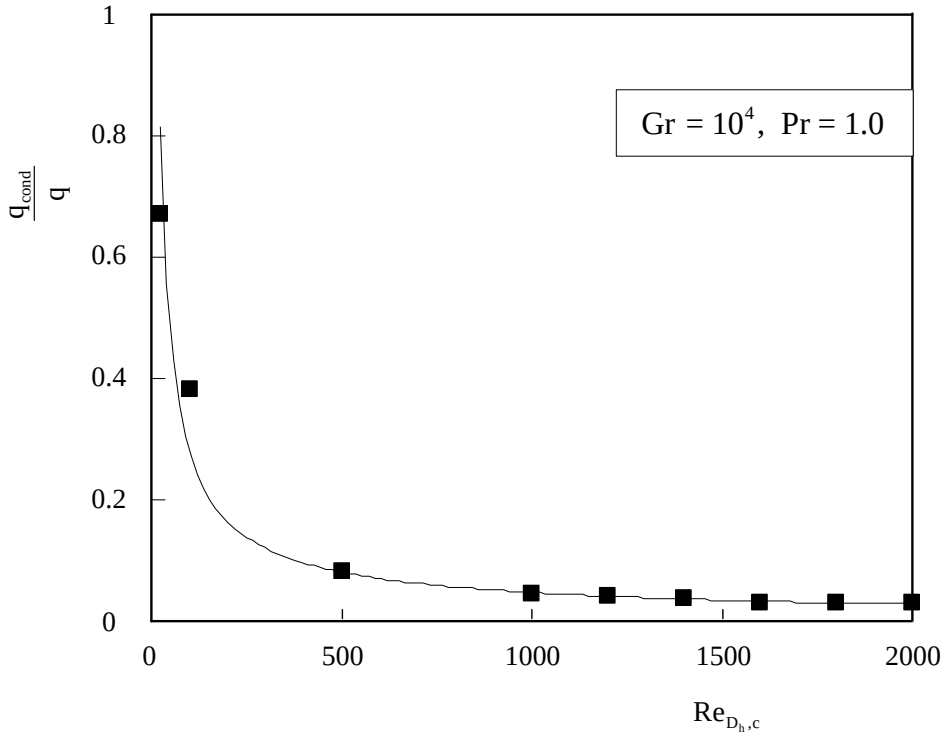

Figure 5.3: The effect of the thermal conductivity ratio on the heat transfer rate.

internal fluid (in the tubes) relative to the total heat transfer rate [Eq. (5.19)] becomes negligible as $Re_{D_h,c}$ is greater than 500. The value $Re_{D_h,c} = 500$ was selected for all the numerical results described in this chapter.

Adiabatic conditions are imposed on the end cross-sections of tubes to rule out the conductive heat transfer from the tube walls to the plenums. In actual heat exchangers [21, 22] the ratio of height to diameter of the tubes is greater than 100, and this rules out the effect of conduction from the tube ends. In the present heat exchanger model, however, the ratio of height to diameter is approximately 6 (Fig. 5.1), and adiabatic tube ends are necessary in order to prevent the conduction along the tube walls, and to isolate the convection effect due to by the circulation established inside the tubes.

5.2 Two tubes

We start with the simplest configuration, which has only two tubes (Fig. 5.1). Heat transfer by natural convection is confirmed in Fig. 5.4, which shows the streamlines and temperature profiles in the middle plane. The flow is upward in the leading tube and downward in the trailing tube, and it is due to the density difference between the two fluid columns. The average dimensionless temperatures in the middle planes of the leading and trailing tubes are 0.75 and 0.35. The volume occupied by the fluid inside the tubes is fixed,

$$\tilde{V}_t = \frac{4V_t}{\pi H^3} = \tilde{h}\left(\tilde{D}_1^2 + \tilde{D}_2^2\right) = \text{constant} \qquad (5.20)$$

Subscripts 1 and 2 indicate the leading and trailing tubes. The dimensionless longitudinal

spacing between two tubes is 0.6. The $\tilde{V}_t$ value is fixed at 0.0441. The volume $\tilde{V}$ occupied by the hot gas flow (around the tubes) is also fixed, and its value is 0.497. These two constant volumes are global constraints and are used in all the calculations reported in this chapter.

Figure 5.5 shows the trend of the dimensionless mass flow rate Eq. (5.18), which is bell-shaped. This behavior is reasonable because the mass flow rate must decay in both limits, $D_1/D_2 \rightarrow 0$ and $D_1/D_2 \rightarrow \infty$. In addition, Fig. 5.5 shows that the maximum flow rate occurs when the tube diameters are approximately the same.

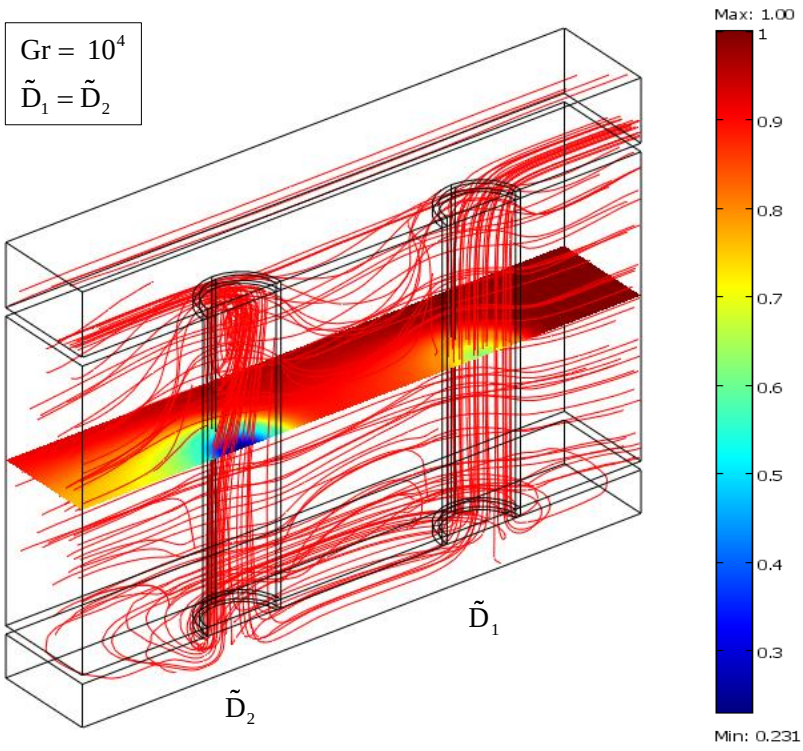

Figure 5.4: Pattern of streamlines in the configuration with two tubes.

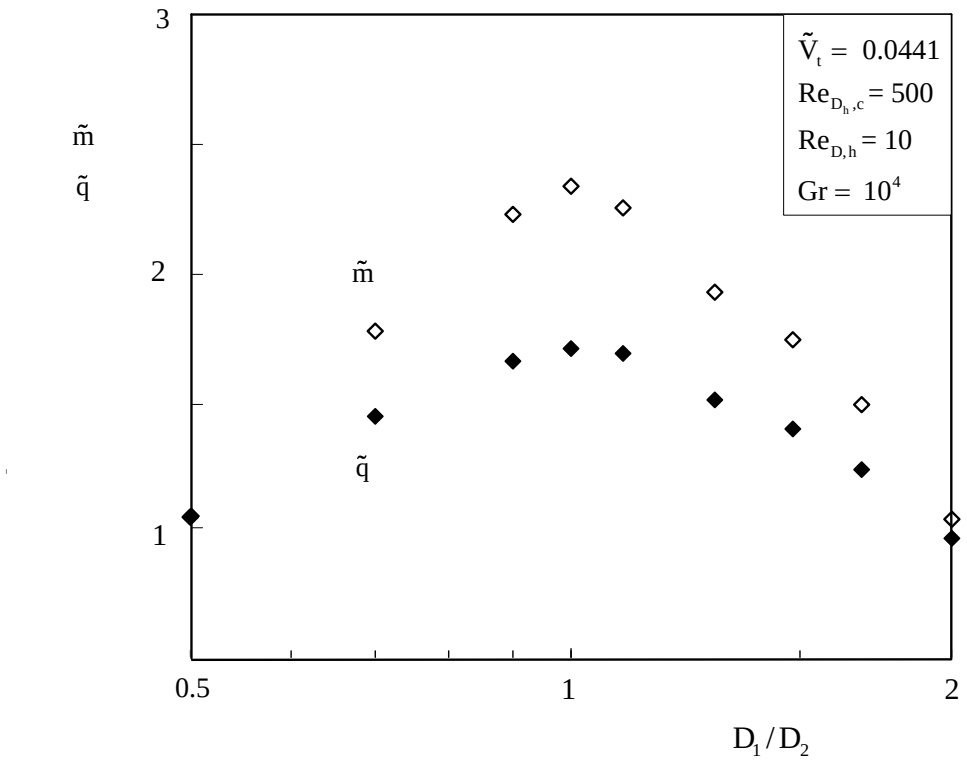

Figure 5.5: The mass flow and heat transfer rates in the configuration with two tubes.

The dimensionless heat transfer rate (Fig. 5.5) has the same trend as the dimensionless mass flow rate. This similarity confirms the dominant effect of convection, which was anticipated when $Re_{D_h,c} = 500$ was selected for the flow rate of cold fluid into the upper plenum, cf. Section 5.1 and Fig. 5.3.

5.3 Three tubes

A step in the direction of more complex heat exchangers is to consider configurations with three tubes. Figure 5.6 shows that the flow direction in the trailing tube is downward and the direction in the other two tubes is upward. To search for the best 3-tube configuration, we fix the diameter of one tube and vary the ratio of the other

two. The total volume constraint is

$$\tilde{V}_t = \frac{4V_t}{\pi H^3} = \tilde{h}\left(\tilde{D}_1^2 + \tilde{D}_2^2 + \tilde{D}_3^2\right) = \text{constant} \qquad (5.21)$$

where 1, 2 and 3 represent the leading, middle and trailing tubes. The dimensionless longitudinal spacing between tubes is uniform and equal to 0.4.

Figure 5.7 shows the dimensionless mass flow and heat transfer rates versus D_2/D_3 when $\tilde{D}_1 = 0.14$. The two curves have the same trend: the convection and mass flow rates increase as the middle tube shrinks. The largest heat transfer rate is obtained in

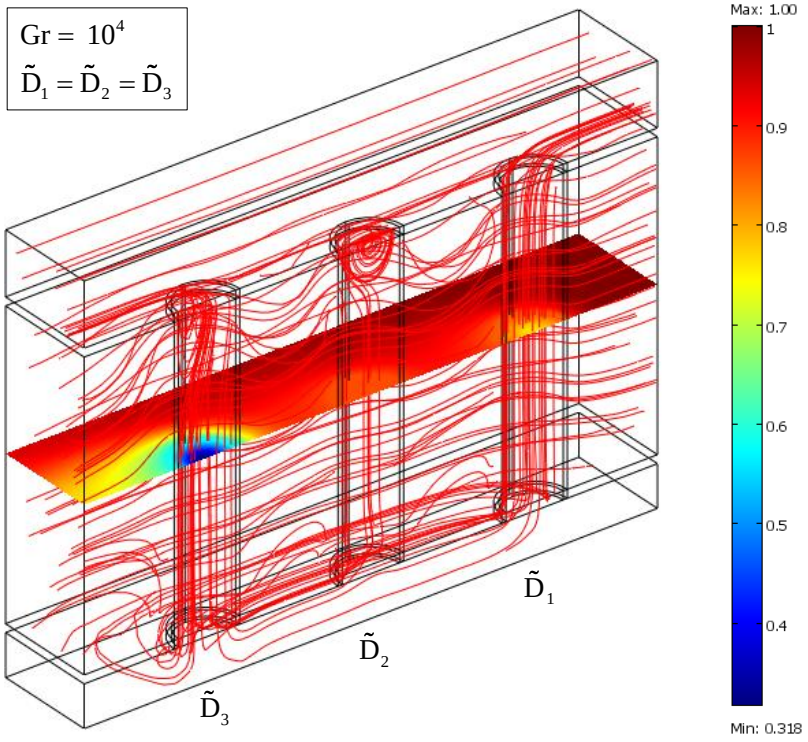

Figure 5.6: Pattern of streamlines in the configuration with three tubes and $D_1 = D_2 = D_3$.

the vicinity of $D_2/D_3 \approx 0.7$ when $\tilde{D}_1 = 0.14$, but we will show next that higher $\tilde{q}$ values are achievable in the limit $D_2/D_3 \to 0$. Figure 5.7 also shows that the flow direction in the middle tube changes when $D_2/D_3 \cong 1.05$.

Figure 5.8 shows the dimensionless mass flow and convective heat transfer rates versus D_1/D_3 when $\tilde{D}_2$ is fixed. The $\tilde{m}$ and $\tilde{q}$ curves exhibit inflexions in the range $0.7 < D_1/D_3 < 1.0$. The highest values occur at $(D_1/D_3)_{max} \cong 0.7$ for $\tilde{m}$, and at $(D_1/D_3)_{max} \cong 1$ for $\tilde{q}$. The flow direction in the middle tube changes when $D_1/D_3 \cong 1.05$.

Figure 5.9 shows the third direction of this search. We fixed $\tilde{D}_3$ and varied D_2/D_1. The mass flow and convective heat flow rates increase when the middle tube shrinks. The peaks of the two curves occur in the vicinity of $D_2/D_1 \approx 0.43$ when $\tilde{D}_3 = 0.14$. The flow reversal in the $\tilde{D}_2$ tube occurs when D_2/D_1 is approximately 0.95.

In summary, if one tube diameter is held fixed, the flow performance is limited by the diameter of the middle tube. For example, if $\tilde{D}_2$ is fixed at the average value of the three tubes (Fig. 5.8), the peak mass and heat flow rates are reduced by 20% relative to the other cases (Figs. 5.7 and 5.9). This means that if the constraint of having fixed one diameter is removed, the performance will improve.

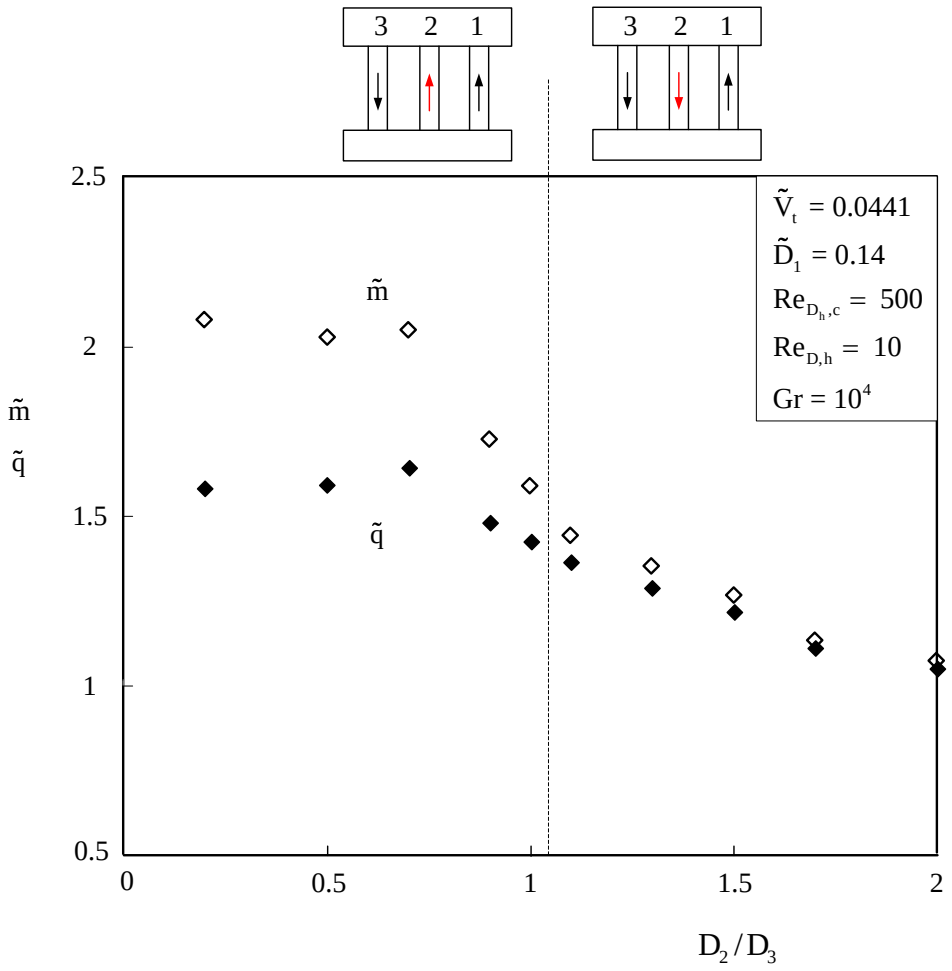

Figure 5.7: The mass flow and heat transfer rates for three tubes and constant D_1.

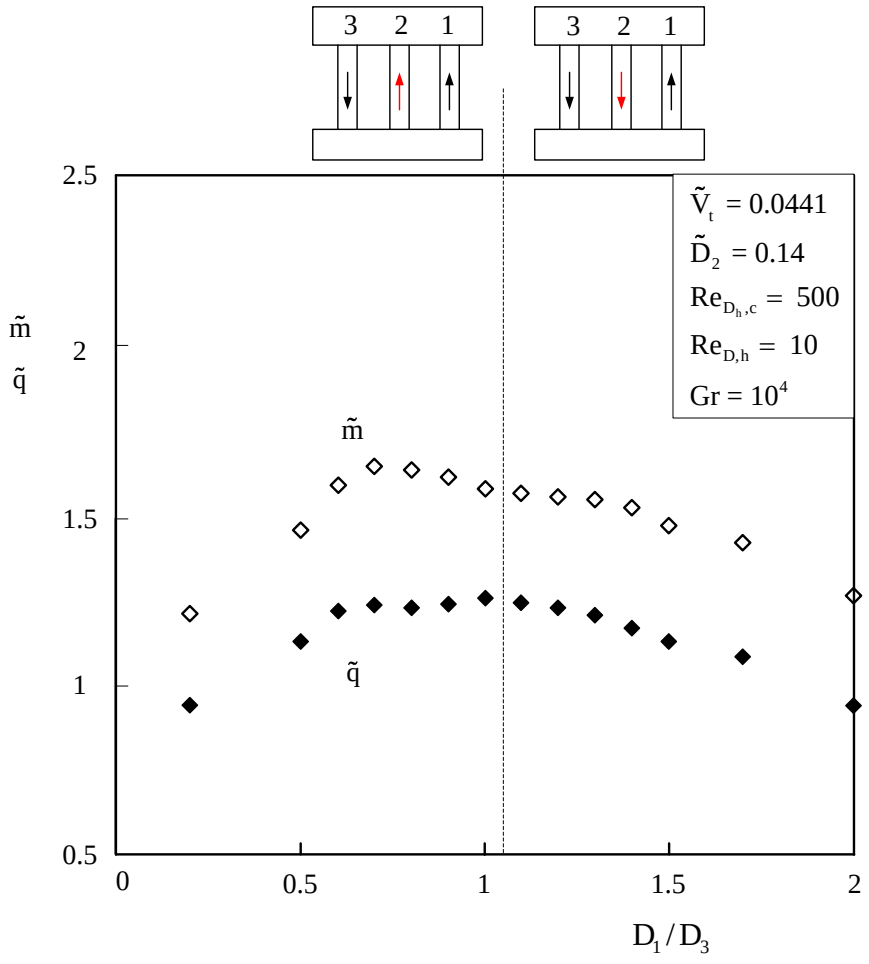

Figure 5.8: The mass flow and heat transfer rates for three tubes and constant D_2.

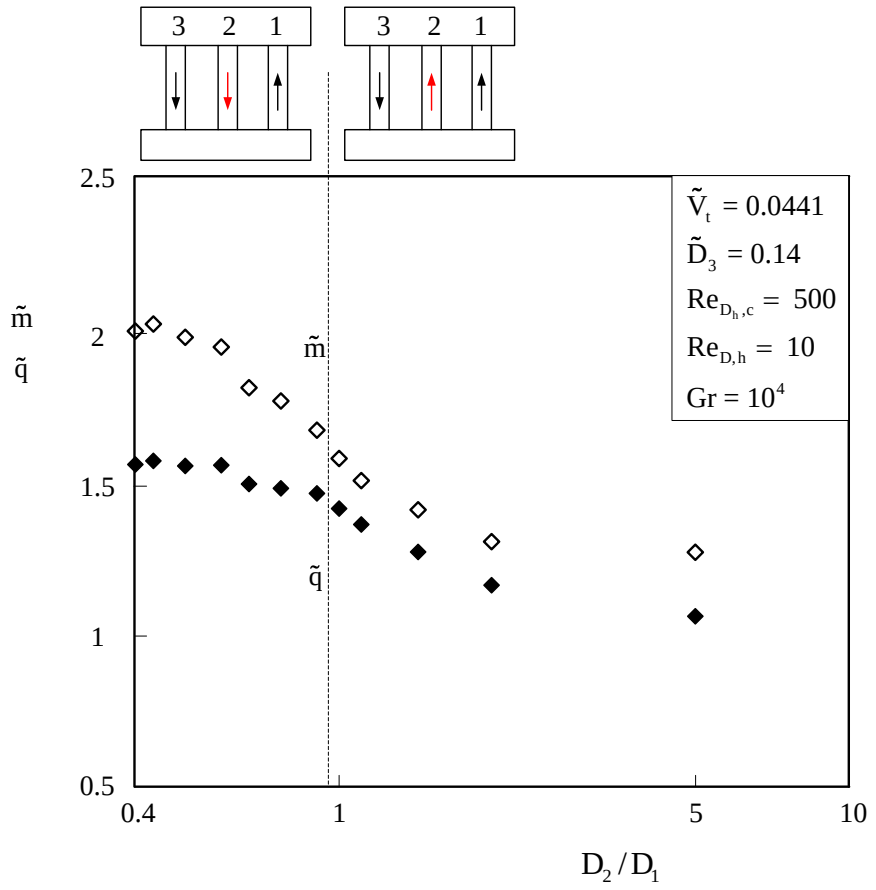

Figure 5.9: The mass flow and heat transfer rates for three tubes and constant D_3.

To vary all the tube sizes subject to the tube volume constraint (5.21) means to vary independently two ratios, D_1/D_3 and D_2/D_3. Figure 5.10 shows the behavior of the mass flow rate. The steepest ascent on the $\tilde{m}$ surface is along $D_1/D_3 \approx 1,$ in the direction of decreasing D_2/D_3. The search for the configuration with the highest flow rate was performed systematically by using

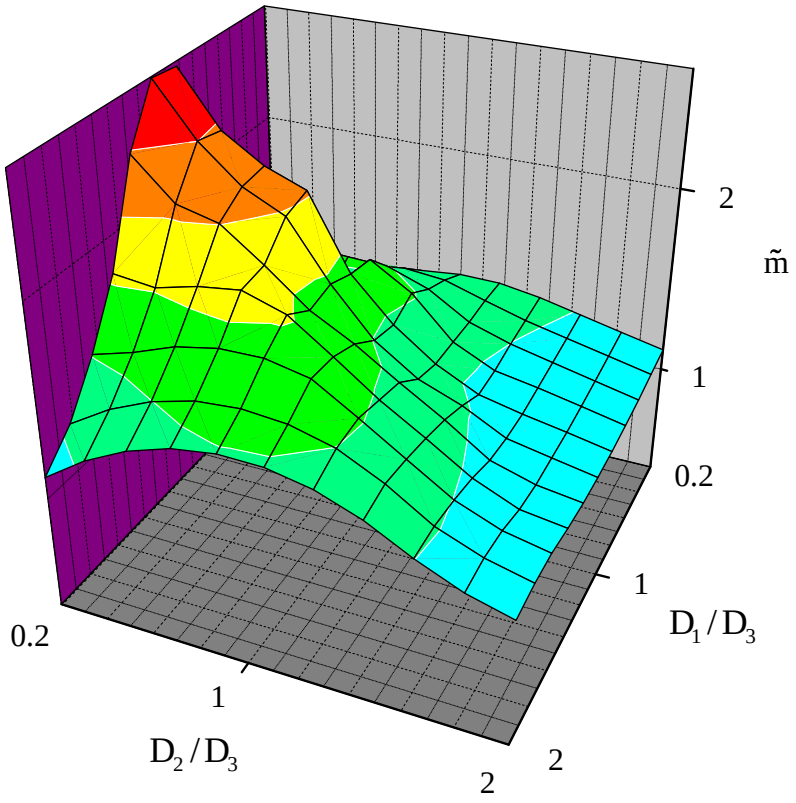

Figure 5.10: The effect of all three tubes on the mass flow rate.

$$\tilde{D}_1 = C_1 \tilde{D}_3$$
$$\tilde{D}_2 = C_2 \tilde{D}_3$$
$$\tilde{D}_3 = \left[\frac{\tilde{V}_t}{\left(1 + C_1^2 + C_2^2\right)} \right]^{1/2} \qquad (5.22)$$

where C_1 and C_2 represent the two degrees of freedom. The steepest gradient is found by manipulating C_1 and C_2. We started with $C_1 = 1$ and $C_2 = 0.7$, which represent the design with the highest mass flow rate based on the previous three searches (Figs. 5.7-5.9).

Figure 5.11 shows that greater design freedom leads to the better performance: both $\tilde{m}$ and $\tilde{q}$ increase as the middle tube vanishes. The values of the peak mass flow

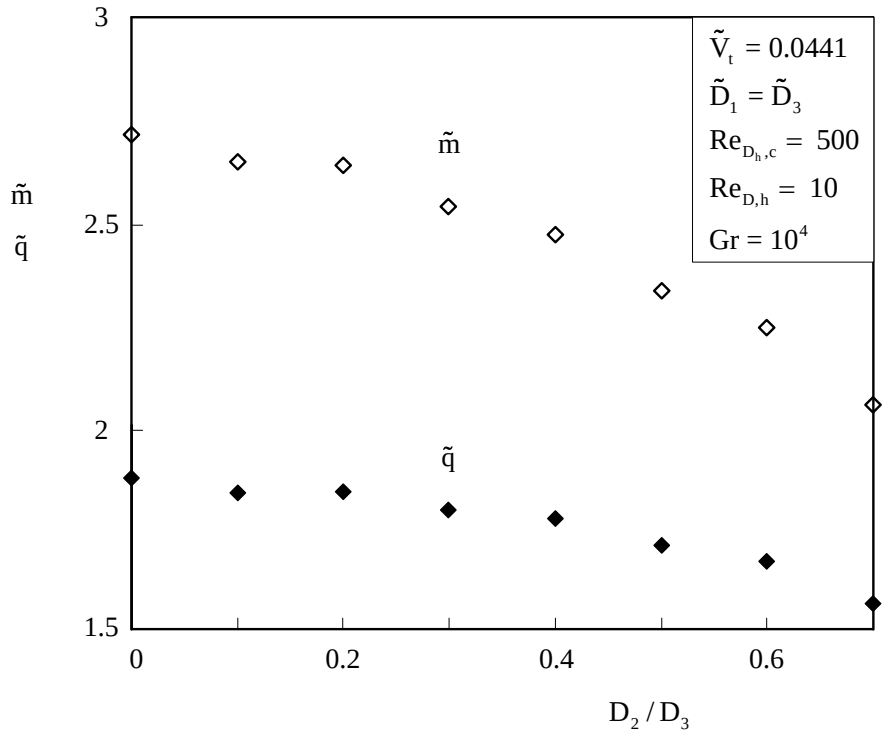

Figure 5.11: The mass flow and heat transfer rates in the configuration with three tubes.

and heat transfer rates increase by 30 % and 20 % respectively relative to the maximum values of the previous searches (Figs. 5.7-5.9) which were based on one fixed tube diameter.

5.4 The effect of the position of the middle tube

In the configurations developed so far, the tubes were equidistant during the search. Now we vary the position of the middle tube (D_2), by varying the distance $\tilde{L} = L / (D_2/2)$ defined in Fig. 5.12. The results for $\tilde{m}$ and $\tilde{q}$ show the effect of $\tilde{L}$ when $\tilde{D}_1 = \tilde{D}_3$ and $D_2/D_3 =$ 0.5 and 0.7. The mass flow and heat transfer rates oscillate as the middle tube moves from touching the leading tube ($\tilde{L}$ = 1) to touching the trailing tube (the largest $\tilde{L}$ value depends on D_2/D_3: see the dashed lines in Fig. 5.12). Each curve exhibits a peak value. For example, the highest mass and heat flow rates for $D_2/D_3 = 0.5$ occur when the position of the middle tube is $\tilde{L}_{opt} \cong 1.5$, i.e. close to the leading tube.

In spite of the new degree of freedom ($\tilde{L}$), the peak values do not exceed the peaks shown in Fig. 5.11 ($\tilde{m}_{3,max} = 2.7$ and $\tilde{q}_{3,max} = 1.9$). For example, even though the peak mass flow rate for $D_2/D_3 = 0.7$ exceeds by 13 % the value when the middle tube is in the center, this peak mass flow rate is significantly less than its highest possible value (Fig. 5.11). As the diameter of the middle tube becomes smaller the effect of changing its position decreases. In summary, the change of the middle tube position confirms the

maxima obtained in Fig. 5.11. The best performance is obtained when the middle tube is removed for 3-tube model.

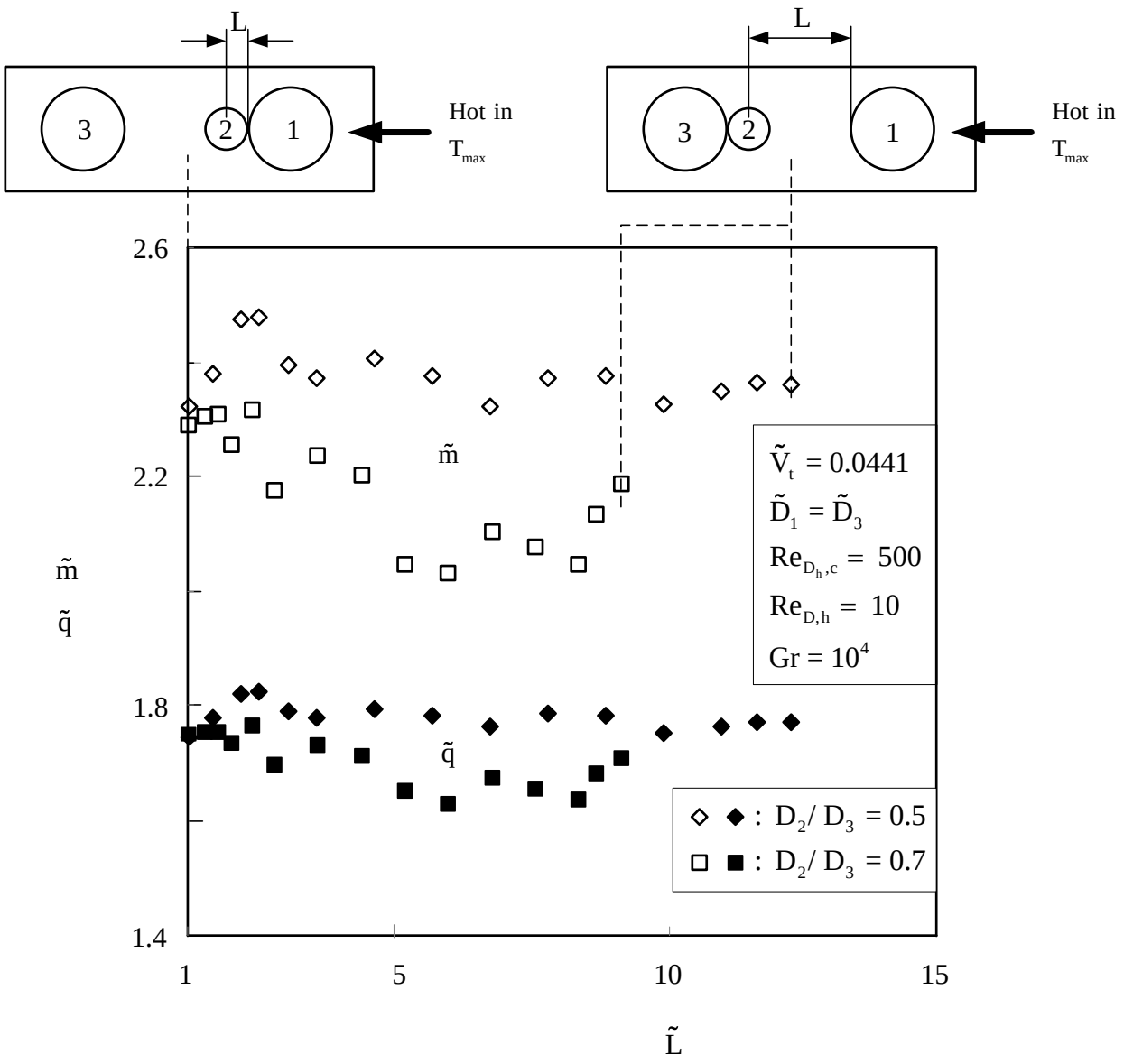

Figure 5.12: The effect of the position of the middle tube on the mass flow and heat transfer rates of the configuration with three tubes.

5.5 Four tubes

The next step toward more complex configurations is the 4-tube assembly shown in Fig. 5.13. We used two sizes, the larger size for the two outer tubes ($D_1 = D_4$), and the smaller size for the two inner tubes ($D_2 = D_3$), and then we varied the size ratio, D_3/D_4, or D_2/D_1. The dimensionless longitudinal spacing between tubes is uniform and equal to 0.28.

Figure 5.13 shows that the maximum values of $\tilde{m}$ and $\tilde{q}$ are reached when the two middle tubes vanish. The highest values are $\tilde{m}_{4,max} = 3.28$ and $\tilde{q}_{4,max} = 2.09$. Even though local peaks appear in the vicinity of $D_3/D_4 = 0.3$, these peaks are considerably lower than $(\tilde{m}, \tilde{q})_{4,max}$.

Another look at the effect of configuration on global performance is presented in Fig. 5.14, where there are three tube sizes: D_2, D_3 and $D_1 = D_4$. The ratio of the inner sizes D_2/D_3 varies, and the results for $\tilde{m}$ and $\tilde{q}$ oscillate. The peak mass flow rate appears in the vicinity of $D_2/D_3 \cong 1.1$, and it is 4% higher than the value when sizes of the two middle tubes are the same. The peak $\tilde{m}$ value does not exceed the highest value, $\tilde{m}_{4,max}$, because when the middle tubes have finite size the mass flow rate is less than half of $\tilde{m}_{4,max}$, as shown in Fig. 5.13.

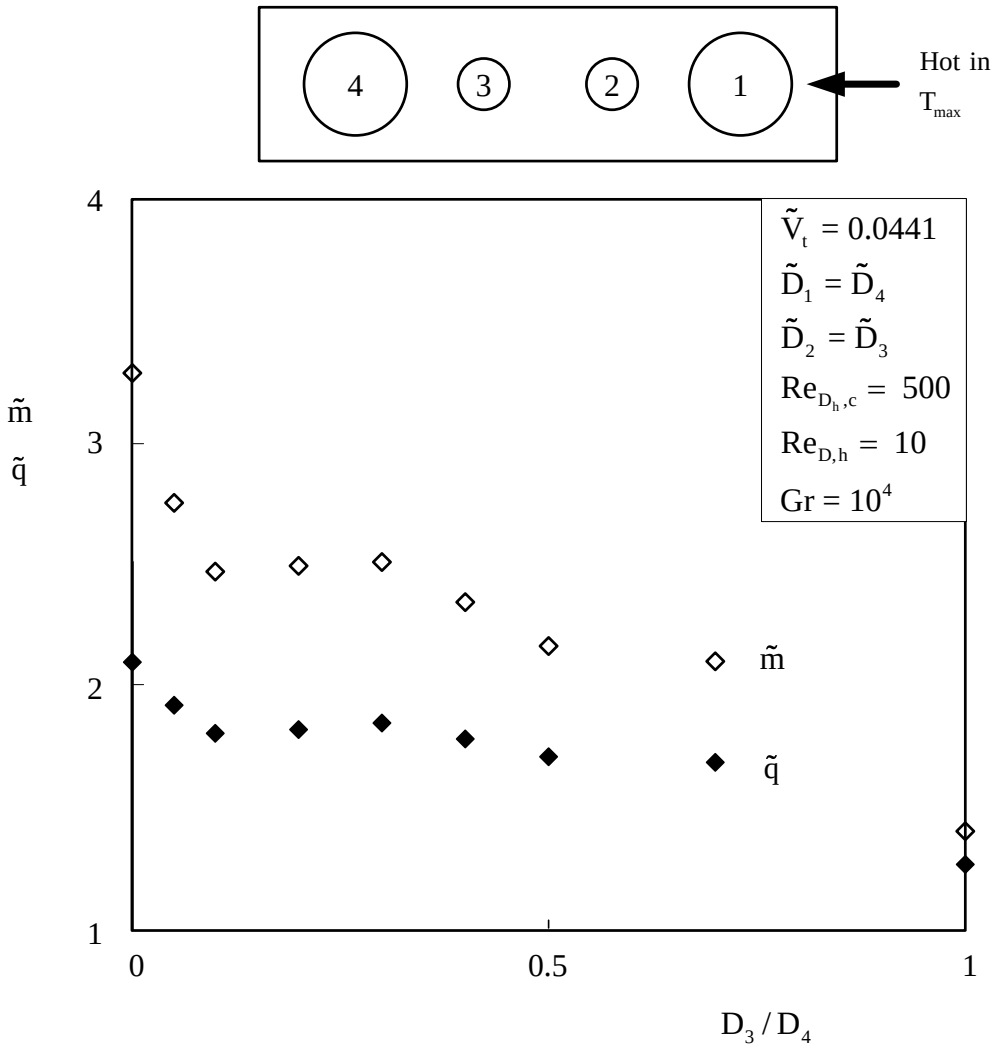

Figure 5.13: The mass flow and heat transfer rates for the configuration with four tubes and two sizes, $D_1 = D_4$ and $D_2 = D_3$.

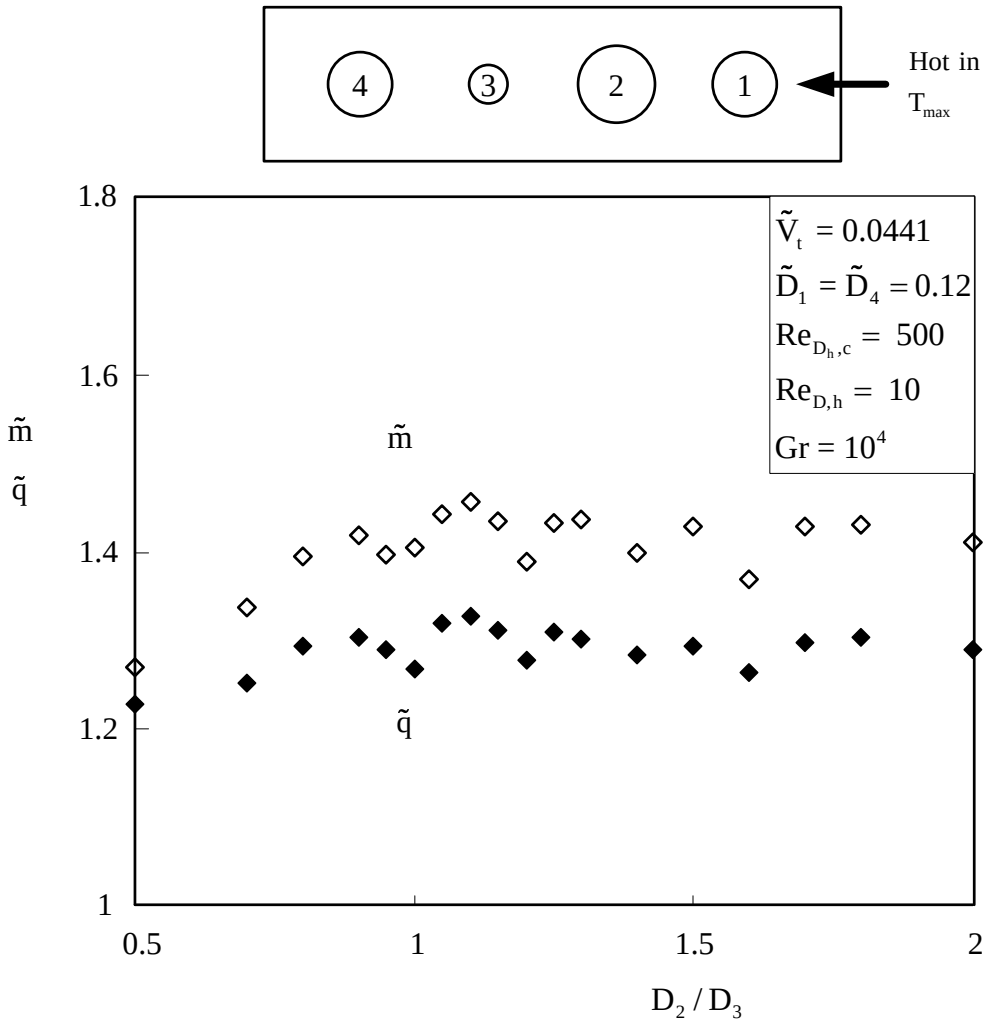

Figure 5.14: The mass flow and heat transfer rates for the configuration with four tubes when $D_1 = D_4 = \text{constant}$ and D_2/D_3 varies.

5.6 Results and discussion

In this chapter we showed numerically how the geometric configuration of the tubular flow structure controls the global performance of a crossflow heat exchanger. The cold side is driven by natural convection and consists of a thermosyphon flowing in vertical tubes attached to two plenums. The hot side consists of hot gases that flow perpendicularly to the tubes, and heat the tubes by crossflow forced convection. The fluid is the same on both sides of the heat transfer surface.

The objective was to determine the number of tubes in crossflow such that the global heat transfer rate from the hot side to the warm side is maximum. Related to this objective was the maximization of the circulation rate in the vertical tubes of the thermosyphon. We found that the configuration for maximum convection ($\tilde{q}$) is nearly the same as the configuration for maximum circulation rate ($\tilde{m}$). In other words, in the search of optimal flow configuration it is sufficient to focus on the one global criterion, for example, the highest convection rate.

The main conclusion is that it is possible to determine the flow configuration by morphing the entire flow structure in pursuit of progressively higher global heat transfer rates between the hot side and cold side. This is in line with the method of design with constructal theory [2], and it is a clear departure from modern practice where the multi-tube flow configuration has a single tube size and tube spacing [47, 49].

The search for the flow configuration was pursued systematically, from the simplest configuration (two tubes) to more complex (three and four tubes). In each case

we found that there is a particular configuration that offers maximum global performance. When the cold fluid circulates in two vertical tubes, the best configuration has tubes with nearly the same diameter (Fig. 5.5). When the configuration has three tubes, the best designs emerge when the second tube (D_2) vanishes (Fig. 5.10). If the spacing between tubes is allowed to vary, then it is possible to optimize the spacing as well (Fig. 5.12), although the conclusion drawn based on Fig. 5.10 still holds.

When the cold fluid circulates in four vertical tubes (Fig. 5.13), the better configurations are again the ones in which the inner tubes (D_2, D_3) disappear. By varying the diameter rates D_2/D_3, we found that an optimal relative size exists (Fig. 5.14), however, the main trend is toward higher $\tilde{m}$ and $\tilde{q}$ values as the two inner tubes varnish (Fig. 5.13).

Why are these findings important? First, they represent a “free” approach to the discovery of flow configurations for heat exchangers with natural and forced convection. The prevailing method today calls for traditional, one-scale configuration, such as numerous vertical tubes with the same diameter and spacing. Second, these results show that even when we allow for three or four tubes to exist, the morphing of the flow architecture takes us back to the configuration with just two vertical tubes. Third, design difficulties such as determining the flow reversal location and finding maximal circulation rate might be resolved by applying these results to the design procedure of the heat exchangers.

6. Constructal Structure for Crossflow Heat Exchangers

Crossflow heat exchangers are a classical configuration that has generated a considerable literature of research and development, which is found in most textbooks and handbooks (e.g. Refs [80-91]). This type of heat exchangers such as heaters, condensers and evaporators has been designed and manufactured for power plants and desalination plants. The classical approach in this domain of design is to consider the configuration as given, and to evaluate its performance. In this chapter we propose to start from the thinking standpoint where the configuration does not exist and must be determined. We know only that an external fluid must flow perpendicularly to another stream of fluid that flows inside a tube of known diameter.

We begin with the single tube in which condensation is assumed on the outer surface, and step by step we discover the appropriate tube length, the number of tubes, the spacings between tubes, and the global effectiveness and heat transfer density of the structure. Using constructal theory we search for the configuration of crossflow heat exchangers which gives higher heat transfer rate.

6.1 Crossflow heat exchangers with condensation

In this section, we consider crossflow heat exchangers with condensation on the outer surface of tubes. The fluid inside tubes is warmed by a heat transfer due to condensation. The diameter of tube and the heat transfer coefficient are assumed to be constant. The two inlet temperatures, T_0 and T_∞ are also fixed. The optimal configuration

of crossflow heat exchangers is searched by segmenting a tube.

6.1.1 Single tube design

Figure 6.1 shows the crossflow heat exchange which consists of one tube. The cold fluid inside the tube is warmed from T_0 to T_L by heat released due to condensation. The temperature of the external fluid remains at T_∞. The heat transfer rate is [33]

$$q_1 = \dot{m}c_P\left(T_\infty - T_0\right)\left(1 - e^{-hA/\dot{m}c_P}\right) \tag{6.1}$$

or in dimensionless form

$$\tilde{q}_1 = \left(1 - e^{-\tilde{L}}\right) \tag{6.2}$$

where

$$\tilde{q}_1 = \frac{q_1}{\dot{m}c_P\Delta T} \tag{6.3}$$

$$\tilde{L} = \frac{\pi DLh}{\dot{m}c_P} \tag{6.4}$$

$$\Delta T = T_\infty - T_0 \tag{6.5}$$

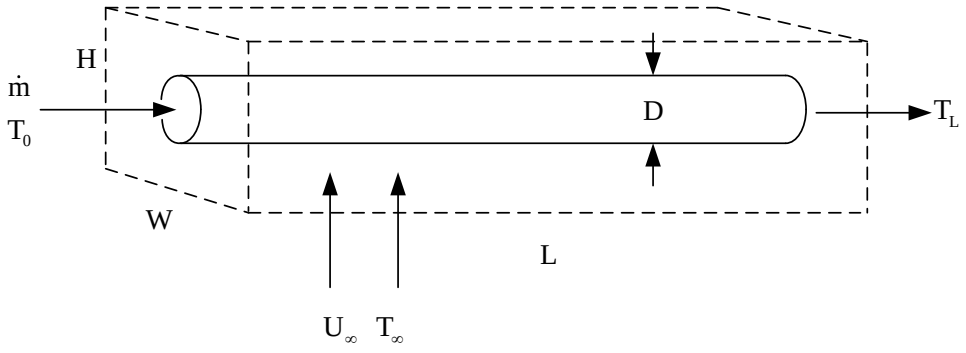

Figure 6.1: Crossflow heat exchanger with condensation.

Using Eq. (6.1) the volumetric heat transfer rate can be written as

$$q_1''' = \frac{h\pi D\Delta T}{HW\tilde{L}}\left(1 - e^{-\tilde{L}}\right) \tag{6.6}$$

where subscript 1 represents the single tube design. The dimensionless volumetric heat transfer rate is

$$\tilde{q}_1''' = \frac{1}{\tilde{L}}\left(1 - e^{-\tilde{L}}\right) \tag{6.7}$$

where

$$\tilde{q}_1''' = \frac{q_1'''HW}{\pi Dh\Delta T} \tag{6.8}$$

The change rate of $\tilde{q}_1'''$ with $\tilde{L}$ is obtained

$$\frac{\partial \tilde{q}_1'''}{\partial \tilde{L}} = \frac{e^{-\tilde{L}}}{\tilde{L}} - \frac{1 - e^{-\tilde{L}}}{\tilde{L}^2} \tag{6.9}$$

Figure 6.2 shows the volumetric heat transfer rate and its change rate with the length. We see that the volumetric heat transfer rate has the maximum value at $\tilde{L} = 0$, and it decreases to zero when the length increases. This means that the increase of the length is not effective in augmenting the heat transfer rate when the length increases beyond a certain value. An alternative to increases the heat transfer rate is to segment the fixed length as shown in Fig. 6.3. The fixed length is divided equally into N segments. The original flow volume is also segmented into N equal pieces of size HWL/N and these

pieces are now stacked as a column of height NH. They are all bathed by an external stream of temperature T_∞.

In Fig. 6.3 $\dot{m}_1$ represents the mass flow rate for the each tube. In the following two sections we search for the configuration for two types of this flow rate: fixed mass flow rate for each segment, and fixed total mass flow rate. In the first case every tube has the same mass flow rate $\dot{m}$ as the single tube design shown in Fig. 6.1. In the second case the fixed total mass flow rate is divided equally into $\dot{m}/N$ among the tubes.

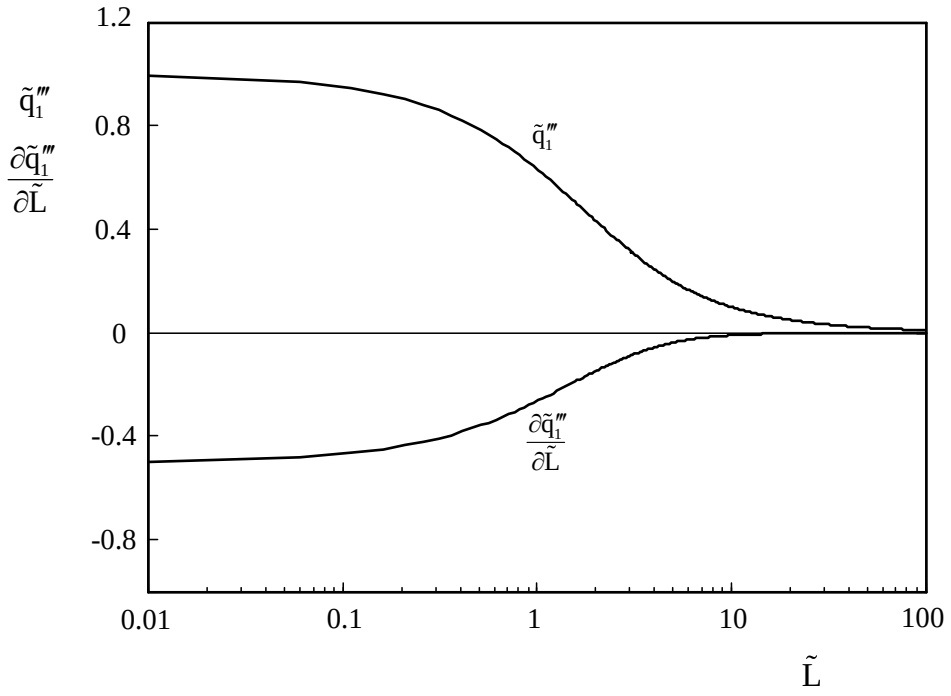

Figure 6.2: The volumetric heat transfer rate and its derivative verse the tube length.

6.1.2 Multi-tube design with the fixed mass flow rate in every tube

We assume that every tube segment has the same mass flow rate, $\dot{m}_1 = \dot{m}$. According to Eq. (6.7) the dimensionless volumetric heat transfer rate for the one segment is

$$\tilde{q}'''_{2,\,\dot{m},\,seg} = \frac{N}{\tilde{L}}\left(1 - e^{-\tilde{L}/N}\right) \tag{6.10}$$

where subscript 2 and $\dot{m}$ represent the multi-tube design and the fixed mass flow rate in every tube. The dimensionless total heat transfer rate for the multi-tube design is obtained by multiplying Eq. (6.10) by the volume of the one segment and the number of tubes

$$\tilde{q}_{2,\dot{m}} = N\left(1 - e^{-\tilde{L}/N}\right) \tag{6.11}$$

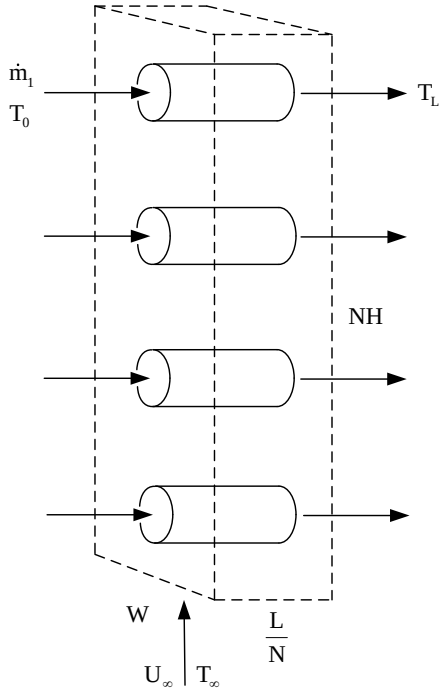

Figure 6.3: Stack of parallel tubes in crossflow.

Figure 6.4 shows how $\tilde{q}_{2,\dot{m}}$ varies with $\tilde{L}$ and N. When N increases the heat transfer rate increases and it approaches $\tilde{L}$ when $N \to \infty$. Each length has the different critical number of segments above which the heat transfer rate is insensitive to N.

The maximum dimensionless heat transfer rate is found by solving

$$\frac{\partial \tilde{q}_{2,\dot{m}}}{\partial N} = 1 - e^{-\tilde{L}/N}\left(1 + \frac{\tilde{L}}{N}\right) = 0 \tag{6.12}$$

This equation is satisfied when $N \to \infty$; corresponding maximum dimensionless heat transfer rate is obtained

$$\tilde{q}_{2,\dot{m},max} = \lim_{N\to\infty}\left[\frac{1 - e^{-\tilde{L}/N}}{1/N}\right] = \tilde{L} \tag{6.13}$$

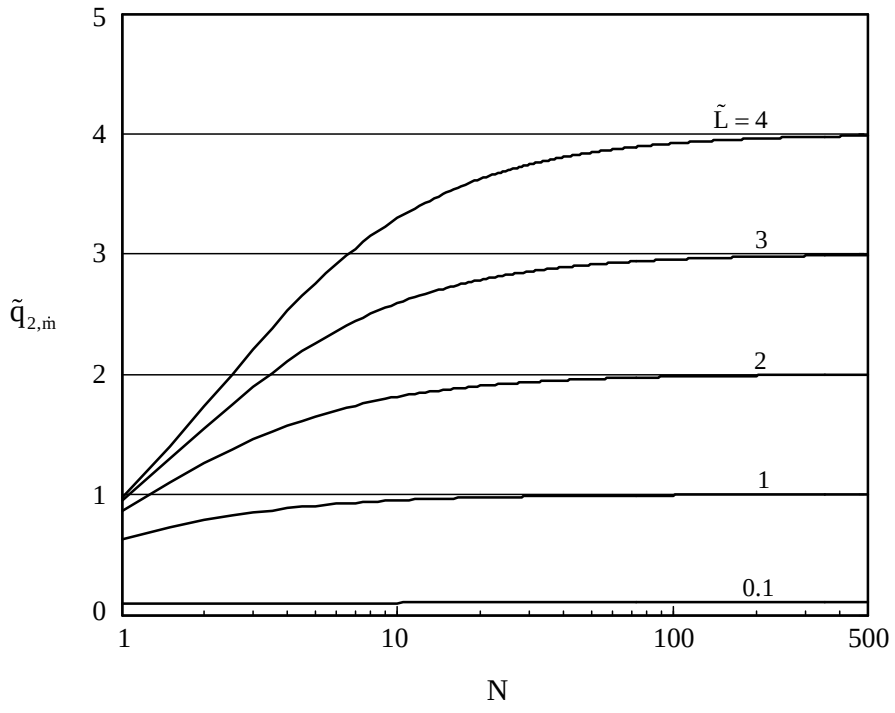

Figure 6.4: The heat transfer rate when the mass flow rate is the same in every tube.

According to Eqs. (6.3) and (6.4) the maximum heat transfer rate is written as

$$q_{2,\dot{m},max} = (\pi DL)h\Delta T \tag{6.14}$$

This equation shows that the maximum heat transfer rate equals the theoretical heat transfer rate which can be defined as multiplying area, heat transfer coefficient and the maximum temperature difference in the heat exchanger. We also see that the theoretical heat transfer rate can be achieved by segmenting a tube into many tubes.

The effectiveness of the multi-tube design is defined

$$\varepsilon_{2,\dot{m}} = \frac{\tilde{q}_{2,\dot{m}}}{\tilde{q}_{2,\dot{m},max}} = \frac{N}{\tilde{L}}\left(1 - e^{-\tilde{L}/N}\right) \tag{6.15}$$

Figure 6.5 shows the effectiveness of the multi-tube design with the fixed mass flow rate

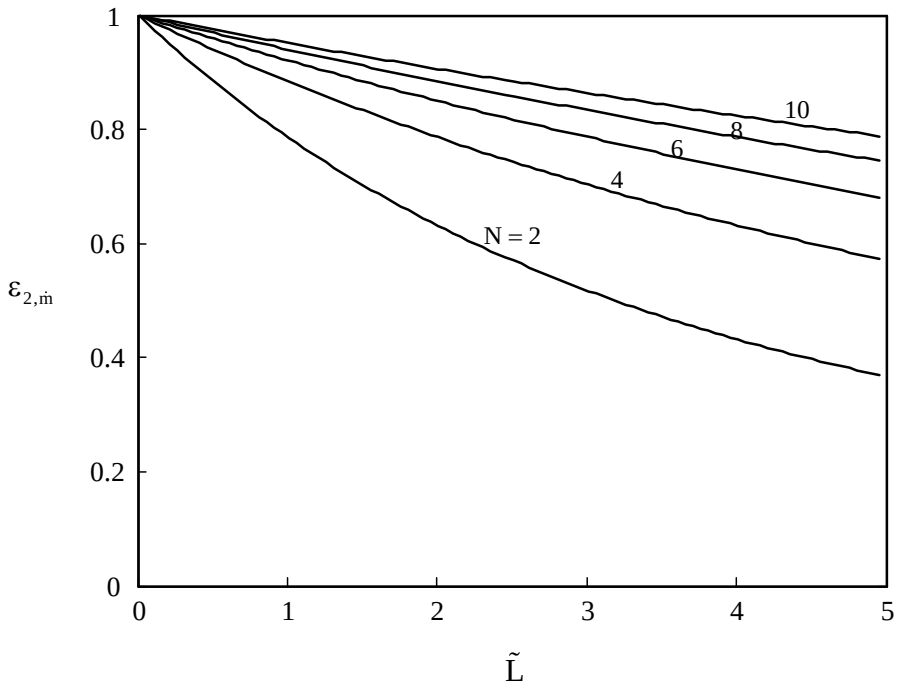

Figure 6.5: The effectiveness of the multi-tube design with the same mass flow rate in every tube.

of each tube; they decrease for all Ns when $\tilde{L}$ increases. We see that the effectiveness becomes less sensitive to $\tilde{L}$ and approaches to 1.0 when N increases.

According to Eqs. (6.2) and (6.11) the goodness of the multi-tube design relative to the single-tube design is indicated by the ratio,

$$\frac{\tilde{q}_{2,\dot{m}}}{\tilde{q}_1} = \frac{N\left(1-e^{-\tilde{L}/N}\right)}{1-e^{-\tilde{L}}} \tag{6.16}$$

Figure 6.6 shows that the multi-tube design with the fixed mass flow rate of each tube is superior to the single tube design for any $\tilde{L}$ and N and the multi-tube design

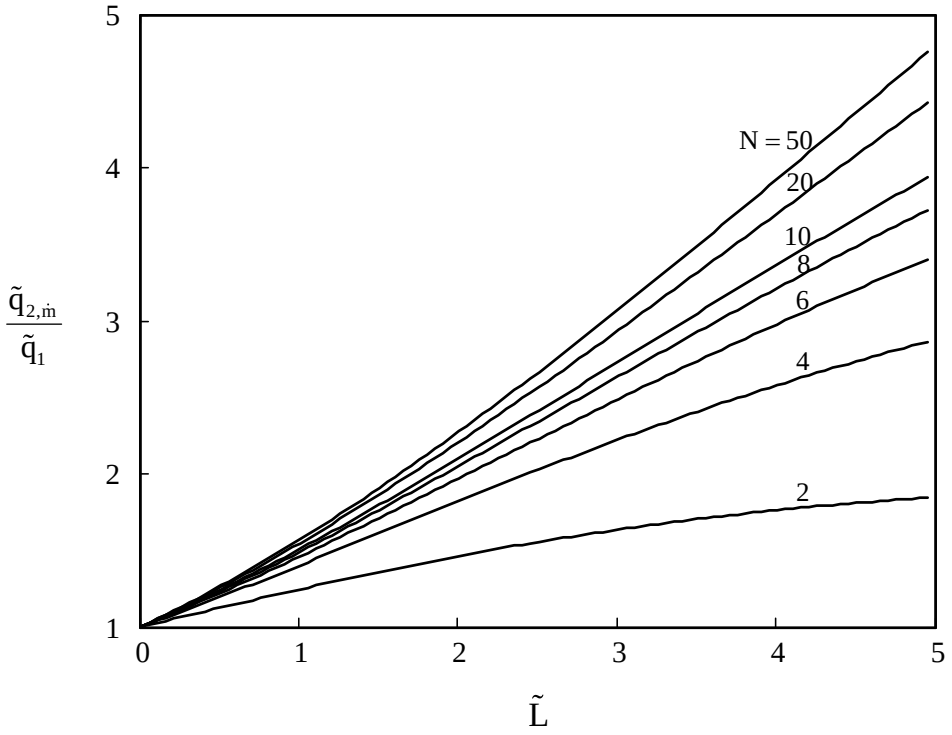

Figure 6.6: The relative goodness of the multi-tube design with the same mass flow rate in every tube.

gives a better heat transfer rate for longer tube and more segmenting when the outer surface of tubes is isothermal.

6.1.3 Multi-tube design with the fixed total mass flow rate

When the total mass flow rate is fixed, the mass flow rate of each tube is $\dot{m}_1 = \dot{m}/N$. Using Eq. (6.7), the dimensionless volumetric heat transfer rate for one segment can be written as

$$\tilde{q}'''_{2,\dot{m}/N,seg} = \frac{1}{\tilde{L}}\left(1-e^{-\tilde{L}}\right) \tag{6.17}$$

where subscript $\dot{m}/N$ represents the fixed total mass flow rate. Multiplying Eq. (6.17) by volume of one segment and the number of tubes yields the dimensionless total heat transfer as

$$\tilde{q}_{2,\dot{m}/N} = 1-e^{-\tilde{L}} \tag{6.18}$$

We see that the dimensionless heat transfer rate for the multi-tube design is identical to that of the single tube structure, cf. Eq. (6.2), if the total mass flow rate is fixed during segmenting a tube

$$\frac{\tilde{q}_{2,\dot{m}/N}}{\tilde{q}_1} = 1 \tag{6.19}$$

In other words, the segmenting of the tube does not affect the total heat transfer rate when the total mass flow rate is fixed.

6.2 Crossflow heat exchangers

For the analysis of crossflow heat exchangers without condensation we also use Figs. 6.1 and 6.3. With reference to Fig. 6.1, we assume that the fluid inside the tube is warmed in crossflow by the external fluid of temperature T_∞, velocity U_∞ and specific heat $c_{P,\infty}$ where T_∞ is a constant. The assumption of the constant T_∞ may seem unreasonable because there is no condensation on the outer surface of the tubes. However, this assumption is a good approximation when the external surface is finned and the effective heat transfer coefficient is considerably greater than the internal heat transfer coefficient. On the other hand, in the stack of tubes as shown in Fig. 6.3 the fluid temperature inside tubes is assumed to be constant. This assumption is acceptable when the tubes are sufficiently short, i.e. when N is very large. Temperature of the external flow decreases as it flows over tubes in crossflow. The external mass flow rate, $\dot{m}_\infty$, depends on N as

$$\dot{m}_\infty = \rho_\infty W\left(\frac{L}{N}\right)U_\infty \tag{6.20}$$

6.2.1 Which is the better configuration?

For the single tube design as shown in Fig. 6.1, we can use the same formula, cf. Eq. (6.7), for the dimensionless volumetric heat transfer rate. For the multi-tube design as shown in Fig. 6.3, however, we need to derive a new formula because the mass flow rate depends on segmenting as shown in Eq. (6.20); the dimensionless volumetric heat transfer

rate is written as

$$q_2''' = \frac{\dot{m}_\infty c_{P,\infty}}{HWL}\Delta T\left(1-e^{-N/u}\right) \tag{6.21}$$

where

$$u = \frac{\rho_\infty W U_\infty c_{P,\infty}}{h\pi D} \tag{6.22}$$

According to Eqs. (6.7), (6.8) and (6.21), the ratio of heat transfer rates for both designs is

$$\frac{q_2}{q_1} = \frac{q_2'''}{q_1'''} = \frac{\left(1-e^{-N/u}\right)}{\left(1-e^{-\tilde{L}}\right)}\frac{\tilde{L}u}{N} \tag{6.23}$$

Figure 6.7 shows this ratio in which the multi-tube design has superiority over the single tube design when

$$1 < \tilde{L}\frac{u}{N} \tag{6.24}$$

According to Eqs. (6.4) and (6.22) this criterion can be written

$$\frac{C_{ext}}{C_{int}} > 1 \tag{6.25}$$

where

$$C = \dot{m}c_P \tag{6.26}$$

We can see that the multi-tube design has the better heat transfer rate than the single tube design when the capacity rate of the external fluid is greater than the internal

fluid. Here we have to be cautious about dependence of $\dot{m}_\infty$ on the number of segment, N; it means that C_{ext}/C_{int} is not constant but variable. For example, this capacity ratio becomes less than one according to Eq. (6.20) if N increases. From Eq. (6.25) we obtain the critical number of segments

$$N_{critical} = \frac{\rho_\infty W U_\infty c_{P,\infty} L}{\dot{m} c_P} \tag{6.27}$$

This equation implies that the multi-tube design is superior to the single tube design when the number of tube is less than $N_{critical}$. In other words, if N is greater than $N_{critical}$ the capacity rate of the external fluid is less than that of the internal fluid.

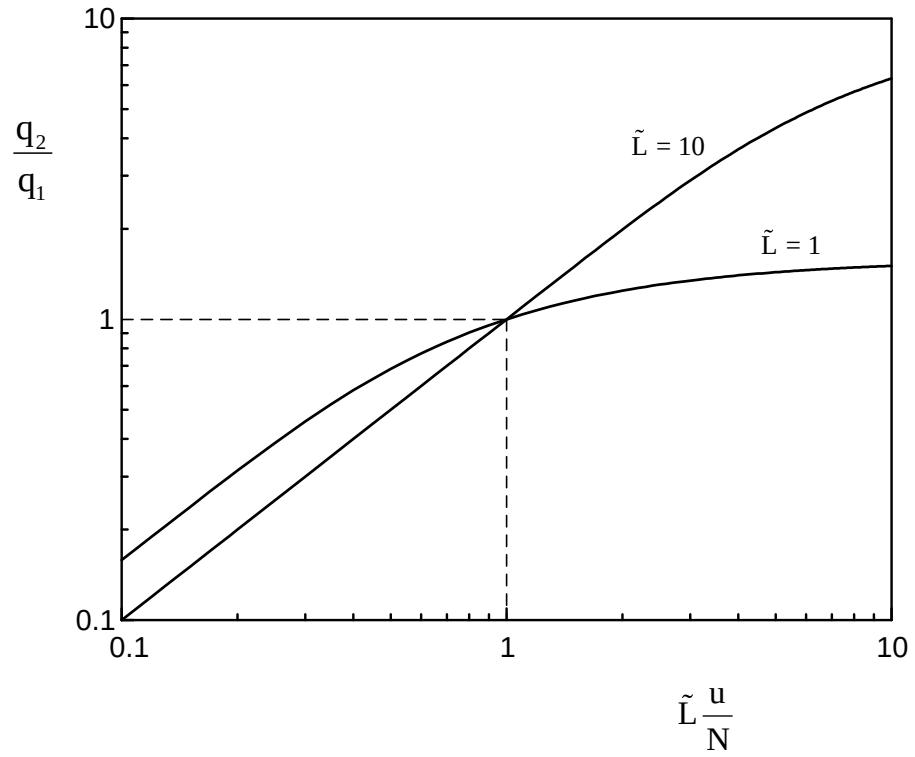

Figure 6.7: The relative heat transfer rate with $\tilde{L}u/N$.

The design criteria is found based on the u and $\tilde{L}$ by setting $q_2/q_1 = 1$ in Eq. (6.23)

$$\frac{\left(1-e^{-y}\right)}{y} = \frac{\left(1-e^{-\tilde{L}}\right)}{\tilde{L}} \tag{6.28}$$

where

$$y = \frac{N}{u} \tag{6.29}$$

In Eq. (6.28) the left hand side term is exactly the same as the right hand side when

$$\tilde{L} = \frac{N}{u} \tag{6.30}$$

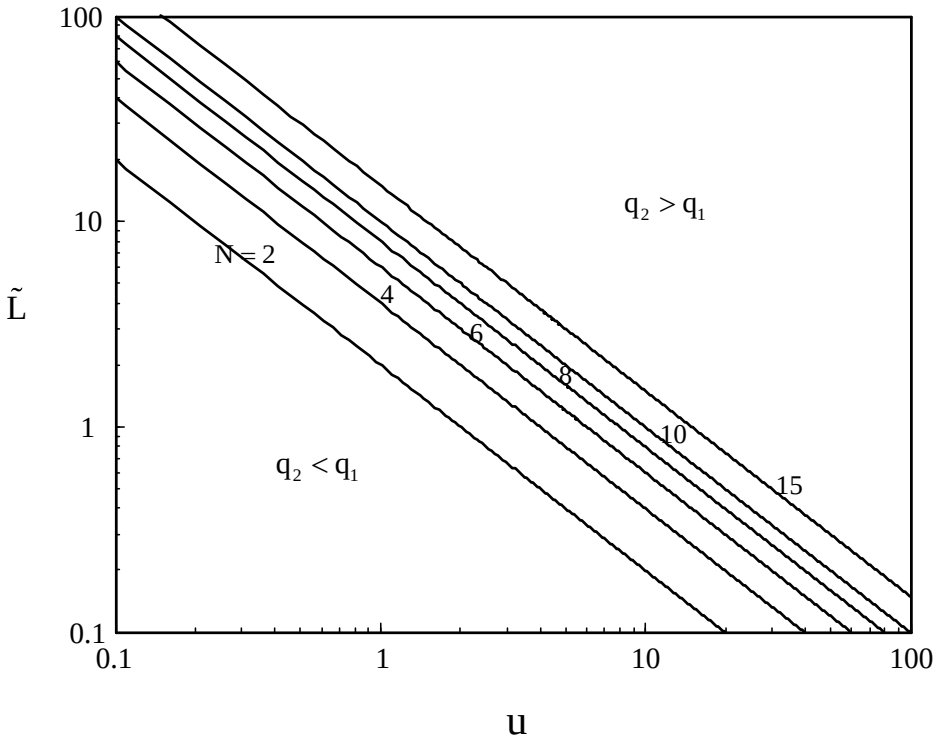

Figure 6.8: The design space for the crossflow heat exchanger.

Equation (6.30) indicates the superiority of the multi-tube design over the single tube design as shown in Fig. 6.8 in which lines represent $q_1 = q_2$ for each N. The space above each line represents that the multi-tube design is superior to the single tube design. The multi-tube design is preferred for a longer tube and higher velocity of the external flow.

6.2.2 Flow spacings

To summarize the analysis of sections 6.1 and 6.2.1, we have found that when the external flow (U_∞, or u) is fixed and the total tube length increases, the flow configuration must evolve from Fig. 6.1 to Fig. 6.3. The total volume of the crossflow heat exchanger increases in proportional with L, or, as indicated at the start,

$$V = HWL \tag{6.31}$$

The width of the cross-section perpendicular to the external flow is

$$W = D + S \tag{6.32}$$

where S is the spacing between adjacent columns of tubes. Earlier, constructal design has shown that if the flow is laminar ($U_\infty D/\nu < 10$) then the spacing for maximal heat transfer density must be of order [2]

$$\frac{S}{NH} \sim \left[\frac{\Delta P_\infty (NH)^2}{\alpha_\infty \mu_\infty}\right]^{-1/4} \tag{6.33}$$

In this expression, NH is the length of flow through the stack, α_∞ and μ_∞ are the thermal diffusivity and the viscosity of the external fluid, and ΔP_∞ is the pressure

difference scale maintained by the external flow,

$$\Delta P_\infty \sim \frac{1}{2}\rho U_\infty^2 \tag{6.34}$$

If the tubes are arranged in a square pattern (or in another regular-polygon pattern), the vertical length H is of order

$$H \sim D + S \tag{6.35}$$

Together, Eqs. (6.30)-(6.32) determine the total volume when the tube diameter and the external flow are specified. In particular, Eqs. (6.33)-(6.35) show that S is smaller than D when

$$Re_D > Pr^{-1/2} N \tag{6.36}$$

where $Re_D = U_\infty D/\nu$ and $Pr^{-1/2} \sim 1$.

6.2.3 Effectiveness of multi-tube design

Now, we can consider how many tubes are optimal for the multi-tube design. According to Eq. (6.21) the heat transfer rate for the multi-tube design is written

$$q_2 = K_1 \frac{1}{N}\left(1 - e^{-N/u}\right) \tag{6.37}$$

where K_1 is a constant

$$K_1 = \rho_\infty W L U_\infty c_{P,\infty} \Delta T \tag{6.38}$$

The maximum heat transfer rate is obtained by solving

$$\frac{\partial q_2}{\partial N} = \frac{1}{u} e^{-N/u} - \frac{1}{N}\left(1 - e^{-N/u}\right) = 0 \tag{6.39}$$

Equation (6.39) is satisfied when N=0; so, the maximum heat transfer rate is

$$q_{2,max} = K_1 \lim_{N \to 0}\left[\frac{1}{N}\left(1 - e^{-N/u}\right)\right] = (\pi DL)\, h\Delta T \tag{6.40}$$

The maximum heat transfer rate for the multi-tube design equals the theoretical maximum heat transfer rate as explained previously in Eq. (6.14). We see that $q_{2,max}$ is imaginary because N can not be zero for the multi-tube design. Furthermore, Eq. (6.40) implies that every heat transfer rate with N > 2 for the multi-tube design is less than the theoretical maximum heat transfer rate.

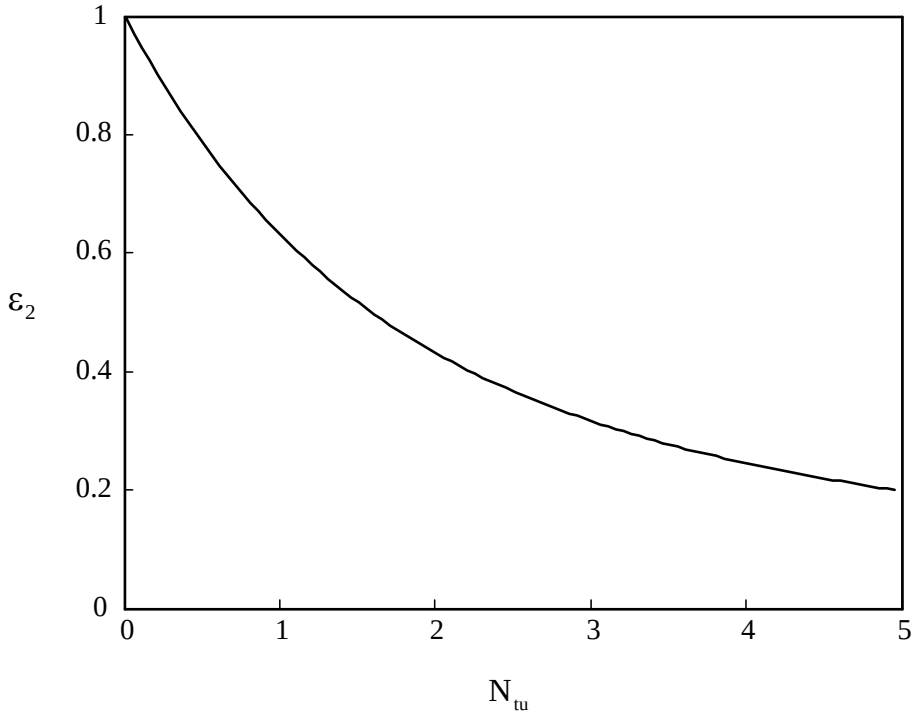

Figure 6.9: The effectiveness of the multi-tube design.

According to Eqs. (6.37) and (6.40) the effectiveness of the multi-tube design is defined as

$$\varepsilon_2 = \frac{q_2}{q_{2,max}} = \frac{1}{N_{tu}}\left(1 - e^{-N_{tu}}\right) \tag{6.41}$$

where

$$N_{tu} = \frac{\pi DhL}{\rho_\infty W(L/N) U_\infty c_{P,\infty}} \tag{6.42}$$

Figure 6.9 shows the effectiveness of the multi-tube design, which decreases when N_{tu} increases.

6.3 Comparison with classical $\varepsilon - N_{tu}$ relation

When C_{max} is unmixed for the crossflow heat exchanger, the effectiveness of the classical $\varepsilon - N_{tu}$ relation is [85]

$$\varepsilon = \frac{q}{q_{max}} = 1 - \exp\left\{-\frac{1}{C^*}\left[1 - \exp\left(-N_{tu} C^*\right)\right]\right\} \tag{6.43}$$

where

$$N_{tu} = \frac{UA}{C_{min}} \tag{6.44}$$

$$C_{min} = \min(C_h,\ C_c) \tag{6.45}$$

$$C^* = C_{min} / C_{max} \tag{6.46}$$

The effectiveness is simplified when condensation appears, that is, $C^* = 0$ or $C_{max} \to \infty$

$$\varepsilon = 1 - e^{-N_{tu}} \tag{6.47}$$

Figure 6.10 shows the effectiveness of crossflow heat exchangers for each ratio of capacity rates.

We see that the effectivenesses of the single tube design and the multi-tube design with the fixed total mass flow rate with condensation, cf., Eqs. (6.2) and (6.18), equal the classical $\varepsilon - N_{tu}$ relation, cf. Eq. (6.47), because N_{tu} equals $\tilde{L}$, cf. Eq. (6.4). This coincidence happens because capacity rates of both streams are fixed. In the classical effectiveness, Eq. (6.43), the denominator, q_{max}, is just a function of the minimum

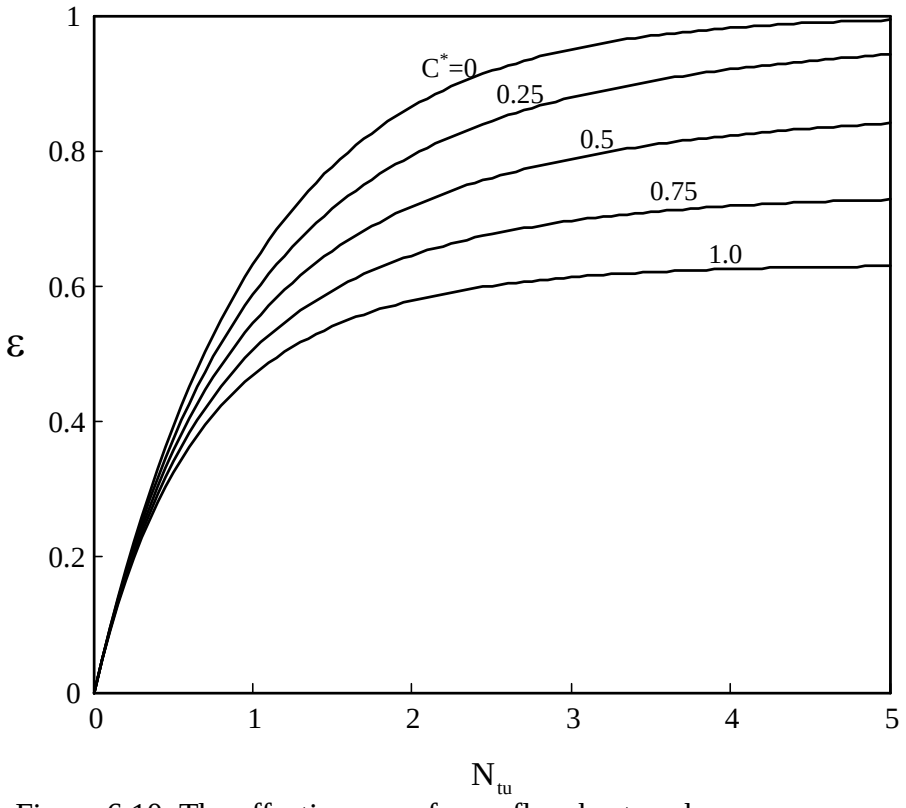

Figure 6.10: The effectiveness of crossflow heat exchangers.

capacity rate, C_{min}. The increase of the length does not effect q_{max} but causes to increase q; therefore, the effectiveness does not decrease with N_{tu} as shown in Fig. 6.10.

The effectivenesses of other two cases shown in Figs. 6.5 and 6.9, however, are different from the classical one. This discrepancy is caused by the variable capacity rates as described in the sections 6.1 and 6.2. For both cases, capacity rates of the internal fluid and the external fluid depend on the segmentation of the fixed length of the tube; it leads to that if the length L becomes longer the maximum heat transfer rate increases faster than the heat transfer rate. This results in the descending effectiveness as shown in Figs. 6.5 and 6.9.

In conclusion, we need to define a new effectiveness like Eqs. (6.15) and (6.41) which describe the morphology of cross heat exchangers in pursuit of a higher heat transfer rate when configuration is searched by segmenting a tube with the fixed stream velocities.

6.4 Results and discussion

A global measure of performance is the heat transfer density, which is the heat transfer rate per unit volume, q''', cf. Eq. (6.21). If L and D are specified, then q''' can be nondimensionlized as

$$\frac{q'''LD^2}{\dot{m}c_P\left(T_0 - T_\infty\right)} = \frac{1 - e^{-N_{tu}}}{\left(1 + \frac{S}{D}\right)^2} \tag{6.48}$$

Smaller spacings (S < D) mean higher heat transfer densities. If the external Reynolds number is high enough [cf. Eq. (6.36)], then S/D << 1 and Eq. (6.48) reduces to

$$\frac{q'''LD^2}{\dot{m}c_P\left(T_0 - T_\infty\right)} = 1 - e^{-N_{tu}} \tag{6.49}$$

which is the same N_{tu} function as Eq. (6.47). In this limit (S/D << 1), effectiveness and heat transfer density are achievable as N_{tu} increases. In the construction proposed in this chapter, the global effectiveness is almost the same as the global heat transfer density of the volume inhabited by crossflow.

According to the present analysis, the configuration of condensers and heaters in power plants can be explained; condensers consist of numerous tubes and heaters have relatively few tubes. Each component operates at the saturated temperature of the external steam flow, and the temperature of water inside tubes increases due to condensation on the outer surface of tubes.

Condensers can be considered to have the same mass flow rate of every tube described in the section 6.1.2 because the pump keeps the velocity of the sea water inside tubes constant [92]. According to Fig. 6.4, a longer tube leads to more heat transfer; in addition, more segments lead to more heat transfer for the fixed length. It means that the number of tube segments for condensers should be large for the better performance. This geometric feature is confirmed by the design data, which shows a very large number of tubes [93].

On the other hand, the heater has the fixed total mass flow rate because the fixed total internal flow rate based on the required electricity of power plants is divided equally among the tubes [94]. As shown in section 6.1.3, the segmenting of the tubes does not affect the heat transfer rate; so, fewer segments are preferred from a manufacturing point of view. The design practice shows that heaters have considerably fewer tubes than the condenser [93].

In summary, it is possible to conceptualize the entire architecture of the crossflow heat exchanger by starting from the single-tube design (Fig. 6.1) and searching for more and more heat transfer. This led to segmenting the tubes to a characteristic length, which were then stacked in the direction of the external stream. More heat transfer was achieved by sizing the spacings between tubes such that the flow in the spacings is penetrated fully by heat transfer from the tubes.

7. Conclusions

The main conclusion of this thesis is that it is possible to rationalize and derive the principle features of an engineering flow component from the free search for flow configuration when the global size is constrained. In every chapter we showed that the major geometric parameters for the optimal drawing for three components of power plants can be predicted with the constructal law. The configuration emerges such that its performance is maximized by distributing the flow resistances better and better though the available volume.

In chapter two we illustrated the constructal design method by focusing on the steam generator, for which we derived the dimensions of the tubes, the number of riser tubes, and the circulation flow rate (and the related steam production rate). The heat transfer rate from hot gases to riser tubes was maximized to find the number of riser tubes. For the tube diameter ratio the global flow resistance of the self-pumping system of the steam generator was obtained and it was minimized under the flow volume constraint. The formulae for these dimensions were deduced as a function of design conditions and properties of fluid. The number of predicted riser tubes was confirmed with the real design data of 100 MW steam generator; 541 for the constructal design and 400 for the real design. It was found that the pressure is the essential parameter to classify the configuration of steam generators.

In chapter three we predicted the optimal spacing between adjacent tubes and the

number of tubes of downcomer for the continuous steam generator which consisted of all heated tubes. The intersection of asymptotes method was applied under the volume constraint; the heat transfer rates for the large and small tube spacings were deduced and then the optimal tube spacing was found by equating two heat transfer rates. The corresponding maximum heat and mass flow rates were obtained. All these data were formulated as a function of Bejan number (Eq. (3.42)). The flow reversal position, which is a chronic problem in the design of the continuous steam generator, was investigated by minimizing the global flow resistance; it led to the formula for the number of the riser tubes (Eqs. (3.69) and (3.72))

In chapter four we showed that the total turbine mass was distributed in a balanced way based on the total mass of turbines for two turbines (Eqs. (4.15) and (4.16)), and that more mass should be distributed at high pressure for the multiple turbines. The total power delivery of a thermal power plant was maximized under the total mass constraint; it led to the mass distribution, i.e. resistance distribution, among turbines. The reversible isothermal expander model was assumed for the turbine modeling of multiple turbines. For a high pressure turbine in series with a low-pressure turbine (two turbines), the optimal intermediate pressure is the geometric average of high-pressure and low pressure. For a train consisting of many turbines expanding the steam at nearly constant temperature, the pressure ratio between consecutive intermediate pressures should be constant.

In chapter five we illustrated how the configuration of a heat exchanger with natural and forced convection with fixed size controlls the global performance. This effect was used to select the configuration of the flow system. The search for the flow configuration was pursued systematically, from the simplest configuration (two tubes) to the more complex (three and four tubes). In each case, there was a particular configuration that offered maximum global performance (heat transfer density). When the cold fluid circulated in two vertical tubes, the best configuration had tubes with nearly the same diameter. When the configuration had three tubes, and if the tube spacing varied, then it was possible to optimize the spacing as well. This geometric method and results represent a departure from the traditional approach, which focuses on a one-scale configuration with many tubes with the same diameter and spacing.

In chapter six we showed that the crossflow heat exchanger had the particular configuration corresponding to the maximum heat transfer rate. For the case of condensation on the outer surface of a tube, the heat transfer density decreased as the tube length increased; this led to the proposal to segment the tube into several tubes. The tube segments must have a certain length in pursuit of higher heat transfer rate for the fixed internal fluid velocity of each tube (Fig. 6.4), whereas the number of tubes was insensitive to the thermal performance for the fixed total mass flow rate (Eq. (6.19)). Without condensation, the multi-tube design was superior to the single tube design for a specified space (Fig. 6.8). Finally, the spacings between tubes were selected optimally

such that the global heat transfer density was maximized. These findings explained several geometric features of condensers and heaters of power plants: significantly large number of tubes for condensers and relatively fewer tubes for heaters.

The added benefit of these results is the size effect, i.e. the *scaling*. This means that the designer can predict how the drawing *morphs* when the allotted size changes. Scaling up and scaling down are now possible because the principle of generation of flow configuration is in hand.

At the power plant level, the many components conceptualized in this manner might be assembled into one "construct" that relies on the fixed sizes of the many. It is at this level that scaling yields benefit, by allowing tradeoffs between the size of one component against the size of another. All such tradeoffs lead to the distribution of "sizes" over the entire installation, with the global objective of improving the global efficiency of the power plant. The distributing of sizes is leading the design in the same direction as the more established methods of distributing (balancing) the destruction of exergy, or generation of entropy [3, 95-97]. Furthermore, the constructal design procedure described in this thesis might be applied to the design and engineering of every engineered product.

References

[1] A. Bejan and S. Lorente, Constructal theory of generation of configuration in nature and engineering , J. Appl. Phys. 100 (2006) 041301.

[2] A. Bejan and S. Lorente, Design with Constructal Theory, Wiley, Hoboken, NJ, 2008.

[3] A. Bejan, Advanced Engineering Thermodynamics, 2nd ed., Wiley, New York, 1997.

[4] A. Bejan, Shape and Structure, from Engineering to Nature, Cambridge University Press, Cambridge, UK, 2000.

[5] A.H. Reis, Constructal theory: from engineering to physics, and how flow systems develop shape and structure, Appl. Mech. Rev. 59 (2006) 269-282.

[6] G. Hernandez, J.K. Allen, F. Mistree, Platform design for customizable products as a problem of access in a geometric space, Eng. Optimiz. 35 (2003) 229-254.

[7] Y. Chen, P. Cheng, Heat transfer and pressure drop in fractal tree-like microchannel nets, Int. J. Heat Mass Transfer 45 (2002) 2643-2648.

[8] D.V. Pence, Reduced pumping power and wall temperature in microchannel heat sinks with fractal-like branching channel networks, Microscale Thermophys. Eng. 6 (2002) 319-330.

[9] A.H. Reis, A.F. Miguel, M. Aydin, Constructal theory of flow architecture of the lungs, J. Med. Phys. 31 (2004) 1135-1140.

[10] S.M. Senn, D. Poulikakos, Laminar mixing, heat transfer, and pressure drop in treelike microchannel nets and their application for thermal management in polymer electrolyte fuel cells, J. Power Sources 130 (2004) 178–191.

[11] S.M. Senn, D. Poulikakos, Tree network channels as fluid distributors constructing double-staircase polymer electrolyte fuel cells, J. Appl. Phys. 96 (2004) 842-852.

[12] F. Lundell, B. Thonon, J. A. Gruss, Constructal networks for efficient cooling/heating, Second Conference on Microchannels and Minichannels, Rochester, NY, 2004.

[13] V.A.P. Raja, T. Basak, S.K. Das, Thermal performance of multi-block heat exchanger designed on the basis of Bejan's constructal theory, Int. J. Heat Mass Transfer 51 (2008) 3582-3594.

[14] M. Lallemand, F. Ayela, M. Favre-Marinet, A. Gruss, D. Maillet, P. Marty, H. Peerhossaini, L. Tadrist, Thermal transfer in microchannels : applications to micro-exchangers, French Congress on Thermics, SFT 2005, Reims, 30 May – 2 Jun 2005.

[15] N. Kockmann, T. Kiefer, M. Engler, P. Woias, Channel networks for optimal heat transfer and high throughput mixers, ECI International Conference on Heat Transfer and Fluid Flow in Microscale, Castelvecchio Pascoli, Italy, Sept. 2005.

[16] Y.S. Muzychka, Constructal design of forced convection cooled microchannel heat sinks and heat exchangers, Int. J. Heat Mass Transfer 48 (2005) 3119-3127.

[17] Y.S. Muzychka, Constructal multi-scale design of compact micro-tube heat sinks and heat exchangers, Int. J. Therm. Sci. 46 (2007) 245-252.

[18] X.-Q. Wang, A.S. Mujumdar, C. Yap, Numerical analysis of blockage and optimization of heat transfer performance of fractal-like microchannel nets, J. Electron. Packag. 128 (2006) 38–45.

[19] A. Stodola, Steam Turbines, D. Van Nostrand Company, 1905.

[20] J. Yoon, Doosan Heavy Industries & Construction Co., Ltd., Private communication, June 2008.

[21] S.C. Stultz and J.B. Kitto, ed., Babcock & Wilcox STEAM its generation and use, Babcock & Wilcox, 2005.

[22] J. G. Singer, ed., Combustion Engineering: A Reference Book on Fuel Burning and Steam Generation, Revised Edition, Combustion Engineering, Inc., New York, 1991.

[23] M. J. Lighthill, Theoretical considerations on free convection in tubes, Quart. J. Mech. Appl. Math. 6 (1953) 398-439.

[24] B. W. Martin, Free convection in an open thermosyphon with special reference to turbulent flow, Proc. Roy. Soc. A230 (1955) 502-530.

[25] B. W. Martin, Free convection heat transfer in the inclined open thermosyphon, Proc. Inst. Mech. Eng. 173 (1959) 761-778.

[26] B. W. Martin and H. Cohen, Heat transfer by free convection in an open thermosyphon tube, B. J. Appl. Phys. 5 (1954) 91-95.

[27] A. Bejan, Heat Transfer, Wiley, New York, 1993, p. 319.

[28] J.R.S. Thom, Prediction of pressure drop during forced circulation boiling of water, J. Heat Mass Transfer 7 (1964) 709-724.

[29] L.F. Moody, Friction factors for pipe flow, Trans. ASME 66 (1944) 671-684.

[30] J.P. Holman, Heat Transfer, 5th ed., McGraw-Hill, 1981, p. 229.

[31] S. Kang, Doosan Heavy Industries & Construction Co., Ltd., private communication, May 2008.

[32] M. Favre-Marinet, S. Le Person, and A. Bejan, Maximum heat transfer rate density in two dimensional minichannels and microchannels, Microscale Thermophysical Engineering, Vol. 8, 2004, pp. 225-237.

[33] A. Bejan, Convection Heat Transfer, 3rd ed., Wiley, NJ, 2004.

[34] S. Bhattacharjee and W.L. Grosshander, The formation of a wall jet near a high temperature wall under microgravity environment, ASME HTD, Vol. 96, 1988, pp. 711-716.

[35] S. Petrescu, Comments on the optimal spacing of parallel plates cooled by forced convection, International Journal of Heat and Mass Transfer, Vol. 37, 1994, p.1283.

[36] K. Kim, Doosan Heavy Industries & Construction Co., Ltd., private communication, April 2008.

[37] A. F. Ghoniem, Energy and the Entropy Challenge, Meeting the Entropy Challenge, AIP Conference Proceedings, New York, 2008.

[38] EG&G Technical Services, Fuel Cell Handbook, 7th Edition, U.S. DOE, Office of Fossil Energy, NETL, Morgantown, West Virginia, 2004, pp. 8-91.

[39] Light-Duty Automotive Technology and Fuel Economy Trends: 1975 through 2008, United States Environmental Protection Agency, EPA420-S-08-003, 2008

[40] A. Bejan, Advanced Engineering Thermodynamics, 3rd ed., Wiley, Hoboken, 2006, pp. 534-537.

[41] T. R. Strobridge, Cryogenic refrigerators: an updated survey, NBS Tech. Note (US), No. 655, June 1974.

[42] A. Bejan and S. Lorente, Thermodynamic optimization of flow architecture: dendritic structures and optimal sizes of components, ASME Paper IMECE 2002-33158, presented at the International Mechanical Engineering Congress and Exposition, New Orleans, LA, Nov. 17-22, 2002.

[43] Provided by Doosan Heavy Industries & Construction Co., Ltd., June 2008.

[44] J. K. Salisbury, Steam turbines and their cycles, Wiley, NY, 1950.

[45] W. P. Sanders, Turbine steam path, Pennwell, Tulsa, 2004.

[46] I. J. Day, H. P. Hodson, J. P. Longley, J. D. Denton, S. Gallimore, P. Came, C. Robinson and J. B. Young, Cambridge turbomachinery course, Whittle laboratory, Department of Engineering, University of Cambridge, 25-29 June 2001.

[47] A. Donatello, Steam Generators: Description and Design, Springer Berlin Heidelberg, 2008.

[48] D. Q. Kern and A. D. Krans, Extended Surface Heat Transfer, McGraw-Hill, 1972.

[49] V. Ganapathy, Industrial Boilers and Heat Recovery Steam Generators, Marcel Dekker, Inc., New York, 2003.

[50] M. P. Boyce, Handbook for Cogeneration and Combined Cycle Power Plants, ASME Press, New York, 2002.

[51] L. F. Drbal, P. G. Boston, K. L. Westra and R. B. Erickson, Power Plant Engineering, Black & Veatch, Champman & Hall, 1996

[52] D. A. Reay, Heat Recovery System, E. & F. N. Spon, London, 1979.

[53] H. L. Solberg, O. C. Cromer and A. R. Spalding, Elementary Heat Power, Wiley, New York, 1946.

[54] D. Q. Kern and A. D. Kraus, Extended Surface Heat Transfer, McGraw-Hill, 1972.

[55] M. P. Boyce, Handbook for Cogeneration and Combined Cycle Power Plants, ASME Press, New York, 2002.

[56] L. F. Drbal, P. G. Boston, K. L. Westra and R. B. Erickson, Power Plant Engineering, Black & Veatch, Champman & Hall, 1996.

[57] S. Kang, Doosan Heavy Industries & Construction Co., Ltd., Private communication, May 2009.

[58] V. A. P. Raja, T. Basak and S. K. Das, Thermal performance of multi-block heat exchanger designed on the basis of Bejan's constructal theory, International Journal of Heat and Mass Transfer 51 (2008) 3582-3594.

[59] J. L. Lage, Tube-to-tube heat transfer degradation effect on finned-tube heat exchangers, Numerical Heat Transfer Part A 30 (2001) 321-337.

[60] H. M. S. Bahaidarah, N. K. Anand and H. C. Chen, A numerical study of fluid flow and heat transfer over a bank of flat tubes, Numerical Heat Transfer Part A 48 (2005) 359-385.

[61] A. Vali, C. J. Simonson, R. W. Besant and G. Mahmood, Numerical model and effectiveness correlations for a run-around heat recovery system with combined counter and cross flow exchangers, International Journal of Heat and Mass Transfer 52 (2009) 5827-5840.

[62] L. Zhang, Flow maldistribution and thermal performance deterioration in a cross-flow air to air heat exchanger with plate-fin cores, International Journal of Heat and Mass Transfer 52 (2009) 4500-4509.

[63] A. Triboix, Exact and approximate formulas for cross flow heat exchangers with unmixed fluids, International Communications in Heat and Mass Transfer (2009) 121-124.

[64] Y. Haseli, I. Dincer and G. F. Naterer, Optimum temperatures in a shell and tube condenser with respect to exergy, International Journal of Heat and Mass Transfer 51 (2008) 2462-2470.

[65] G. Diaz, Controllability of cross-flow two-phase heat exchangers, International Journal of Heat and Mass Transfer 50 (2007) 4559-4567.

[66] W. Q. Tao , Y. P. Cheng and T. S. Lee, The influence of strip location on the pressure drop and heat transfer performance of a slotted fin, Numerical Heat Transfer Part A 52 (2007) 463-480.

[67] W. A. Khan, J. R. Culham and M. M. Yovanovich, Convection heat transfer from tube banks in crossflow: Analytical approach, International Journal of Heat and Mass Transfer 49 (2006) 4831-4838.

[68] A. K. Dhiman, R. P. Chhabra, A. Sharma and V. Eswaran, Effects of reynolds and prandtl numbers on heat transfer across a square cylinder in the steady flow regime, Numerical Heat Transfer Part A 49 (2006) 717-731.

[69] H. A. Navarro and L. Cabezas-Gómez, A new approach for thermal performance calculation of cross-flow heat exchangers, International Journal of Heat and Mass Transfer 48 (2005) 3880-3888.

[70] A. M. F. El-Shaboury and S. J. Ormiston, Analysis of laminar forced convection of air crossflow in in-line tube banks with nonsquare arrangements, Numerical Heat Transfer Part A 48 (2005) 99-126.

[71] M. Tutar and A. Akkoca, Numerical analysis of fluid flow and heat transfer characteristics in three-dimensional plate fin-and-tube heat exchangers, Numerical Heat Transfer Part A 46 (2004) 301-321.

[72] V. Prabhakar, G. Biswas and V. Eswaran, Numerical prediction of heat transfer in a channel with a built-in oval tube and various arrangements of the tvortex generators, Numerical Heat Transfer Part A 44 (2003) 315-334.

[73] Y. Ping and H. Kou, Entropy generation on a crossflow heat exchanger including three gas streams with different arrangements and the effect of longitudinal wall conduction, Numerical Heat Transfer Part A 43 (2003) 619-638.

[74] E. Buyruk, M. W. Johnson and I. Owen, Numerical and experimental study of flow and heat transfer around a tube in cross-flow at low Reynolds number, International Journal of Heat and Fluid Flow 19 (1998) 223-232.

[75] R. T. Ogulata and F. Doba, Experiments and entropy generation minimization analysis of a cross-flow heat exchanger, International Journal of Heat and Mass Transfer 41 (1998) 373-381.

[76] Y. Ping and H. Kou, The effect of longitudinal wall conduction in a three-fluid crossflow heat exchanger, Numerical Heat Transfer Part A 34 (1998) 135-150.

[77] W. W. Lin and D. J. Lee, Second-law analysis on a pin-fin array under crossflow, International Journal of Heat and Mass Transfer 40 (1997) 1937-1945.

[78] K. W. Hansen and K. Demandt, Dynamics of a cross-flow heat exchanger with fins, International Journal of Heat and Mass Transfer 17 (1974) 1029-1036.

[79] COMSOL Heat Transfer Module User's Guide, 2008.

[80] S. Kakac, A. E. Bergles, and F. Mayinger, Eds., Heat Exchangers: Thermal-Hydraulic Fundamentals and Design, Hemisphere, Washington, 1981.

[81] A. P. Fraas, Heat Exchanger Design, 2nd edition, Wiley, New York, 1989.

[82] W. M. Kays and A. L. London, Compact Heat Exchangers, 3rd edition, McGraw-Hill, New York, 1984.

[83] E. U. Schlunder, Ed., Heat Exchanger Design Handbook, Vols. 1-5, Hemisphere, New York, 1983.

[84] F. P. Incropera and D. P. Dewitt, Fundamentals of Heat and Mass Transfer, Wiley, New York, 2002.

[85] J. E. Hesselgreaves, Compact Heat Exchangers, Pergamon, New York, 2001

[86] B. Sunden and M. Faghri, Eds., Computer Simulations in Compact Heat Exchangers, Computational Mechanics Publications, Boston, 1998.

[87] D. Chisholm, Ed., Development in Heat Exchanger Technology, Applied Science Publishers, 1980.

[88] T. Kuppan, Heat Exchanger Design Handbook, Marcel Dekker, New York, 2000.

[89] H. Martin, Heat Exchangers, Hemisphere, Washington, 1992.

[90] E. M. Smith, Thermal Design of Heat Exchangers, Wiley, New York, 1997.

[91] G. F. Hewitt, G. L. Shires and T. R. Bott, Process Heat Transfer, CRC Press, Boca Raton, 1994.

[92] P. Fraas and M. Ozisik, Heat Exchanger Design, Wiley, New York, 1965

[93] M. Choi, Doosan Heavy Industries & Construction Co., Ltd., Private communication, March 2010.

[94] H. Martin, Heat Exchangers, Hemisphere, Washington, 1992.

[95] M. Moran, A Guide to Efficient Energy Use, 2nd ed., ASME Press, New York, 1989.

[96] E. Sciubba and R. Melli, Artifical intelligence in thermal systems design: concepts and applications, Nova Science Publishers, New York, 1998.

[97] A. Bejan, Entropy Generation through Heat and Fluid Flow, Wiley, New York, 1982.

Biography

Yong Sung Kim received his MS in Mechanical Engineering from Seoul National University in 1988. He started his career as an engineer of steam generators at Samsung Heavy Industries in South Korea. He expanded his interest in power and water plants at Doosan Heavy Industries which sponsored his Ph.D study at Duke University in the United States. Before coming to Duke University he worked as a director for Doosan Babcock setting up the research and development center in Glasgow, Scotland.

Yong Sung Kim has written numerous technical reports and papers on various topics of the design and operation of thermal power plants. These include solid, thermal and fluid performances and various kinds of dynamic behavior of thermal power plants and their components. He was in charge of USC (UltraSuper Critical) steam generator development sponsored by the South Korean government. His major research, design and engineering interests are to predict configurations of energy systems and their components in order to archive greater performance under the constraint of fixed fuel rates.